UNIVERSIDAD DE CHILE
FACULTAD DE CIENCIAS FÍSICAS Y MATEMÁTICAS
DEPARTAMENTO DE INGENIERÍA QUÍMICA, BIOTECNOLOGÍA Y MATERIALES

PHOTO-ANODES BASED ON MOLYBDENUM OXIDES FOR THE HYDROLYSIS OF WATER IN A PHOTO-ELECTROCHEMICAL CELL

TESIS PARA OPTAR AL GRADO DE
DOCTOR EN CIENCIAS DE LA INGENIERÍA, MENCIÓN INGENIERÍA QUÍMICA Y BIOTECNOLOGÍA

MATÍAS ALEJANDRO GARCÍA GARCÍA

PROFESORA GUÍA:
MELANIE COLET LAGRILLE

PROFESOR CO-GUÍA:
FRANCISCO GRACIA CAROCA

MIEMBROS DE LA COMISIÓN:
PAULO ARAYA FIGUEROA
SALVADOR ESLAVA FERNÁNDEZ
VICTOR FUENZALIDA ESCOBAR

SANTIAGO DE CHILE
2019

RESUMEN DE LA TESIS PARA OPTAR
AL GRADO DE DOCTOR EN CIENCIAS DE
LA INGENIERÍA, MENCIÓN INGENIERÍA
QUÍMICA Y BIOTECNOLOGÍA
POR: MATÍAS ALEJANDRO GARCÍA GARCÍA
FECHA: 2019
PROF. GUÍA: MELANIE COLET LAGRILLE

PHOTO-ANODES BASED ON MOLYBDENUM OXIDES FOR THE HYDROLYSIS OF WATER IN A PHOTO-ELECTROCHEMICAL CELL

Las fuentes de energía limpias y sostenibles deben ser consideradas una base importante para el futuro crecimiento y desarrollo económico de cualquier país. Actualmente, el suministro mundial de energía depende en gran medida de los combustibles fósiles. Esto conlleva a que tecnologías tales como las celdas foto-electroquímicas se vuelvan especialmente atractivas, ya que permiten usar energía solar para producir hidrógeno. El funcionamiento de las celdas foto-electroquímicas se basa en el uso de semiconductores como electrodos, que al ser irradiados generan pares hueco-electrón, los cuales pueden migrar en la superficie del semiconductor y reaccionar con las especies adsorbidas o recombinarse entre sí. El hueco electrónico generado por la migración de un electrón puede oxidar una molécula de agua para producir oxígeno en el ánodo, mientras que los electrones generados viajan hacia el cátodo para reducir los protones presentes en el agua formando hidrógeno

El presente trabajo de tesis tuvo como objetivo general la sintesis (a través de los métodos de electrodeposición y de *spin−coating*) y caracterización del desempeño de foto-ánodos basados en óxidos de molibdeno para la producción de hidrógeno en una celda foto-electroquímica a partir de electrólisis de agua.

Películas de óxido de molibdeno dopadas con niquel y sin dopar se electrodepositaron aplicando un potencial de -1,377 V vs Ag / AgCl (KCl 3 M) durante 3 horas en un vidrio de cuarzo cubierto con dióxido de estaño dopado con flúor - FTO - sumergido en soluciones acuosas de molibdato-citrato a pH 9. Por otra parte, se depositaron peliculas de MoO_x, WO_3 y MoO_x dopado con W sobre vidrio de aluminoborosilicato recubierto con óxido de estaño dopado con flúor. Este proceso se realizó mediante *spin − coating* a 4000 rpm durante 40 segundos.

La caracterización de los foto-ánodos fabricados a través de electrodeposición y *spin − coating* sugiere que presentan propiedades semiconductoras y catalíticas que los hacen atractivos para su uso en una celda foto-electroquímica para la hidrólisis del agua. Sin embargo, aunque los foto-electrodos sintetizados a través de las técnicas mencionadas tienen un intervalo de banda prohibida óptimo para aprovechar eficientemente la luz solar, la caracterización foto-electroquímica mostró que estos electrodos no exhiben una estabilidad en solución acuosa y que son susceptibles a la foto-corrosion, que son factores limitantes para el uso de semiconductores convencionales como foto-electrodos.

RESUMEN DE LA TESIS PARA OPTAR
AL GRADO DE DOCTOR EN CIENCIAS DE
LA INGENIERÍA, MENCIÓN INGENIERÍA
QUÍMICA Y BIOTECNOLOGÍA
POR: MATÍAS ALEJANDRO GARCÍA GARCÍA
FECHA: 2019
PROF. GUÍA: MELANIE COLET LAGRILLE

PHOTO-ANODES BASED ON MOLYBDENUM OXIDES FOR THE HYDROLYSIS OF WATER IN A PHOTO-ELECTROCHEMICAL CELL

Sources of clean and sustainable energy are fundamental vectors for economic growth and development. The current global energy supply depends heavily on fossil fuels. This makes technology such as direct water splitting from harvesting solar energy in photo-electrochemical (PEC) systems potentially attractive, due to is a promising route for the environmentally-benign production of hydrogen. The principle of this technology utilises semiconductors to absorb photons of energy greater than their band-gap energy, generating an electron-hole pair. The hole could oxidise water to produce oxygen at the anode, whereas the electrons could reduce water to form hydrogen at the cathode.

The general aims of this research work has been to synthesize (through electrodeposition and spin-coating methods) and characterize the performance of photo-anodes based on molybdenum oxides for the production of hydrogen in a photo-electrochemical cell from water electrolysis.

Undoped and nickel-doped molybdenum oxide films were electrodeposited by applying -1.377 V vs Ag/AgCl (3 M KCl) during 3 hours on an FTO-coated glass substrate immersed in molibdatecitrate aqueous solutions at pH 9. On the other hand, MoO_x, WO_3 and W-doped MoO_x films on aluminoborosilicate glass (ABS) coated with fluorine-doped tin oxide (FTO) were deposited by spin-coating at 4000 RPM applied for 40 seconds.

The characterization of the fabricated photo-anodes (by electrodeposition and spin-coating) suggests that they present semiconducting and catalytic properties which make them attractive for their application in a photo-electrochemical cell for water splitting. Nevertheless, although all these photo-electrodes have an optimal band-gap for harnessing sufficient sunlight, the photo-electrochemical characterization showed that these photo-anodes do not exhibit a stability in aqueous solution and that are susceptible to the photo-corrosion, which are limiting factors for the use of conventional photovoltaic semiconductors as photo-electrodes.

A mis abuelos y a mi madre. En memoria de Luis Bravo.

Agradecimientos

En primer lugar, me gustaría agradecer al Grupo de Ingeniería Electroquímica (GIE) liderado por la Dra. Colet, me siento afortunado por haber compartido con un tremendo equipo de trabajo. Infinitas gracias a los profesores Victor Fuenzalida y Francisco Gracia por el apoyo académico que me brindaron durante mi estadía en la Universidad de Chile.

A mi familia, por el cariño y apoyo incondicional que me han entregado en los buenos y malos momentos. A Erna, por ser mi segunda mamá y por el amor inagotable que le ha dado a cada uno de sus nietos. A mi tata Elio, por su cariño paternal y por animarme a creer en mis sueños. A mi madre, por su amor, por estar siempre ahí y creer en mí. A Gustavo y Antonia, los mejores hermanos que la vida me pudo dar. Su alegría, perseverancia y cariño me inspiran a enfretar con garra y entrega cada nuevo desafio que decido tomar. A los tios más joviales y apañadores que se pueda tener, Verónica y Helio. Gracias por cada momento que tenemos la dicha de compartir.

Gracias a esos amigos que la vida a puesto en mi camino, con quienes he compartido historias y momentos inolvidables. Francisca, Sylvana, Dasna, Juanito, Anita, Romina, Michelle, Rodolfo, Daniela, Quiñelen, Karol, Alberto, Vane, Made, Claudia, Roberto, Mabel, Rorro, Jorge y Alexis, nunca estaré lo suficientemente agradecido por la ayuda, cariño y comprensión que me brindan cuando lo necesito.

Al laboratorio de Hidrometalurgia y Electroquímica, por ser literalmente mi segundo hogar durante estos ultimos 3 años. A Sergio, Carlita, Jacqueline, Evelyn, Joaquin, Eli, Kathy e Isaac gracias por las risas, los interminables almuerzos, la camaradería a prueba de balas y por sobre todo, por soportar mi a veces insufrible personalidad. A Ignacio y Cristian los integrantes mas nuevos del grupo, por la simpatia y los gratos (aunque lamentablemente cortos) momentos compartidos. Gracias a todos ustedes por tanto, ¡los amo cabros!.

A quienes me brindaron compañia y soporte en Inglatera: Salvador, Miriam, Ana Maria y Martin, gracias por hacer de mi paso por Bath una de las experiencias mas hermosas que me ha tocado vivir.

A Martin, mi covalente. Gracias por el cariño, paciencia y compañia (aunque esta última sea desde cualquier punto del planeta). Gracias por enseñarme los significados de ser persistente y fuerte.

Finalmente a la Comisión Nacional de Investigación Científica y Tecnológica (CONICYT) por la beca doctoral otorgada durante mi formación.

Table of Contents

List of Tables

List of Figures

Nomenclature

Symbol	Definition	Units
A	Geometric area	m^2
$\tilde{A}$	Absorbance	-
a_{i}	Activity of species i	-
c_{i}	Concentration of species i	$mol\ L^{-1}$
D_{i}	Diffusivity of species i	$m^2\ s^{-1}$
E^0	Standard potential	V
E_{cell}	Cell potential	V
E_{bg}	Band gap energy	eV
E_{cb}	Conduction band energy	eV
E_{vb}	Valence band energy	eV
G	Gibbs free energy	$J\ mol^{-1}$
H	Enthalpy	$J\ mol^{-1}$
I	Current	A
j	Current density	$A\ m^{-2}$
j_0	Exchange current density	$A\ m^{-2}$
k_{i}	Rate constant of reaction i	$mol\ m^{-2}\ s^{-1}$
k^0	Standard electrochemical kinetics constant	$mol\ m^{-2}\ s^{-1}$
S	Entropy	$J\ mol^{-1}\ K^{-1}$
T	temperature	K
t	time	s
ΔG_{rxn}	Gibbs free energy of reaction	$J\ mol^{-1}$
ΔH_{rxn}	Enthalpy of reaction	$J\ mol^{-1}$
ΔS_{rxn}	Entropy of reaction	$J\ mol^{-1}\ K^{-1}$
δ	Thickness of the boundary layer	m
η	Overpotential	V
ϕ	Electric potential	V
R	Reduced species	-
O	Oxidized species	-
V	Volume	m^3

Symbol	Definition	Units
$\Delta G^{\circ}_{f,\mathrm{i}}$	Gibbs free energy of formation of species i	$J\ mol^{-1}$
L_{film}	Film thickness	nm
β_0	Kinematic viscosity	$m^2\ s^{-1}$
ω	Rotational speed	$rad\ s^{-1}$
p_A	Vapor pressure of species A	$Torr$
α	Transfer coefficient	-
μ	Dynamic viscosity	$kg\ m^{-1}\ s^{-1}$
$u_{m,\mathrm{i}}$	Mechanical mobility of species i	-
r_{i}	Hydraulic radio of species i	m
h^{+}_{vb}	Electronic hole in valence band	-
e^{-}_{cb}	Electron in conduction band	-

Table 1: Physical constants.

Symbol	Definition	Units
c	Speed of light in the vacuum	$3.00 \cdot 10^{8}\ m\ s^{-1}$
F	Faraday constant	$9.65 \cdot 10^{4}\ C\ mol^{-1}$
h	Planck constant	$6.63 \cdot 10^{-34}\ J\ s$
k_B	Boltzmann constant	$1.38 \cdot 10^{-23}\ J\ K^{-1}$
N_A	Avogadro number	$8.02 \cdot 10^{23}\ mol^{-1}$
R	Ideal Gas	$8.31\ J\ mol^{-1}\ K^{-1}$

Chapter 1

Introduction

The increase in energy consumption in the world due to overpopulation and alternatives for generating clean energy are discussed in this chapter. Photo-electrochemical water splitting is presented as a promising alternative for harvesting the solar energy and convert it into chemical energy in the form of hydrogen, which can be used in a fuel cell to produce energy with zero greenhouse gases emissions. Based on this discussion, the hypothesis and general aim of this thesis are finally presented.

1.1. Hydrogen: A Solution to the Global Energy Crisis

Two hundred years ago there were less than one billion people living on Earth. Nowadays, according to the United Nations (UN) humans have exceeded the 7 billions on the planet [1]. This increase in the world population, together with economic growth of some countries, have triggered an abrupt increase in the global energy consumption, as shown in Figure 1.1.

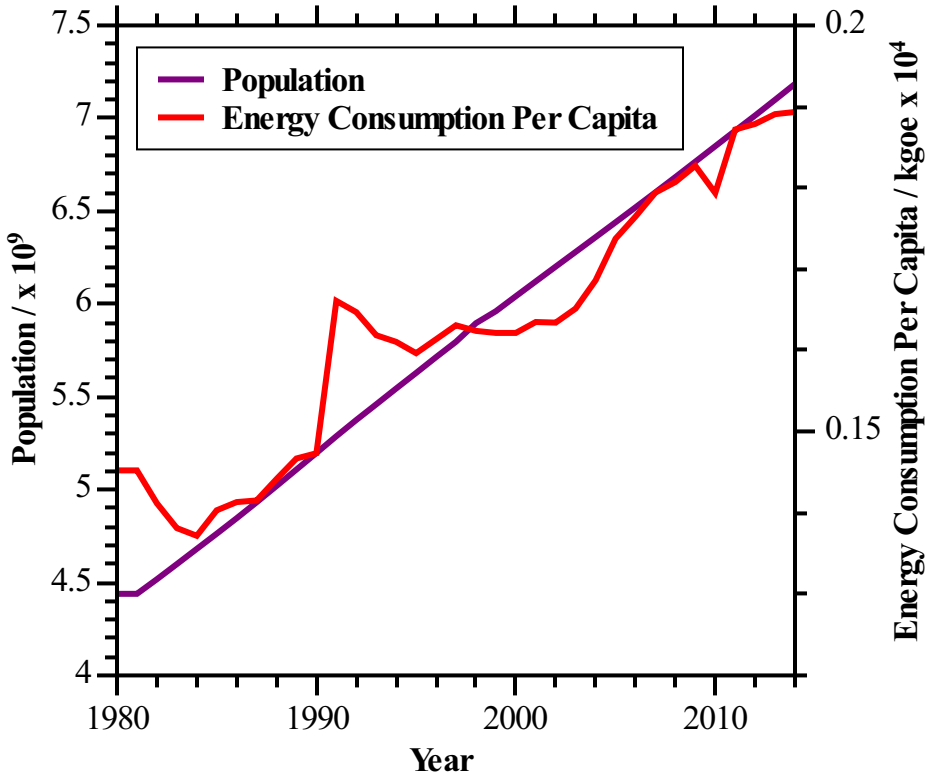

Figure 1.1: Population and annual energy consumption worldwide between 1980 and 2014 [2] [3].

As can be seen in Figure 1.2, in 1973 at least 75 % of the electrical energy was obtained from fossil fuels (coal, oil and natural gas), percentage that fell slightly to 66 % in 2015. This indicates that nowadays most of the energy used worldwide still comes from the combustion of fossil fuels, which is not a clean and sustainable approach [4]. In addition, fossil fuels are non-renewable, which motivates the study and development of systems for energy generation based on renewable sources (e.g. sunlight or wind) and that are environmentally friendly.

In this context, an attractive alternative to fossil fuels is hydrogen [5] [6] , which can be used to produce energy in an electrochemical device (fuel cell) and generates only water as the reaction product. Table 1.1 illustrates the main properties of hydrogen.

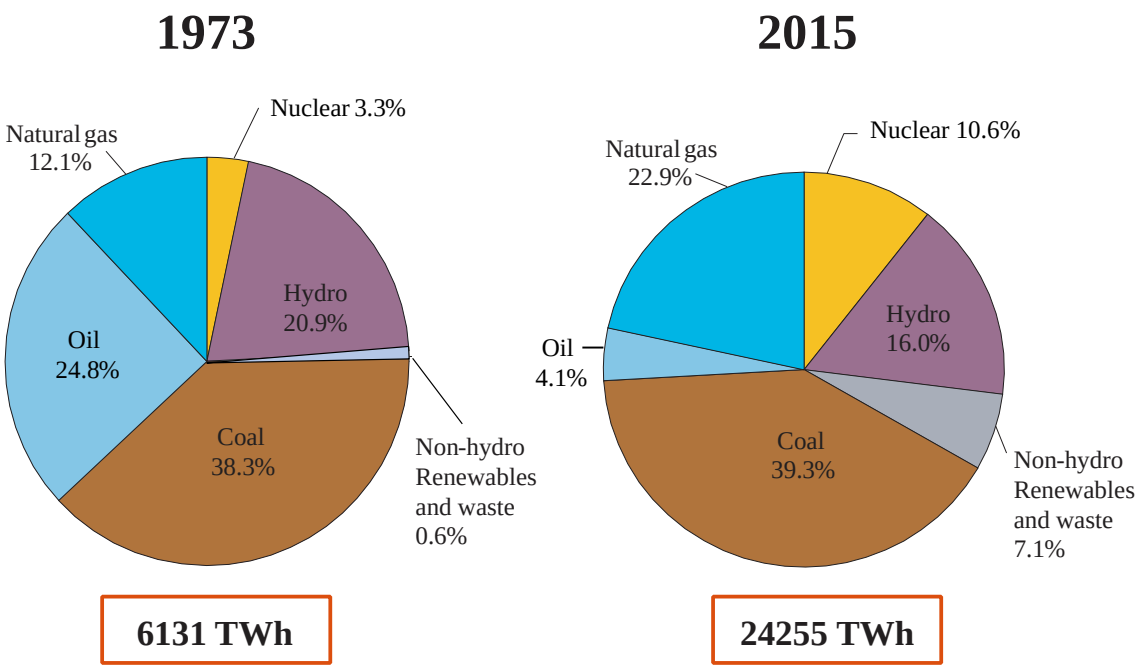

Figure 1.2: Source shares of electricity generation in 1973 and 2015. Adapted from [4].

Table 1.1: Physicochemical properties of hydrogen [7] [8].

Property	Value	Units
Molecular weight	2.02	$g\,mol^{-1}$
Density (at 1 atm and 20 °C)	$8.38 \cdot 10^{-2}$	$kg\,m^{-3}$
Viscosity (at 1 atm and 20 °C)	$8.81 \cdot 10^{-5}$	$g\,cm^{-1}\,s^{-1}$
Boiling point	-253	°C
Flammable range in air	4 - 75	vol %
Auto ignition temperature	585	°C

Nowadays, ca. 96 % of world hydrogen production is by steam reforming of natural gas, as indicated by equation 1.1 [9]:

$$CH_{4(g)} + 2H_2O_{2(g)} \rightarrow 4H_{2(g)} + CO_{2(g)} \tag{1.1}$$

This process produces CO_2 and hydrogen contaminated with traces of carbon monoxide, which poisons platinum catalysts used in fuel cells [9]. Therefore, such applications require purer hydrogen, as can be produced by water electrolysis. At present, electrolysis of water to produce hydrogen accounts for only ca. 4 % of the world production of hydrogen. However, this is expected to increase with increasing need for storage of renewable energy [10]. Electrolysis will be discussed in detail in Chapter 2.

Due to the high specific energy[1] and low energy density[2] of hydrogen, its storage and transportation, cryogenically or at high pressure, remains an economic challenge, limiting its deployment as a clean fuel. Currently, hydrogen is stored economically in compressed gas form at up to 700 bar in gas cylinders. It is quite important to store hydrogen safely, because of the explosion risk, as hydrogen has very wide flammability limits (4 % – 75 % in air, and 4 % – 95 % in oxygen) [13]. Another alternative is to store it cryogenically in liquid form at temperatures lower than its boiling point of 20.28 K; however, its liquefaction is very energy intensive. Besides, it is possible to store hydrogen in metal hydrides such as $LiAlH_4$, $NaAlH_4$, and MgH_2, which require heat to desorb hydrogen gas [14]. As can be seen, the use of hydrogen as an alternative to fossil fuels is still under development. Despite the various benefits of using this gas as the next generation clean fuel, it is evident that there are still a number of hurdles to be overcome.

1.2. Solar Irradiance

The annual mean solar irradiance at normal incidence just outside the Earth's atmosphere is around 1,360 W m^{-2} [15], which converted to available solar power striking the Earth's surface (attenuated as it passes through the atmosphere) is equivalent to 130 million 500 MW power plants for electricity generation [16]. This amount of energy is higher than the global electrical power consumption of 30 TW predicted for 2050 [17], so electricity generation from the sunlight energy collected and efficiently converted in photo-active devices (such as photovoltaic modules) appears to be a promising approach to deal with the future environmental and energy challenges.

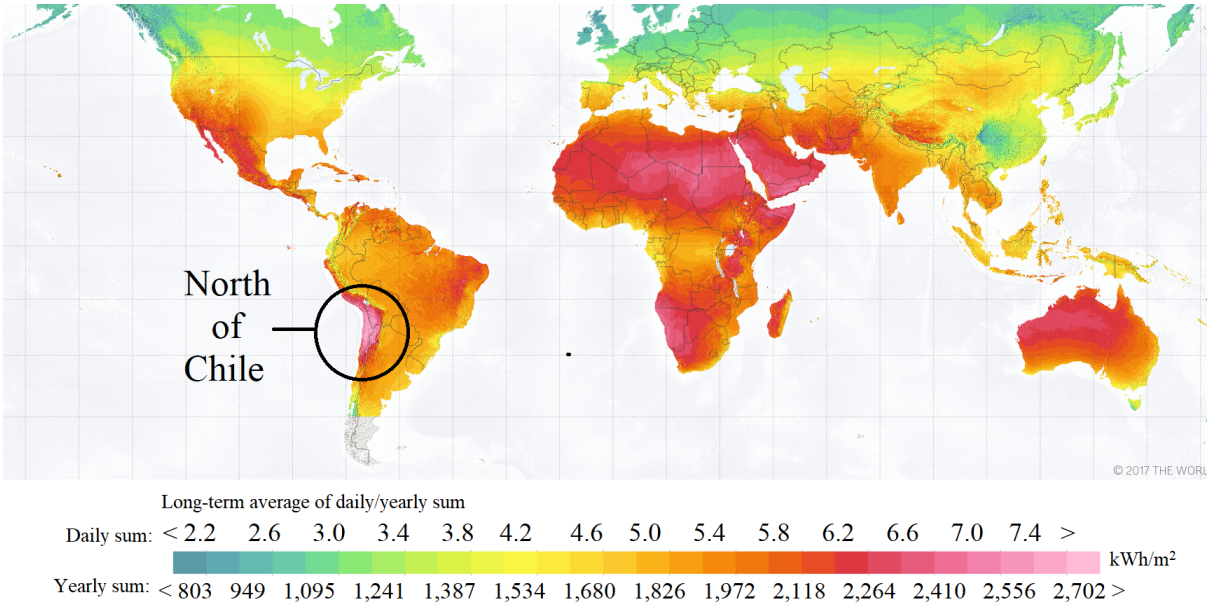

Figure 1.3: Distribution of solar irradiation in the world and Chile. Adapted from [18]

[1]Specific energy storage of H_2: $142 \cdot 10^6$ J/kg [11].

[2]Hydrogen has one of the highest energy density values per mass. Its energy density is between 120 and 142 MJ/kg. This means that for every 1 kg of mass of hydrogen, it has an energy value of 120-142 MJ [12].

The amount of solar irradiance received at any particular location on the Earth surface depends mainly on the latitude and the average cloud cover. Figure 1.3 shows that some locations in the world receive a high solar irradiance during the whole year, as in the Atacama Desert in the north of Chile; therefore, the countries where such areas lay are potential clean energy suppliers. In order to make this potential scenario a reality, the governments and industry of these countries need to encourage the research and development of technologies capable of converting solar energy efficiently to electrical energy, but also of storing this energy to be used during periods of zero or low insolation (night or days with cloudy weather).

It is well known that insolation varies both diurnally and seasonally, a reason for which an inbuilt capacity for energy storage is highly desirable if electricity is to be produced from solar energy. Presently, most of the photovoltaic technologies developed for standalone power systems rely on batteries for storage of electrical energy [19]. However, batteries lack of high energy storage densities (specific energies of only 30-140 W kg^{-1}) and ease of transportation. Therefore, fuels such as hydrogen, methane or methanol appear to be a much more attractive route to store solar energy in the form of chemical energy (compound bonds), since they offer high gravimetric and volumetric energy densities. In fact, the energy of visible-light photons is 1 to 3 eV, or 100 to 300 kJ mol^{-1}, which is more than sufficient to synthesize these fuels through many chemical routes [17][3]

1.3. Photo-Electrochemical Cells and Hydrogen Production

Hydrogen appears to be the best option for chemical storage of solar energy as its oxidation produces only water, enabling electrical energy production (either using conventional combustion or fuel cells) without greenhouse gases emissions.

Hydrogen can be readily produced by oxidation of water in an electrolysis cell, so in the last decades research has been centered in the development of systems that use solar energy for its production. In this regard, two approaches can be considered to capture the solar energy and store it in the form of chemical energy in hydrogen bonds: (i) a photovoltaic / electrolysis system and (ii) a photoelectrolysis system. In the first case, the solar energy is captured and converted to electrical energy in an array of photovoltaic modules and used in an electrolysis cell to produce hydrogen and oxygen by water splitting. The hydrogen produced at the cathode of the electrolysis cell is stored and subsequently used in a fuel cell stack or other similar device to satisfy the portable (e.g. electronic devices or transportation) or stationary (e.g. power station) demand for electricity. In the second case, hydrogen is directly produced in a photo-electrochemical cell (PEC) with one or both electrodes fabricated with semiconducting materials. Hydrogen produced by this means is stored and used identically to the case of a photovoltaic / electrolysis system. The advantage of this second approach is that solar energy is used directly to produce hydrogen, which means having a simple system operation and probably decreased implementation costs [19]. Figure 1.4 shows a diagram of

[3] Approximately 50 % of the solar radiation spectrum is in the infrared wavelength region and the other 50 % is distributed between the UV wavelength region (ca. 3 %) and the visible wavelength region (ca. 45 %) [15].

water splitting in a PEC.

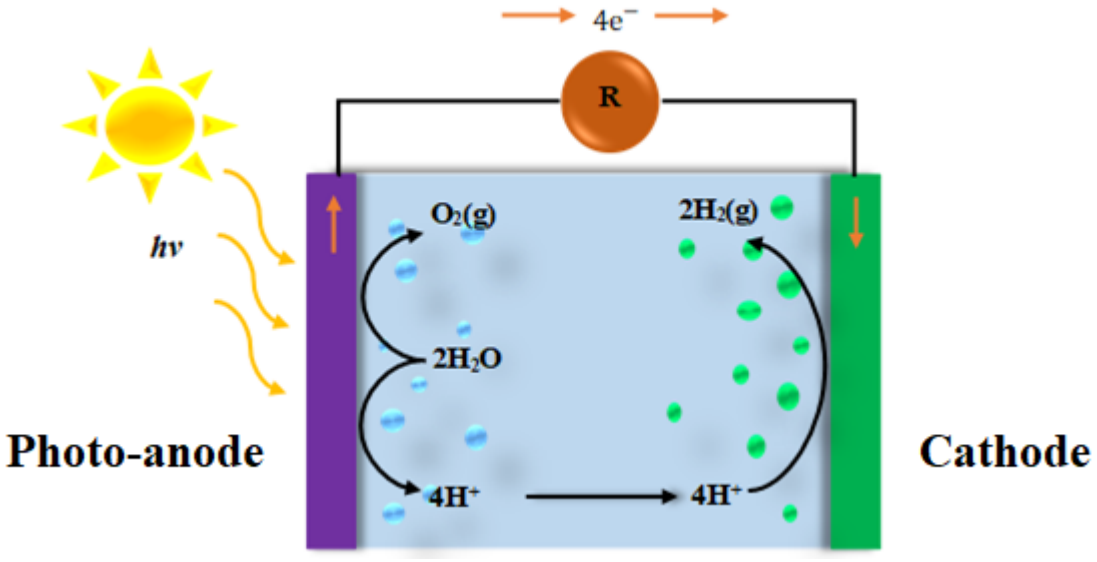

Figure 1.4: Simplified diagram of the operation of a photo-electrochemical cell (PEC) for the hydrolysis of water. In this case, the photo-sensitive electrode is the anode.

In order to promote the direct chemical decomposition of water into hydrogen and oxygen in a PEC according to the global reaction:

$$H_2O_{(l)} \rightarrow H_{2(g)} + \frac{1}{2}O_{2(g)} \tag{1.2}$$

a Gibbs free energy (ΔG°_{298K}) of 237 kJ mol^{-1} needs to be supplied to the system. This Gibbs free energy is equivalent to a potential difference (ΔE°_{298K}) of 1.23 V, which corresponds to the minimum potential that has to be applied between the electrodes (anode and cathode) of an electrochemical cell to promote the water splitting reaction 1.2 according to the half-reactions [17]:

Anode half-reaction:

$$\frac{1}{2}O_{2(g)} + 2H^{+}_{(aq.)} + 2\mathrm{e}^{-} \leftarrow H_2O_{(l)} \tag{1.3}$$

Cathode half-reaction:

$$2H^{+}_{(aq.)} + 2\mathrm{e}^{-} \rightarrow H_{2(g)} \tag{1.4}$$

A primary matter in the fabrication of a photo-electrochemical cell is the selection of an efficient (light to chemical energy conversion) and stable (under water photo-electrolysis conditions) material for the photo-electrode(s). The anode and/or cathode of these cells are

fabricated using semiconductor materials capable of absorbing the energy of the photons in the regions of ultraviolet and (some of them) visible wavelengths, promoting the half-reactions in Eq. (1.3) and/or (1.4) at the electrode(s) | electrolyte interface.

Three materials have received special attention for the fabrication of photo-anodes for photo-electrochemical cells: (i) titanium dioxide (TiO_2), (ii) hematite (α-Fe_2O_3), and (iii) tungsten trioxide (WO_3). These materials present high efficiencies for solar energy capture and conversion to chemical energy, stability under water splitting operating conditions and/or low cost and earth abundance [9]. However, when operating under illumination in the visible range (ca. 45 % of the solar spectrum), most of these semiconductors need of an external potential (bias) to promote the oxygen evolution reaction on its surface, due to the position of their conduction and valence bands [20]. This limitation restricts the use of these materials in a practical way, so the search for new materials is still under study.

In this context, molybdenum oxides emerge as interesting materials for the fabrication of photo-anodes, since it has been observed that: (i) molybdenum trioxide (MoO_3) films have good electrochromic and photochromic properties, and (ii) molybdenum dioxide (MoO_2) has an unusual metal-like electrical conductivity [21][22]; added to the relatively earth-abundance of molybdenum [23].

PEC photo-anodes are fabricated by several methods successfully. Two of them are electrodeposition and spin-coating. Regarding electrodeposition, this technique can be implemented as a simple, scalable and inexpensive method of producing these types of electrodes. In this context, it is widely accepted that some factors such as the type of sustrate, electrolyte properties and electrodeposition parameters (such as current density, time, electrode potential), have a direct influence on the morphological and photo-electrochemical properties of the semiconductor films obtained. In this method, the understanding of the thermodynamic stability of the aqueous electrolyte involved is essential for the engineering of these parameters, and therefore, reaching higher solar-to- hydrogen conversion efficiencies (STH) in photo-electrochemical cells containing these photo-electrodes [24]. On the other hand, spin-coating is a technique for deposition of thin uniform films onto the substrates. This technique is attractive for the manufacture of photo-anodes for the following reasons: good homogeneity, easy control of the composition, processing at low temperatures, large coating area, possibility of mixing and doping oxides with other materials, control of the microstructure of deposited coatings, good optical properties and low cost of the equipment since it is not required to use systems to reach high vacuum [25] [26] [27].

1.4. Hypothesis

Photo-electrochemical cells offer a promising method to produce hydrogen directly driven by the use of solar energy. In fact, the anode or/and the cathode of these cells are manufactured using semiconductors that are capable of absorbing the energy of the photons in the ultraviolet and visible wavelength regions, promoting the water splitting reaction. In this respect, molybdenum oxides have recently emerged as a promising alternative in the search of new semiconductor materials to fabricate photo-electrodes, since it has n-type semiconduction, relative band edge positions in aqueous electrolytes and band-gap energy values (Eg >1.23 eV) suitable for harvesting enough energy to drive the oxygen evolution reaction

(OER) in a water splitting photo-electrochemical cell [24]. Additionally, it has been reported that impurities such as nickel or tungsten (oxides) co-deposited with molybdenum oxides on FTO-coated glass can improve the photo-electrochemical properties of the films obtained and their catalytic activity for the oxygen evolution reaction [28] [29]. In this context, this doctoral thesis has been focused on the synthesis of semiconductor materials by two different routes: (i) electrodeposition and (ii) spin-coating. Therefore, the following hypothesis has been formulated:

- Molybdenum oxides films (MoO_x) produced on fluorine-doped tin dioxide (FTO)-coated glass absorb photons with energies in the UV and visible wavelength ranges of the solar spectrum and, moreover, impurities such as nickel or tungsten (oxides) co-deposited with MoO_x could improve the photo-electrochemical properties of the films obtained and their catalytic activity for the OER. Therefore, it is expected that fabrication of photo-anodes for water splitting in photo-electrochemical cells can be accomplished by this means.

1.5. General Aim

Energy and environment are undoubtedly fundamental worldwide concerns nowadays. Consequently, the development of technologies that enable energy production from renewable sources (such as solar radiation) with low or zero greenhouse gases emissions is important and timely to study.

The efficient conversion of solar energy to electrical energy is strongly associated with the energy storage capacity of the technology employed, due to the diurnal and seasonal intermittency of solar irradiation. Hydrogen appears as a promising storage alternative, since it can be produced from water (an abundant resource in Earth) and used in a fuel cell stack or other similar device to produce electrical energy with zero greenhouse emissions.

The general aims of this research work has been to synthesize and characterize the performance of photo-anodes based on molybdenum oxides for the production of hydrogen in a photo-electrochemical cell from water electrolysis.

Chapter 2

Fundamentals Review

This chapter presents a review of the theoretical aspects associated with the operation of a photo-electrochemical cell (electrochemistry, photo-chemistry and semiconductor physics), together with the fundamentals of the synthesis techniques used in this thesis.

2.1. Thermodynamics of Electrochemical Processes

2.1.1. Cell Potential and Free Energy

The maximum amount of work, W_{max}, that can be produced by an electrochemical cell is equal to the product of the cell potential, E_{cell}, and the total charge transferred, $\nu_e F$, during the reaction [30][31]:

$$W_{max} = -\nu_e F E_{cell} \tag{2.1}$$

By convention, the work is expressed as a negative number because it is done by a system on its surroundings [30].

The change in Gibbs free energy, ΔG, is also a measure of the maximum amount of work that can be performed during a chemical process ($\Delta G = W_{max}$). Therefore, there is a relationship between the potential of an electrochemical cell and ΔG:

$$\Delta G = -\nu_e F E_{cell} \tag{2.2}$$

When the reaction is carried out under standard conditions, equation 2.2 takes the following form:

$$\Delta G^{\circ} = -\nu_e F E^{\circ}_{cell} \tag{2.3}$$

A spontaneous redox reaction is characterized by a negative value of ΔG, which corresponds to a positive value of E_{cell}.

2.1.2. Nernst Equation

In general, two types of processes occur in the electrode | electrolyte interface:(i) faradaic and (ii) non-faradaic. The first are those where the transfer of electrons through the electrode | electrolyte interface involves a change in the oxidation state of some species, that is, there is a proportionality between the current that passes through the system and the reacted amount of active material on the electrode (Faraday's law) [32]. On the other hand, non-faradaic processes involve changes in the structure of the electrode | electrolyte interface by varying the applied potential, mainly due to adsorption and desorption of electrochemical species [33]. This chapter is focused mainly on the faradaic processes.

The electrochemical kinetics and thermodynamics related to faradic processes can be analyzed considering the following general reaction:

$$O + \nu_e e^- \leftrightharpoons R \tag{2.4}$$

The free energy change, ΔG, as a function of the activities of the species in the reaction, is given by the following equation [33]:

$$\Delta G = \Delta G^{\circ} + RTln\left[\frac{a_R}{a_O}\right] \tag{2.5}$$

Substituting the equations 2.2 and 2.3 into equation 2.5 gives:

$$-\nu_{\mathrm{e}} F E_{cell} = -\nu_{\mathrm{e}} F E^{\circ}_{cell} + RTln\left[\frac{a_R}{a_O}\right] \tag{2.6}$$

By dividing both sides of this equation by $-\nu_{\mathrm{e}} F$, it is possible to obtain the Nernst equation:

$$E_{cell} = E^{\circ}_{cell} + \frac{RT}{\nu_{\mathrm{e}} F} ln\left[\frac{a_O}{a_R}\right] \tag{2.7}$$

In equilibrium, that is when there is no external current flow, the Nernst equation allows describing the potential (also known as Nernst potential,E_N) as a function of the activities of the electroactive species [34].

2.1.3. Gibbs Free Energy of Formation and Standard Hydrogen Electrode

The Gibbs free energy of formation of a compound i, $\Delta G^{\circ}_{f,\mathrm{i}}$, is the change of Gibbs free energy that accompanies the formation of 1 mole of a substance in its standard state from its constituent elements in their standard states [35]. The utility of this energy is to be able to calculate the ΔG_{rxn} of any chemical reaction using the equation:

$$\Delta G_{rxn} = \sum_{\mathrm{i}} \nu_{\mathrm{i}} \Delta G^{\circ}_{f,\mathrm{i}} \tag{2.8}$$

The ΔG°_f of the elements in their more stable allotropic states are equal to zero, since these are used as a reference. The free energies of ion formation must also be compared to a reference that has charge. The proton, H^+, is assigned the value $\Delta G^{\circ}_{f,H^+} = 0$. A negative reference is also needed, which is the electron: $\Delta G^{\circ}_{f,\mathrm{e}^-} = 0$.

Considering the above, the semi-reaction:

$$H^+ + \mathrm{e}^- \leftrightarrow \frac{1}{2} H_2 \tag{2.9}$$

has $\Delta G^{\circ}_{semirxn} = \frac{1}{2}\Delta G^{\circ}_{f,H_2} - \Delta G^{\circ}_{f,H^+} - \Delta G^{\circ}_{f,\mathrm{e}^-} = 0$. Using equation 2.3 it is possible to obtain the following expression:

$$E^{\circ}_{N,H^+/H_2} = 0 \tag{2.10}$$

The above means that, given the free energy of formation conventions, the half-reaction of proton reduction in hydrogen is assigned the value of 0 V in the standard potential. If this semi-reaction occurs in an electrode of an electrochemical cell with unit activities for the protons (pH = 0) and for the hydrogen (fugacity of 1 atm), this is known as a standard hydrogen electrode (SHE) [35].

2.1.4. Redox Stability of Species in Aqueous Solution: Pourbaix and Latimer Diagrams

The Pourbaix diagram is a plot of potential versus pH that shows zones for thermodynamic stability of different species at fixed concentrations and temperature [36]. That a species appears in a region of the diagram does not imply that this is the only existing species, but that it is the most abundant stable form.

Since this speciation occurs in aqueous solution, the oxidizing and reducing character of water must be considered:

$$2H^+_{(aq.)} + 2\mathrm{e}^- \leftrightarrow H_{2(g)} \qquad E^{\circ} = +0{,}00\ V\ vs\ SHE \tag{2.11}$$

$$\frac{1}{2}O_{(g)} + 2H^+_{(aq.)} + 2\mathrm{e}^- \leftrightarrow H_2O_{(l)} \qquad E^{\circ} = +1{,}23\ V\ vs\ SHE \tag{2.12}$$

From the Nernst equations for each of these semi-reactions at 298 K and 1 atm and with activities different to the unity, we have the following:

$$E_{N,H^+/H_2}/(V\ vs\ SHE) = 0{,}00 - 0{,}0591pH \tag{2.13}$$

$$E_{N,O_2/H_2O}/(V\ vs\ SHE) = 1{,}23 - 0{,}0591pH \tag{2.14}$$

In the Pourbaix diagram, lines 2.13 and 2.14 are usually plotted. Both are parallel to each other and delimit an area that is known as the water stability field, as can be seen in the example diagram in Figure 2.1. If the experimental conditions are in the zone delimited by these two lines, then the water does not react transferring electrons. If the conditions are above the stability zone, the water is oxidized (Reaction 2.12 occurs to the left), reducing the dissolved species and evolving oxygen. Conversely, if they are under the zone of stability, then the protons present due to the autoionization of the water are reduced (Reaction 2.11 to the right), oxidizing the dissolved species and evolving hydrogen.

A Latimer diagram is another way to show species stability in a summarized way. Latimer or reduction potential diagrams show the standard reduction potentials connecting various

oxidation states of an element [39][40]. Figures 2.2 and 2.3 show, as an example, molybdenum diagrams.

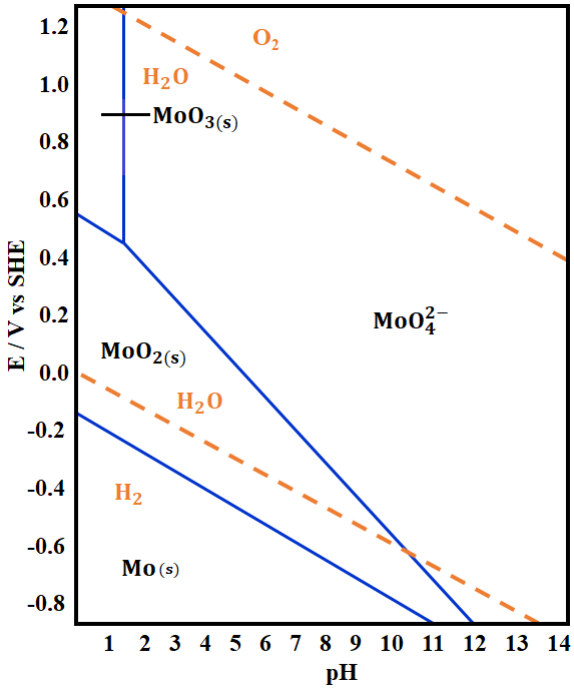

Figure 2.1: Pourbaix diagram of the molybdenum-water system. Adapted from [37]

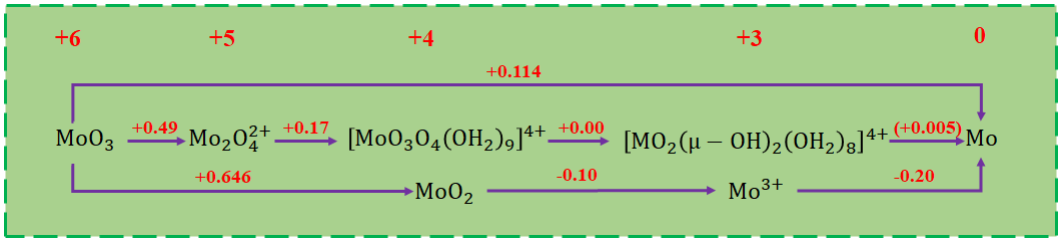

Figure 2.2: Latimer diagram of the molybdenum-water system in an acid medium. Adapted from [38]

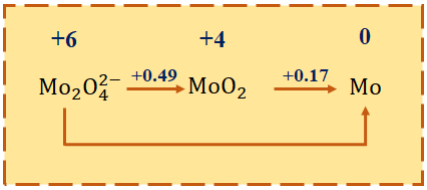

Figure 2.3: Latimer diagram of the molybdenum-water system in a basic medium. Adapted from [38]

From these diagrams it is possible to predict the redox behaviour of a given species. The more positive the standard reduction potential, more readily the species on the left is reduced to the species on the right side of the arrow. Therefore, highly positive standard reduction potentials indicate that the species at the left is a good oxidizing agent. Negative standard reduction potentials indicate that the species to the right behaves as a reducing agent.

2.2. Kinetics of Electrochemical Processes

When a chemical reaction involves species of different phases (such as in electrodeposition or water electrolysis processes) we have a heterogeneous reaction. This type of reactions happen by mechanisms that involve both diffusive and chemical reaction processes. It is fundamental to have complete understanding of the global phenomenon, because, if a reaction is the product of a sequence of steps, the reaction rate will be determined by the rate of the slowest stage, that is, the controlling stage.

2.2.1. Transport Processes in Electrochemical Systems

In the electrolyte of an electrochemical cell, mass transfer occurs in the aqueous solution by three different mechanisms: (i) diffusion, (ii) convection and (ii) migration [39].

- Diffusion: Is the displacement (the motion) of any species in solution, as the result of a concentration/pressure gradient [39].

- Migration: Concerns only charged species (anions and cations), and corresponds to the displacement of an ion in solution resulting from an electrical field [39].

- Convection: Is the motion of any species within a solution arising from the motion of this solution (turbulent, laminar). The motion can be caused:(i) by the agitation (stirring-flowing) of the solution, (ii) by the motion of the electrode (rotation, formation of a deposit, flowing of a liquid or semi-solid electrode, etc.), (iii) by a difference of the temperature which introduce a difference of density in two areas of the bulk, and (iv) by a difference of the concentration (at the interface electrode | bulk for example), which also introduce a difference of density [39].

In an electrochemical reaction, the transport of species to and from the electrode | electrolyte interface is important to maintain the transfer of electrons and is a necessary step for any electrochemical reaction. Moreover, it is one of the most preponderant factors in determining the speed at which the process is carried out.

Making a mass balance of the electroactive charged species, ν_{e}, in an element of infinitesimal volume of solution we have the following:

$$\frac{\partial c_{\mathrm{i}}}{\partial x} = \nu_{\mathrm{e}} u_{m,\mathrm{i}} F \nabla \left(c_{\mathrm{i}} \nabla \Phi\right) + D_{\mathrm{i}} \nabla^2 c_{\mathrm{i}} - \nabla c_{\mathrm{i}} \mu \tag{2.15}$$

The first term on the right of equation 2.15 is the rate of migration in an electric field (in case the species is not ionic, this term is null), the second term is associated with the diffusion driven by concentration gradients, and the third term corresponds to the transport by convection.

The diffusivity, D_{i}, can be expressed by the Stokes-Einstein equation [40]:

$$D_{\mathrm{i}} = \frac{k_B T}{6\pi\mu r_{\mathrm{i}}} \tag{2.16}$$

- At high temperatures (T), the species have larger internal energy and, therefore, are able to move with larger kinetic energy.

- The dynamic viscosity, μ, of the medium is linked to the magnitude of the intermolecular forces existing in the solvent. In other words, the dynamic viscosity (also known as absolute viscosity) is the measurement of the fluid's internal resistance to flow.

- The hydraulic radius, r_{i}, of the particle that diffuses is inversely proportional to its diffusivity, since the smaller the better is its ability to permeate through the spaces between the solvent molecules.

2.2.2. Current-Overpotential Equations

Any electrochemical reaction either produce or consume electrons, thus the rate of electron flow to or from a reacting interface is a measure of reaction rate. Faraday's Law allows to relate the mass and electron fluxes of a single reaction, such as 2.4, so the current, I at an anode (A) or cathode (C) is a direct measure of the (area) specific reaction rate (r):

$$r_{A/C} = \frac{\left|I_{A/C}\right|}{A_{A/C} \cdot \nu_{\mathrm{e}} \cdot F} \tag{2.17}$$

Dividing the current by an electrode's geometric area defines the current density, related directly to the specific reaction rate:

$$r_{A/C} = \frac{\left|j_{A/C}\right|}{\nu_{\mathrm{e}} \cdot F} = k_{A/C} \cdot c_{\mathrm{red/ox}} \tag{2.18}$$

Therefore, the partial current densities j_A and j_C can be defined as a function of the cathodic and anodic reaction rates:

$$\left|j_{A/C}\right| = r_{A/C} \cdot \nu_{\mathrm{e}} \cdot F \tag{2.19}$$

The rate coefficients $k_{A/C}$ exhibit an experimental dependence on driving forces / overpotentials:

$$k_A = k^{\circ} exp\left(\frac{(1-\alpha) \cdot \nu_{\mathrm{e}} \cdot F \cdot \eta}{R \cdot T}\right) \tag{2.20}$$

$$k_C = k^{\circ} exp\left(-\frac{\alpha \cdot \nu_{\mathrm{e}} \cdot F \cdot \eta}{R \cdot T}\right) \tag{2.21}$$

Where overpotentials, η, are defined by :

$$\eta = E_{semirxn} - E^{\circ} \tag{2.22}$$

In equations 2.20 and 2.21, α is the transfer coefficient and k° is called standard electrochemical kinetic constant, which is the same for both reaction rates [34].

At equilibrium no *net* current flows to or from the surface of the electrodes. This, however, does not mean that nothing is happening in the electrochemical cell. A "dynamic equilibrium" condition exists, where the net currents in electrochemical reactors must sum to zero to conserve charge (Kirchoff's 1st law):

$$j_{net} = j_A + j_C = 0 \tag{2.23}$$

Solving equations 2.18 and 2.23 gives:

$$j_{net} = k^{\circ} F exp\left(\frac{(1-\alpha)\cdot \nu_{\mathrm{e}} \cdot F \cdot \eta}{R \cdot T}\right) c_{\mathrm{red}} - k^{\circ} F exp\left(-\frac{\alpha \cdot \nu_{\mathrm{e}} \cdot F \cdot \eta}{R \cdot T}\right) c_{ox} \tag{2.24}$$

Factoring by $k^{\circ} F$:

$$j_{net} = k^{\circ} F \left[exp\left(\frac{(1-\alpha)\cdot \nu_{\mathrm{e}} \cdot F \cdot \eta}{R \cdot T}\right) c_{\mathrm{red}} - exp\left(-\frac{\alpha \cdot \nu_{\mathrm{e}} \cdot F \cdot \eta}{R \cdot T}\right) c_{ox}\right] \tag{2.25}$$

Equation 2.25 is known as the current-overpotential relationship.

Another useful form of this equation (more details in bibliography [31]) is known as the Butler-Volmer equation:

$$j_{net} = j_o \left[exp\left(\frac{(1-\alpha)\cdot \nu_{\mathrm{e}} \cdot F \cdot \eta}{R \cdot T}\right) - exp\left(-\frac{\alpha \cdot \nu_{\mathrm{e}} \cdot F \cdot \eta}{R \cdot T}\right)\right] \tag{2.26}$$

where, j_o, is a parameter known as the exchange current density. The exchange current density corresponds to the current at equilibrium, i.e. the rate at which oxidized and reduced species transfer electrons with the electrode. In other words, the exchange rate is the rate of reaction at the reversible potential (when the overpotential is zero by definition).

2.3. Electrodeposition Processes

Deposits of photo-active materials with varied morphologies (thin dense films or nanostructured arrays) and, therefore, active surface areas have been synthesized on different substrates (titanium foil, sheets or FTO-coated glass) by spray-pyrolysis, chemical vapor deposition

(CVD), electrodeposition processes, drop-casting or spin-coating. The photo-anodes obtained by these different routes present diverse photon absorption, charge separation and catalytic oxygen evolution properties and, consequently, different photo-current densities are produced by each of them when operating at similar conditions.

Electrodeposition provides a simple, cheap, scalable and manufacturable fabrication method of semiconducting materials [41]. In this context, it is widely accepted that factors such as the electrolyte properties (concentrations of precursors and other compounds dissolved, solvent, pH), the type of substrate, and the electrodeposition parameters (electrode potential, current density, time), influence the morphological and photo-electrochemical properties of the generated semiconducting deposits (films) [41]. The understanding of the thermodynamic stability of the aqueous electrolyte involved is crucial for the engineering of these parameters, and thus reaching higher solar to- hydrogen conversion efficiencies (STH) in photo-electrochemical cells containing these photo-electrodes [42].

In general, in the electrodeposition of a compound of interest in an electrochemical cell the phenomenology can be described by the following steps:

1. The precursor species is dissolved in the electrolyte and moves towards the boundary layer.

2. The precursor species penetrates the boundary layer and reaches the solid | liquid interface.

3. The species is adsorbed on the surface, either in the substrate or in the solid already deposited, with chemical reaction with charge transfer (redox reaction).

4. The adsorbed species diffuses on the surface.

5. When the species finds a growth site (minimum energy gap in the surface of the substrate that provides larger stability) it is incorporated into the deposit.

Figure 2.4 shows steps mentioned above:

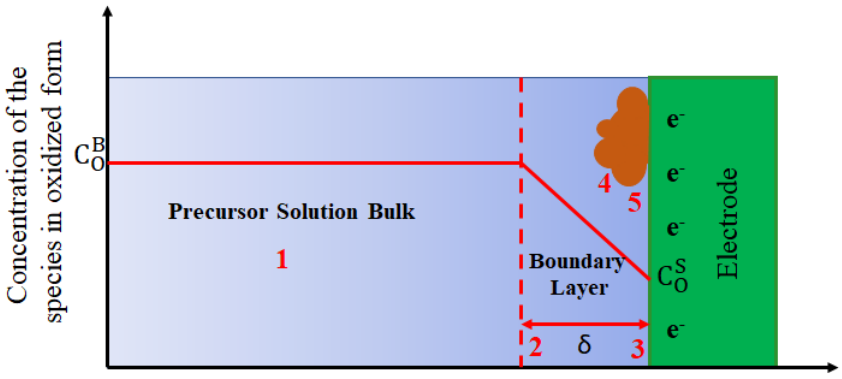

Figure 2.4: General stages of the electrodeposition process.

2.4. Spin-Coating: An Alternative to the Electrodeposition Processes

Large scale fabrication of photo-anodes by electrochemical methods offers advantages over other techniques since the successful scale up of electrochemical synthesis processes is confirmed by numerous industrial applications, such as the electrolytic production of pure metals. The above is one of the motivations of this research project which is mainly focused on the manufacture of photo-anodes based on molybdenum oxides through electrodeposition. However, spin-coating was considered as an alternative synthesis method in order to compare the results obtained by both approaches and enrich the discussion.

One of the most popular low-cost techniques for the preparation of thin films is spin-coating. The main advantage of spin-coating is its ability to quickly and easily produce very uniform films, ranging from a few nanometres to a few microns in thickness [43]. The fundamentals of this technique will be reviewed in this section, which will help to a better understanding and interpretation of the results discussed in Chapter 6.

This technique generally involves the application of a thin film (a few nm to a few μm) evenly across the surface of a substrate by coating (casting) a solution of the desired material in a solvent while it is rotating [43].

Generally, spin coating can be broken down into four key stages:(a) deposition, (b) spin-up, (c) flow domination and (d) evaporation. These stages are schematized in Figure 2.5 [64]. The first three are commonly sequential, but flow domination and evaporation usually overlap [43].

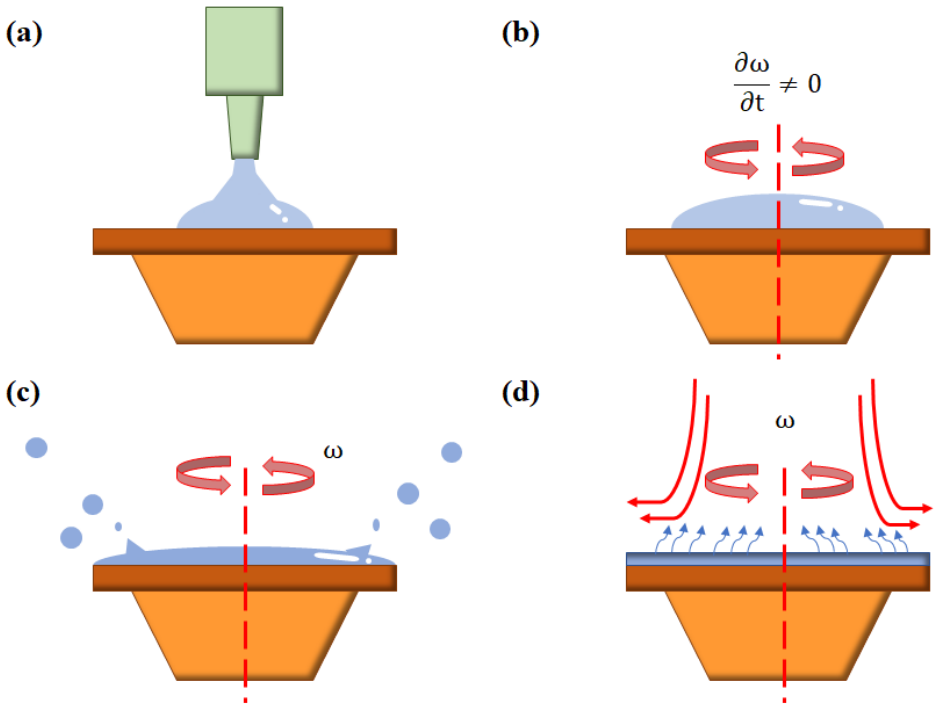

Figure 2.5: General diagram of the Spin Coating process.

1. Deposition: In this stage, the coating solution material is applied on the of substrate surface as illustrated in Figure 2.5(a). The amount of applied liquid depends on the viscosity of the liquid and the size of the substrate to be coated.

2. Spin-up: In the second stage of the spin-coating process, the substrate is accelerated up to its final, desired, rotational speed. As can be seen in the Figure 2.5(b), in this stage liquid is spread over the substrate surface by centrifugal force. The spinning speed is set at a specific value depending on the desired film thickness.

3. Flow domination: The third stage of a spin-coating process corresponds to the spinning of the substrate at a constant rate and fluid viscous forces dominate the gradual thinning of the deposited layer (Figure 2.5(c)).

4. Evaporation: In the final stage, evaporation of the solvent takes over as the primary mechanism of thinning as can be seen in Figure 2.5(d). During this stage centrifugal out flow stops and further shrinkage is due to solvent loss. The above causes the formation of thin film on the substrate. During the evaporation stage the suspended or dissolved solids may grow so concentrated at the liquid surface as to form a high viscosity, low diffusivity layer or solid skin.

2.5. Semiconductor Materials

Materials can be classified according to their resistivity in conductors, semiconductors and insulators. Semiconductor materials are used in the manufacture of photo-electrodes. These types of materials are insulators with a band-gap that allows electronic transitions from the valence band to the conduction band; its conductivities result of the movement of excess electrons or holes (electron-vacancies) in a semiconductor lattice [44].

Semiconductors with holes as majority charge carriers are known as p-type semiconductors, whereas those with excess electrons as charge carriers are known as n-type semiconductors.

2.5.1. Band-Gap

Intrinsic semiconductors are materials that have full energy levels (valence band) and empty energy levels (conduction band) [44] [45]. These bands are separated by an area in which it is not possible for an electron to remain because of a lack of energy states. This area is known as a band-gap. The width of this band defines the electronic characteristics of the material and determines the sensitivity of the semiconductor to irradiation at a certain wavelength. The energy difference that defines this band-gap, usually ranges between 1 to 4 eV [46].

As can be seen in Figure 2.6, if the value of the band-gap is greater than 4 eV, the material is a dielectric or insulator, and if the value of the band-gap is close to zero it is a conductor. In any other circumstance the material is a semiconductor [47].

When a semiconductor absorbs solar irradiance, an excited electron-hole pair will be generated. The probability of finding an electron in a given state can be modelled by the

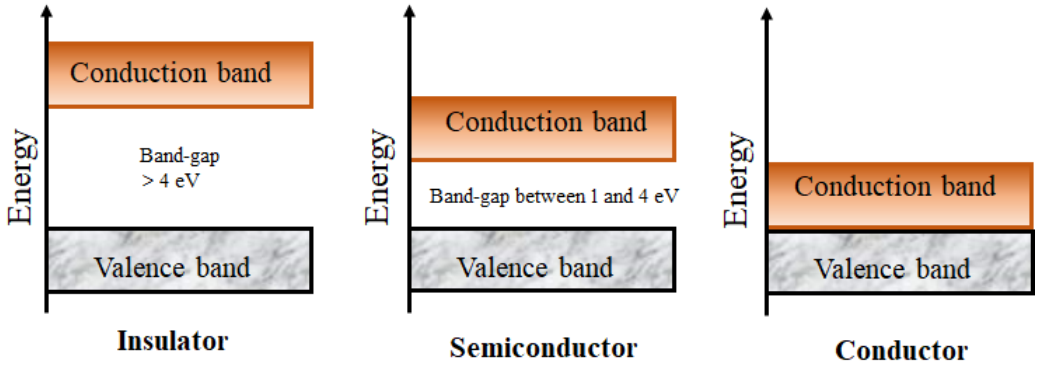

Figure 2.6: Materials classified according to their conductivity.

Fermi-Dirac[4] distribution in which the Fermi level is defined as the energy level at which the probability of finding an electron is 0.5. It is important to note that n-type semiconductors have Fermi levels closer to their conduction band, while p-type semiconductors have Fermi levels closer of their valence band [49].

2.5.2. Flat-Band Potential

Flat-band potential corresponds to the Fermi level on an electrochemical scale within a semiconductor electrode under no band bending conditions (no potential difference between the surface and the bulk energy bands) [42]. For instance, the energies of bands of isolated semiconductors in vacuum are 'flat', i.e. do not depend on position relative to the semiconductor | vacuum interface. However, when a semiconductor is in electrical contact with an electrolyte solution or another semiconductor, the Fermi levels in the two congruous phases equilibrate by transfer of charge, causing the bands to bend across the space charge region $|e\phi_{sc}|$, as illustrated in Figure 2.7.

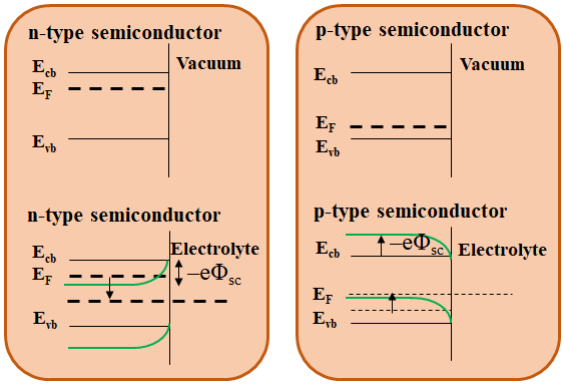

Figure 2.7: Curvature of semiconductor bands in contact with electrolytes: (i) n-type and (ii) p-type [42].

[4]The statistical mechanics of Fermi-Dirac is applied mainly to subatomic particles and very particularly to electrons, which are governed by the Pauli exclusion principle according to which only two electrons (with opposite spin) can occupy the same quantum state [48].

By changing the potential of the electrode, it is possible to manipulate the degree of band bending. In the case of a n-type semiconductor, when the applied potential is negative to the flat-band potential, an accumulation layer is formed, in which electrons (majority charge carriers) accumulate at the semiconductor surface. On the other hand, if the applied electrode potential is positive to the flat-band potential, a depletion layer is formed, in which the majority charge carriers at the surface is small but still significant. When a larger positive potential is applied to the semiconductor, an inversion layer will be formed, in which the concentration of minority charge carriers (holes) will be dominant at the surface [42].

2.6. Water Splitting and Photo-Electrochemical Cells

As stated in Section 1.3, to promote the water splitting reaction (equation 1.2) according to the half-reactions (equations 1.3 and 1.4) a potential of at least 1.23 V must be applied between the electrodes (anode and cathode).

In the case of a photo-electrochemical cell, the anode or/and the cathode are fabricated using semiconductor materials which are capable of absorbing the energy of photons in the ultraviolet and visible wavelength regions and use them to promote reaction(s) 1.3 or/and 1.4) at the electrode | electrolyte interface(s)[5]. Figure 2.8 shows a schematic of the band-edge energy levels of an ideal semiconductor anode material for water splitting [6], at which two key aspects can be observed: (i) the band-gap energy (E_g) of this material is larger than 1.23 eV, and (ii) the valence and conduction band-edge energies (E_{vb} and E_{cb} , respectively) are below and above the electrochemical equilibrium potentials $E^0_{298K}(O_2/H_2O)$ and $E^0_{298K}(H^+/H_2)$ for half-reactions 1.3 and 1.4, respectively.

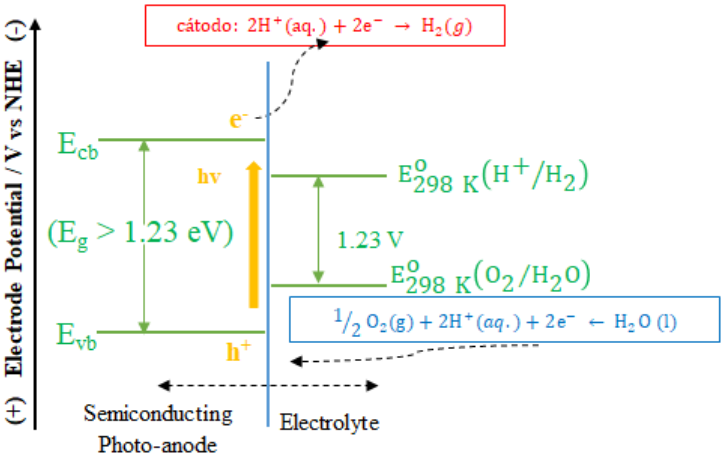

Figure 2.8: Schematic of the band-edge energy levels of an ideal semiconducting photo-anode material for water splitting. Half-reaction equilibrium potentials vs NHE (normal hydrogen reference electrode).

[5]The semiconductor must absorb radiant light with photon energies of >1.23 eV, which is equivalent to wavelengths of ca. 1,000 nm and shorter (ultraviolet and visible wavelength regions) [16].

[6]Similarly, a schematic for the band-edge energy levels of an ideal semiconducting cathode material can be conceived, but it is not presented in this Ph.D thesis since its aim is to fabricate a semiconducting photo-anode.

These conditions have to be satisfied by the semiconductor anode material in order to: (i) promote the oxygen evolution reaction (OER) at the electrode | electrolyte interface by means of the electron holes generated in the semiconductor valence band by absorption of the energy of sunlight (photons), and (ii) generate electrons with energies high enough to promote the hydrogen evolution reaction (HER) at the cathode surface.

In Figure 2.9, the band-gap limits of some semiconductor materials studied as photo-anodes and photo-cathodes are illustrated.

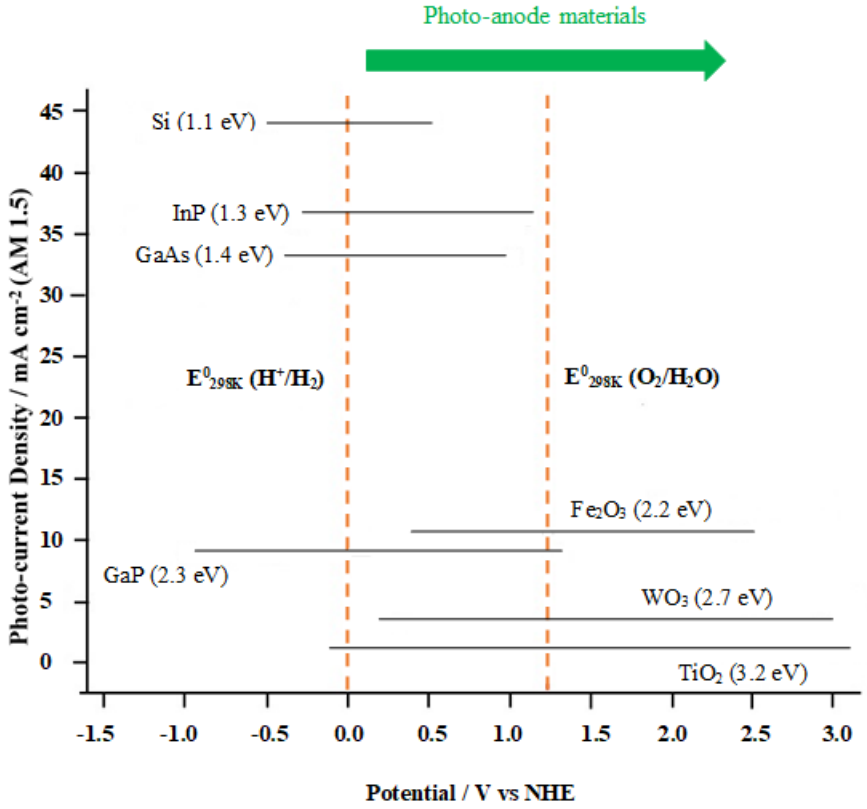

Figure 2.9: Conduction band (left dots line) and valence band (right dots line) position vs NHE (normal hydrogen reference electrode) of some common semiconductors used in PECs [16].

Chapter 3

Literature Review

This chapter reviews the main aspects of photo-electrochemical processes for water splitting, emphasizing the semiconductor materials most commonly used in the production of photo-anodes, such as : (i) titanium dioxide (TiO_2), (ii) hematite (α-Fe_2O_3) and (iii) tungsten trioxide (WO_3), and materials that seems an attractive alternative, such as molybdenum oxides (MoO_x).

3.1. Photo-electrochemical Cells

In a photo-electrochemical cell one or both electrodes are made of semiconductor materials, which convert incident photons to electron–hole pairs [50]. These electrons and holes migrate in opposite directions to the electrode surface [50][51]. In the case of a photo-anode, the photo-generated electrons are swept toward the conducting backcontact and transported to the counter-electrode via an external wire. At the counter-electrode, the electrons reduce water to form hydrogen gas. On the other hand, the created holes on the valence band are swept toward the semiconductor | electrolyte interface, where they oxidize water to form oxygen gas [50].

As mentioned in section 1.3, in order to promote the direct chemical decomposition of water into hydrogen and oxygen in a PEC a potential difference of at least 1.23 V needs to be supplied to the system, which corresponds to the minimum potential that has to be applied between the electrodes (anode and cathode) of an electrochemical cell to promote the water splitting reaction. Figure 3.1 shows a schematic of a photo-electrochemical cell (PEC) used for water splitting with a photo-anode in acid solution.

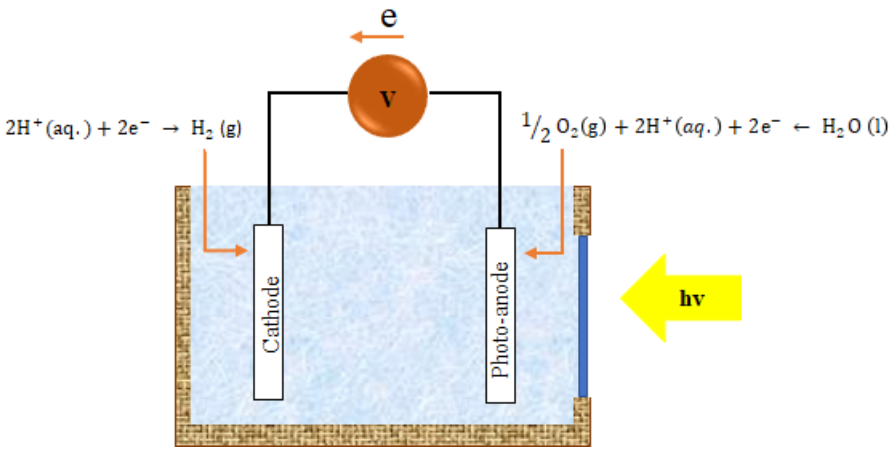

Figure 3.1: Diagram of a simple photo-electrochemical cell [85].

3.2. Design and Fabrication of Photo-Electrochemical Cells

Research on photo-electrochemical systems has been focused mainly on the improvement of the performance and durability of photo-electrode materials. The design of an electrochemical cell is also fundamental to maximize the overall efficiency of conversion / production of the process and achieve its economic viability. In the case of photo-electrochemical cells, the efficient production of hydrogen from the hydrolysis of water depends strongly on the manufacturing process of a photo-electrode that complies with the basic characteristics which are mentioned in section 3.1. Usually, a photo-electrochemical cell would need at least a window which allow illumination into the reactor and one or two photoactive electrodes, as illustrated in Figure 3.1. Next, photo-electrochemical cells with different design will be discussed.

In the study and search of suitable materials for photo-electrodes, the cappuccino cell [52],

which is illustrated in Figure 3.2, is an excellent alternative since this type of devices generally works with small photo-electrodes areas (ca. $\sim$ 0.5 cm^2). Most cells use either platinum wire or platinised titanium as the counter-electrode in order to minimise the overpotential required for hydrogen evolution. Due to the electrode area is all so small, the effect of potential distribution is insignificant.

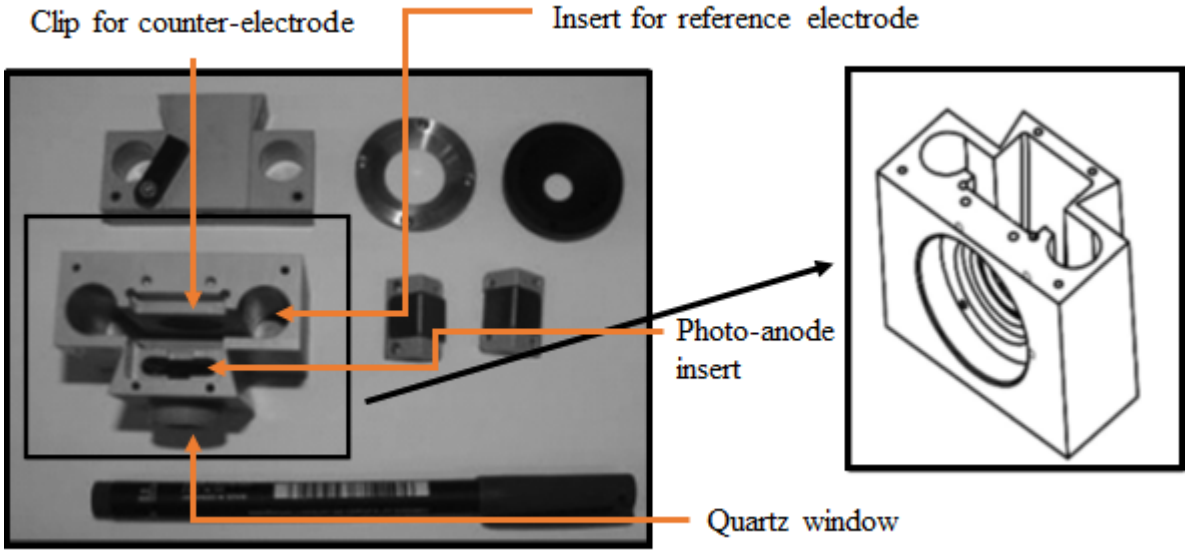

Figure 3.2: Components of the cappuccino photo-electrochemical cell [52].

A photo-electrochemical cell of a single compartment, batch type, will only be sufficient for laboratory scale material testing, but if this technology is to be deployed at the industrial level, flow reactors need to be considered. Currently, most photo-catalytic reactors are used in the water treatment industry where dissolved organics in waste water are oxidised using particulate semiconductors [53][54]. As can be seen in Figure 3.3, these systems can be easily operate in a fluidised bed reactor with UV lamp illuminated from inside of an annular column or illuminated from the outside[89]. Unfortunately, having the product gas, particles, and liquid all mixed in the reactor, the separation process will prove to be challenging.

The simplest design of a photo-electrochemical cell would be to use planar and parallel electrodes with a membrane separating the anolyte and catholyte [55][56]. As shown in Figure 3.4, a possible planar electrode design [53] is to have an assembly of a few plates which forms different compartments and meshing a membrane in between. This kind of design is easy to fabricate and modification on the cell such as addition or removal of a compartment can be easily made. However, this cell or reactor design present a slight disadvantage, which is that the multiple joints will serve as possible spots for liquid and gaseous leaks [57].

Two types of photo-electrochemical cells have been developed by Midwest Optoelectronics [58]: (i) the immersion-type as shown in Figure 3.5 and (ii) the substrate-type as illustrated in Figure 3.6. The immersion type cell suggests the use a bipolar type of electrode, where the surface facing the top would be the photo-anode, while the opposing surface would be the cathode. In this cell, having the membrane installed perpendicular to the electrodes would also create possibly an uneven potential distribution due to the long proton path (assuming

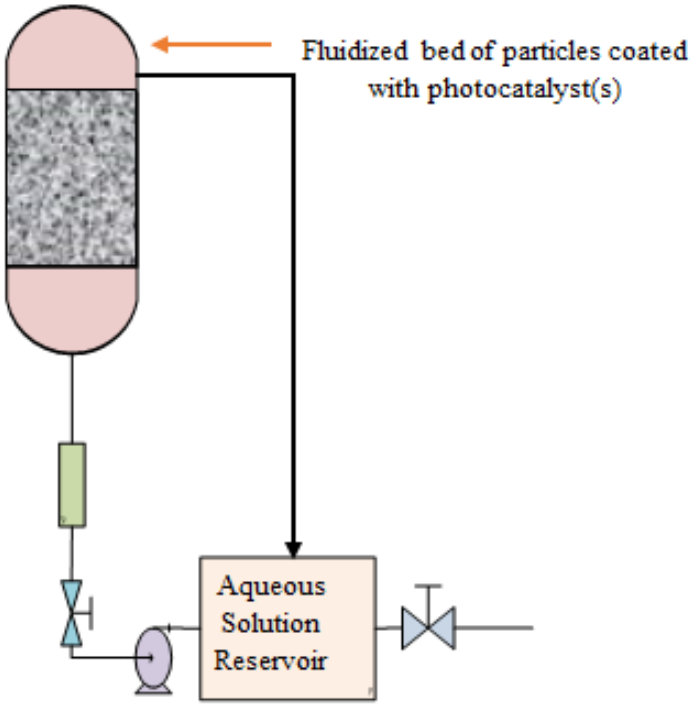

Figure 3.3: Schematic of a fluidised bed cell loaded with semiconductor particles [89].

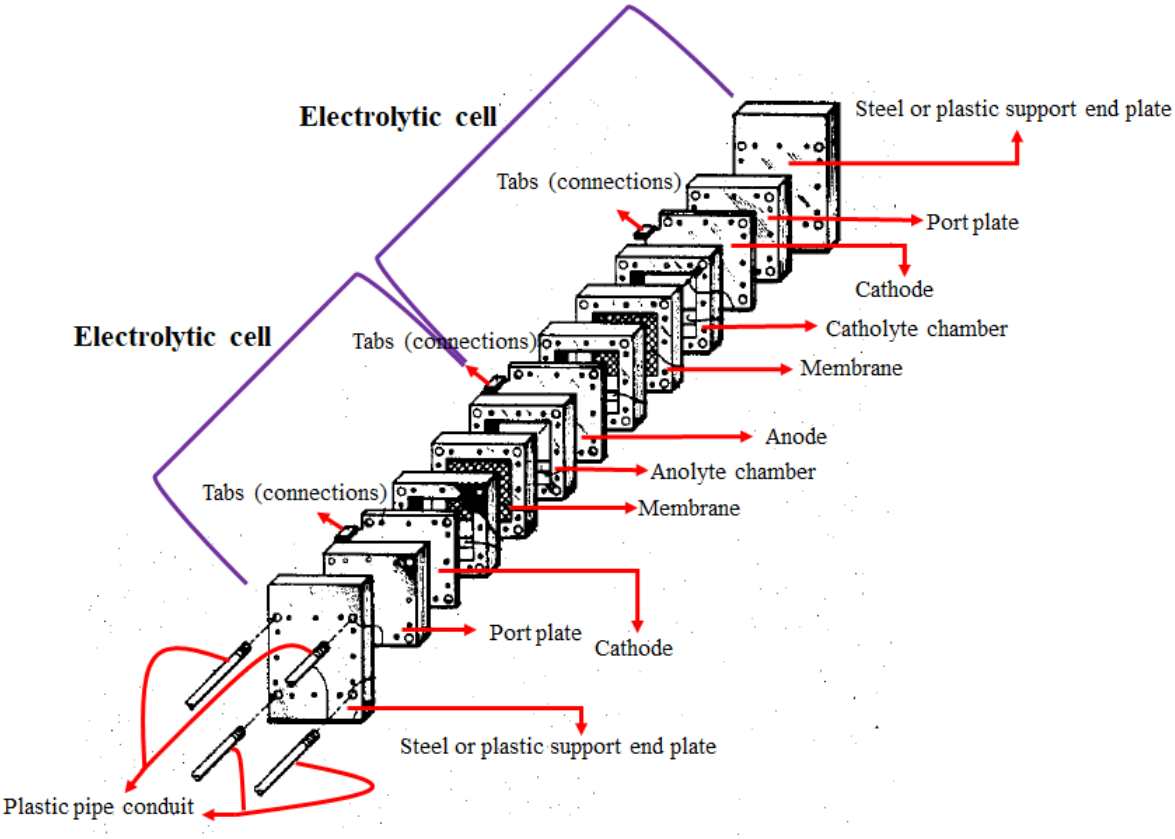

Figure 3.4: Exploded view of a multiple plate electrochemical reactor assembly [57].

acidic electrolyte), and hence reducing the efficiency of the reactor, as suggested by Haussener *et al.* [59]. In the case of substrate-type photo-electrochemical cell design, the photovoltaic material is deposited on top of a hydrogen evolution catalyst such as Co:Mo. Unfortunately, as both the immersion and substrate type reactor designs are top facing, the gas bubbles could get trap on the top surface of the cell and electrodes could cause an increase in interfacial resistance. On the other hand, the effect of trapped bubbles on the performance of the cell would be more significant for the immersion type reactor, where the bubbles will cause light scattering, thus reducing the incident photon flux to the photo-anode.

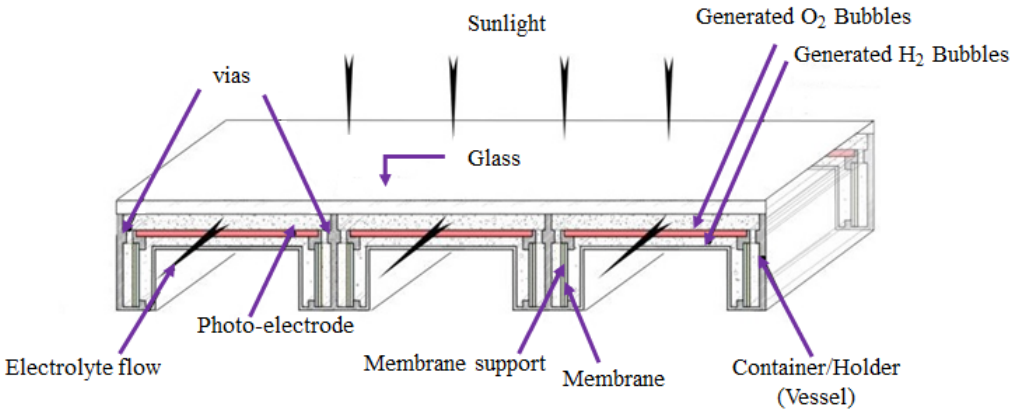

Figure 3.5: Immersion type photo-electrochemical cell [58].

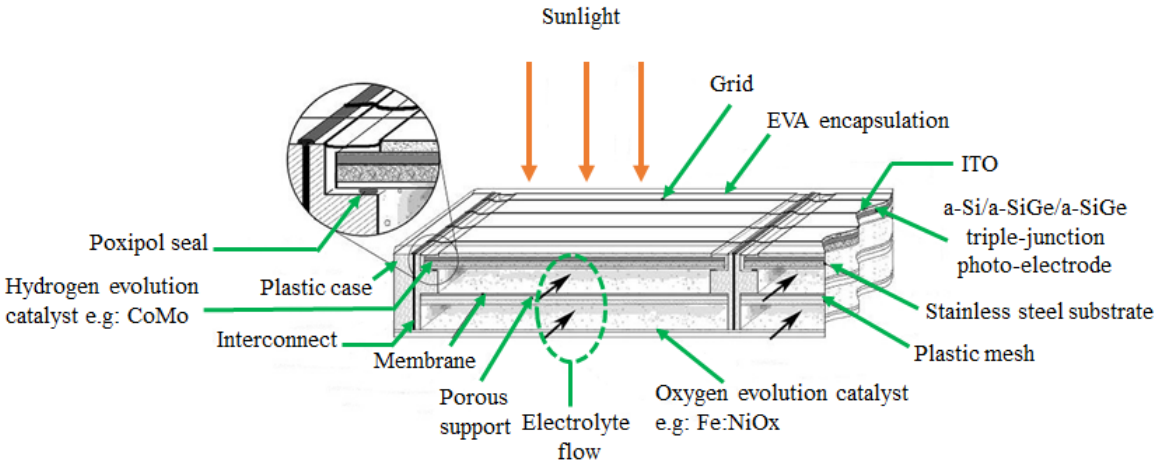

Figure 3.6: Substrate type photo-electrochemical cell [58].

Fan *et al.* invented a photo-electrochemical cell that uses a mirror to illuminate the cell from both sides [60]. This device is illuminated on one of its faces directly with sunlight, while on the opposite side a mirror is placed perpendicular to the direction of the light beams in order to reflect the light towards the cell and use the photons more efficiently. This is very useful in a system where a photo-anode and photo-cathode is used. This concept is based on to having the electrolyte at the core of the cell, separated by membrane where photo-anode is deposited at one side while the photo-cathode at the other side as can be seen in Figure 3.7. In this type of cell, the reaction would be highly limited by mass transport of the electrolyte/water through the membrane and to the electrodes for reaction to take place.

Linkous and Slattery [61] designed a double bed photo-electrochemical system as can be seen in Figure 3.8. In this design, using a pump the electrolyte can flow through the chambers (anodic and cathodic) where the oxygen and hydrogen evolution are carried out separately. This system has several disadvantages, such as an uneven potential and current distribution, moreover it will also have mixture of oxygen, hydrogen and lower conversion efficiency due to the recycle of the electrolyte.

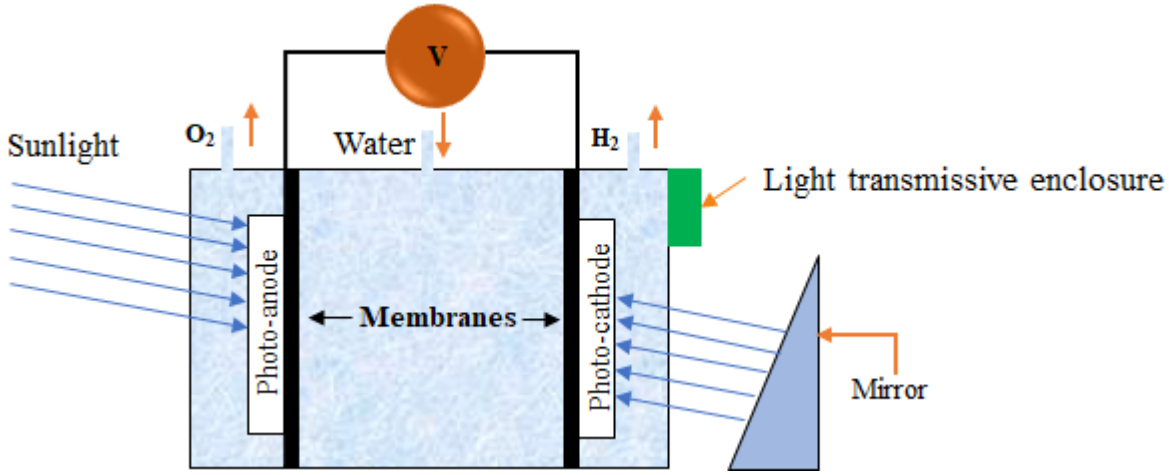

Figure 3.7: Schematic of a photo-electrochemical cell which utilises a mirror to illuminate both sides of the system [60].

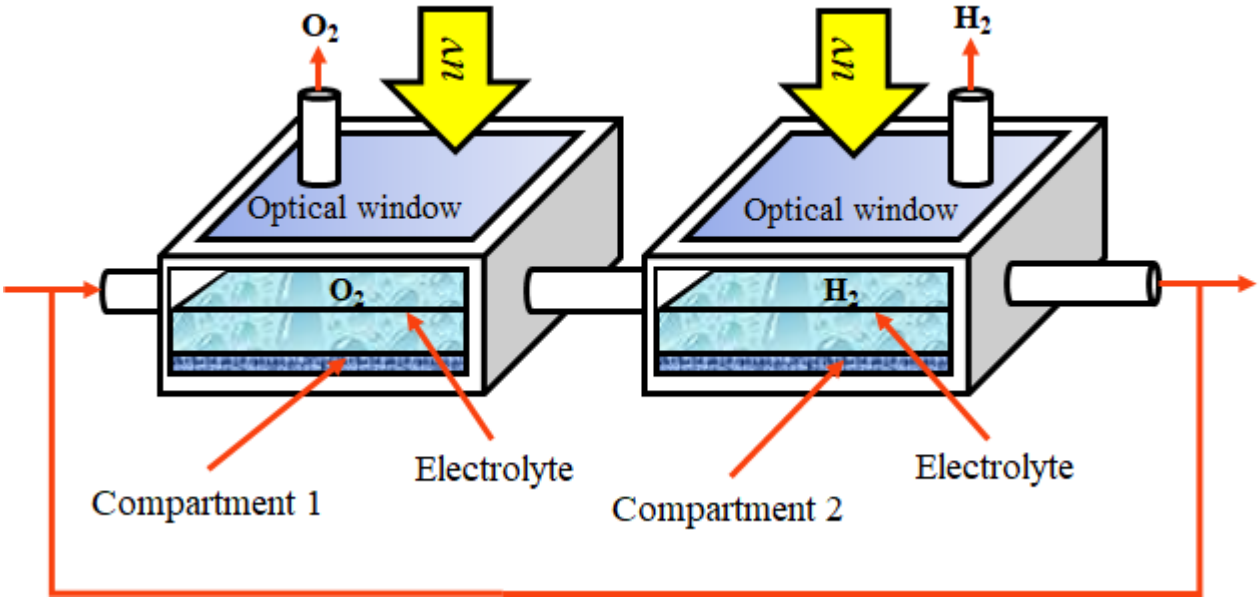

Figure 3.8: Concept design of a dual bed photo-electrochemical cell [61].

Aroutiounian *et al.* proposed an improved dual-bed cell where the electrolyte is separated by a membrane as illustrated in Figure 3.9 [62]. Unlike the cell described above, instead of a flat optical window, a light-concentrating optical window and a light-focusing parabola is

used to maximise the photon flux into the cell. Nevertheless, this setup does not improve the potential distribution.

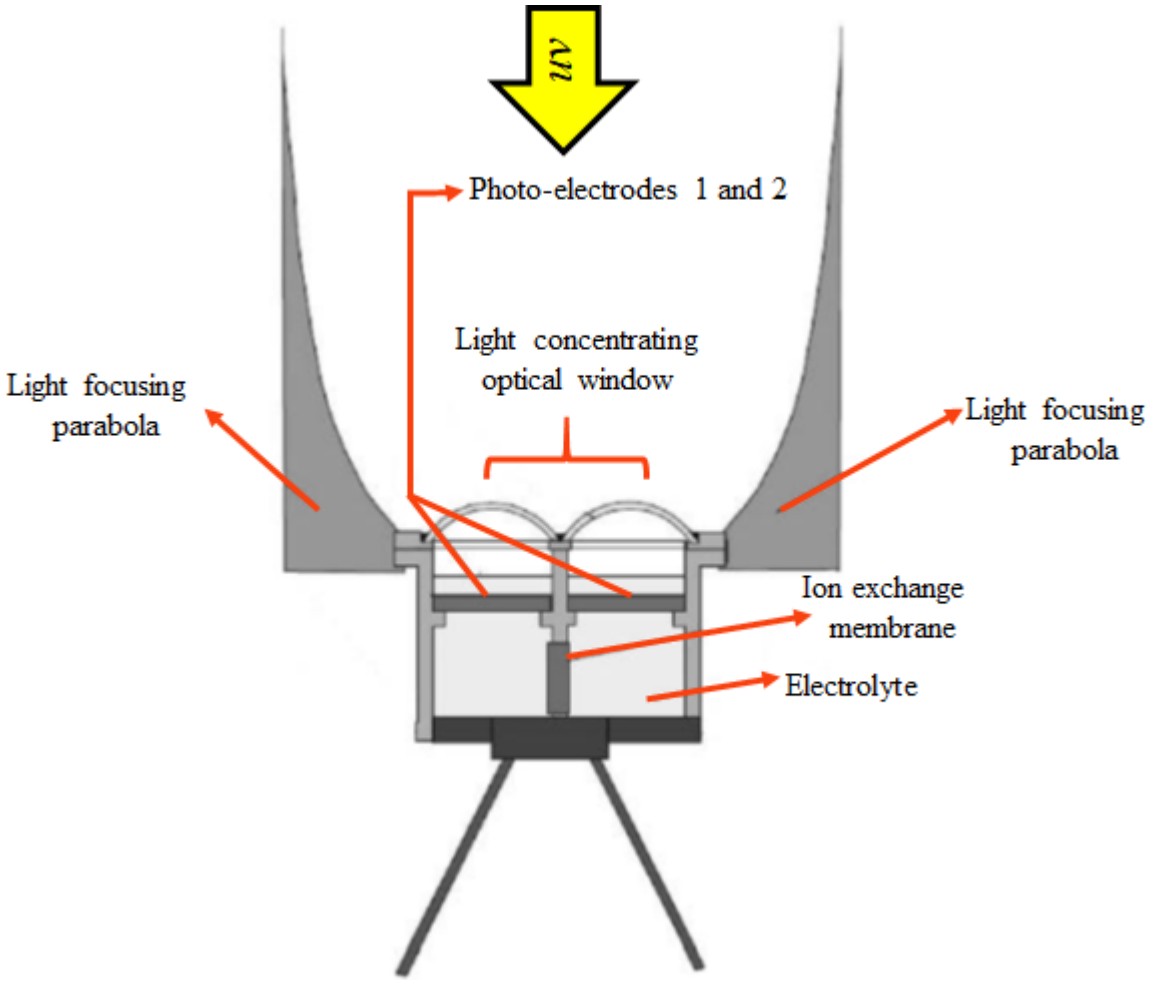

Figure 3.9: Improved dual-bed cell with light-concentrating optical window [62].

Kelly and Gibson also used the same concept of utilising a curved surface to provide intensified photon flux onto an immersed PV-electrolyser reactor system in a folded plastic (polyester) bag and divided fish bowl reactor (Figures 3.10 and 3.11) [63]. Plastic bags or fish bowls would make an interesting alternative as material for a photo-electrochemical cell since these devices are very cheap. Nevertheless, as the suggested cell system requires approximately 19 litres of 5 M of KOH solution as electrolyte, the mechanical stability of the plastic bags may not be strong enough to hold the weight of the highly alkaline electrolyte and will be a potential hazard. On the other hand, having the PV panel immersed in the electrolyte in this type of cells, the semiconductor needs to be well insulated from the electrolyte in order to avoid degradation of the PV semiconductor material, this makes implementing these devices less viable.

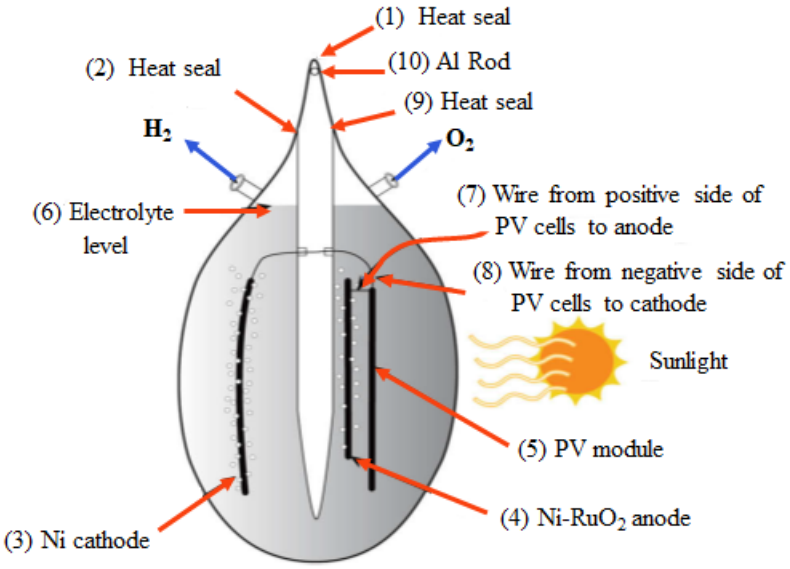

Figure 3.10: Schematic diagram of a folded plastic bag PV-electrolyser cell system [63].

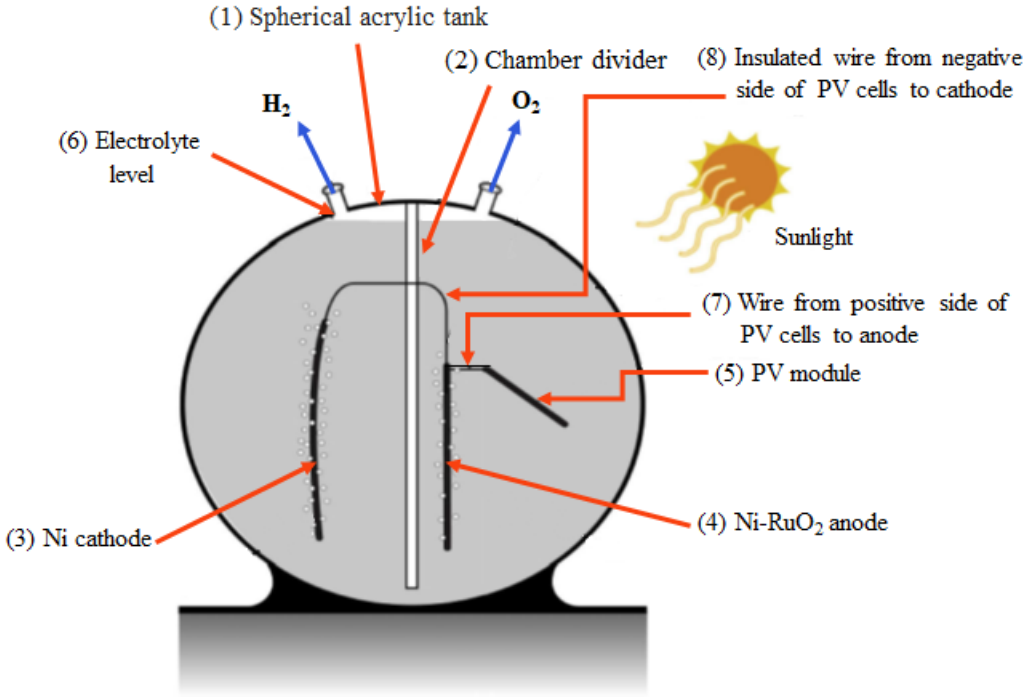

Figure 3.11: Schematic diagram of a fish bowl PV-electrolyser cell system [63].

A more practical alternative of a photo-electrochemical cell which utilises focused and intensified light would be a design which uses fibre optic light guide [64][65]. In this setup, the fibre optic light guide will be coated externally with photo-anode material, in contact with electrolyte solution, enclosed with a membrane sheath. A porous metal cathode which has electrical continuity can be made on the membrane as shown on Figure 3.12. The cell can be scaled-up by having a bundle of these electrode modules in a manifold arrangement as ilustrated the Figure 3.13. It is also possible to scale the cell in the direction of length,

but this would depends highly of the conductivity and characteristics of the photo-anode material.

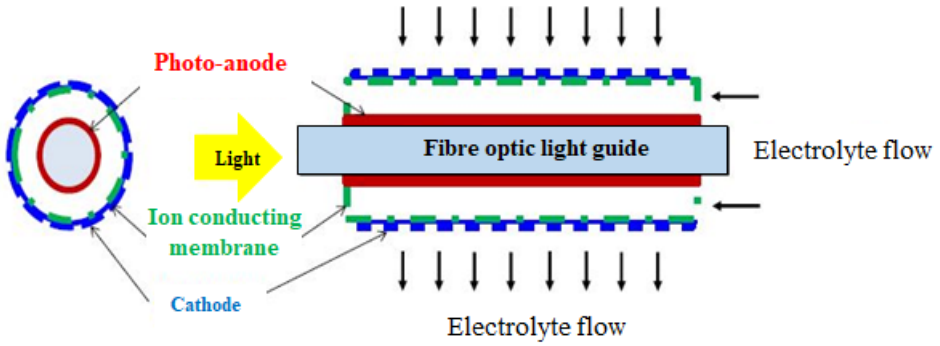

Figure 3.12: Cross sectional area and schematic of a single fibre photo-electrochemical cell module [64][65].

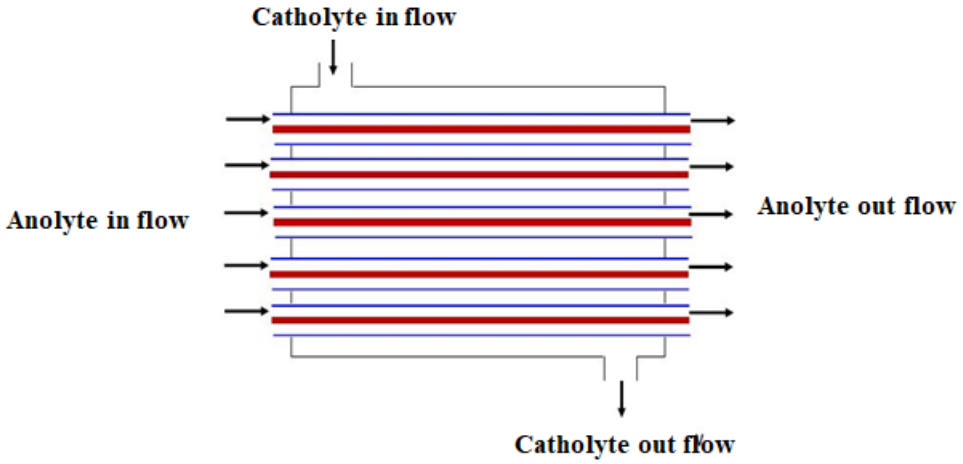

Figure 3.13: Schematic of a photo-electrochemical cell with multiple modules of fibres [64][65].

3.3. Semiconductor Materials for Photo-Electrochemical Processes

Photo-electrochemical cells with semiconductor electrodes in electrical contact with a conductive substrate (back contact) have been considered for an efficient water splitting. In the case of semiconductor electrodes, radiation absorption, carrier production and water oxidation/reduction reactions take place in the same semiconductor material. The photo-electrode surface plays thus a seminal role and particular care should be devoted to surface morphology and defective sites [66].

The design of semiconductor photo-electrodes must consider that a significant fraction of the incident solar energy has to be absorbed for the activation of water oxidation/reduction reactions. Besides, for these technology to be deployed at large scale globally, semiconductor materials need to be low-cost and earth-abundant.

3.3.1. Materials for Photo-Anodes

For the photo-anodes production, three materials have received special attention for the fabrication of photo-anodes for photo-electrochemical cells: (i) titanium dioxide (TiO_2), (ii) hematite (α-Fe_2O_3), and (iii) tungsten trioxide (WO_3), which are n-type semiconductor and stable under oxygen evolution conditions. The details of these materials will be discussed further in this section.

3.3.1.1. Titanium dioxide, TiO_2

Titanium dioxide has been considered as a promising photo-anode material for the photo-electrochemical production of hydrogen from water splitting, due to its resistance to dissolution in aqueous environments and under oxygen evolution, which can be inferred from the analysis of the potential-pH diagram in Figure 3.14. However, the band-gap energy of titanium dioxide is 3.2 eV (as can be seen in Figure 2.9), which determines that only ca. 3 % of the energy in the solar spectrum (mainly the UV wavelength region) will be able to promote the formation of the electron-electron hole pairs necessary for the oxygen evolution reaction to occur (see Figure 2.8)[20]. In addition, some researchers have shown that due to the position of the valence and conduction band-edge energies of titanium dioxide (see Figure 2.9), it is not possible to promote the unassisted photo-electrolysis of water in a photo-electrochemical cell using TiO_2 photo-anodes [67], but an external electrical or chemical bias (e.g. pH difference between anolyte and catholyte) is required to drive the water splitting process [108]. There have been many attempts to change the band structure of TiO_2, so absorption of solar radiation in the visible light wavelength range and unassisted water splitting are possible. Some results reported in the literature have shown that introducing impurities such as zinc, chromium, molybdenum, carbon or nitrogen into the TiO_2 lattice, the band-gap of the material can be decreased to enable absorption of photons in the visible light wavelength range [67] .

3.3.1.2. Hematite, α-Fe_2O_3

Hematite is a cheap and abundant mineral, which has been widely studied as a photo-anode material for PECs since it can absorb up to 30 % of the energy in the solar spectrum (band-gap energy of 2.2 eV as illustrated in the Figure 2.9), and has good photo-electrochemical stability and chemical inertness over a wide range of pH and under oxygen evolution conditions, according to the potential-pH diagram in Figure 3.15 [68] [69]. However, as with TiO_2, α-Fe_2O_3 is not able to promote the unassisted photo-electrolysis of water at its surface under illumination, due to its conduction band-edge energy level. Moreover, studies have shown that the photo-current densities generated in PECs with α-Fe_2O_3 photo-anodes are quite low due to: (i) the high recombination rates of photo-generated electrons and electron holes [70], and (ii) the slow electron exchange rate between water and the photo-anode surface [71]. In this respect, impurities such as tin, titanium, silicon and zinc have been incorporated in the α-Fe_2O_3 lattice to create surface defects or trapped states which decrease the electron-electron hole recombination rates. Furthermore, α-Fe_2O_3 doped with silicon, tin or titanium presents higher electron exchange rates between water and the photo-anode surface [72]. Photo-current densities produced by PECs with α-Fe_2O_3 photo-anodes can also be increased by addition of oxygen evolution catalysts such as iridium oxide or cobalt phosphate on the surface of the photo-anode, which decrease the applied to equilibrium potential difference (overpotential)

required to evolve oxygen and hence lower the bias (auxiliary potential) required to promote the unassisted water splitting in a PEC [73][69].

3.3.1.3. Tungsten trioxide, WO_3

Tungsten trioxide is among the most popular candidates to fabricate photo-anodes for PECs, together with TiO_2 and α-Fe_2O_3. Although WO_3 is stable only in acidic conditions (pH below ca. 4.0, as can be seen in Figure 3.16) and presents a band-gap energy of 2.7 eV (according to Figure 2.9), so it is able to capture a maximum of 10 % of the energy in the solar spectrum, its popularity is due to the slow recombination rate of photo-generated electrons and electron-holes. Similarly to TiO_2 and α-Fe_2O_3, the conduction band-edge energy of WO_3 is not high enough to promote the spontaneous splitting of water to produce oxygen and hydrogen, so impurities have to be introduced to the WO_3 photo-anode structures. For example, a photo-current increase of ca. 20 % at an applied potential of 1.6 V vs SCE reference electrode has been measured when using WO_3:Mo|WO_3 bi-layer structures as photo-anodes, compared to pure WO_3 photo-electrodes [73][69][74].

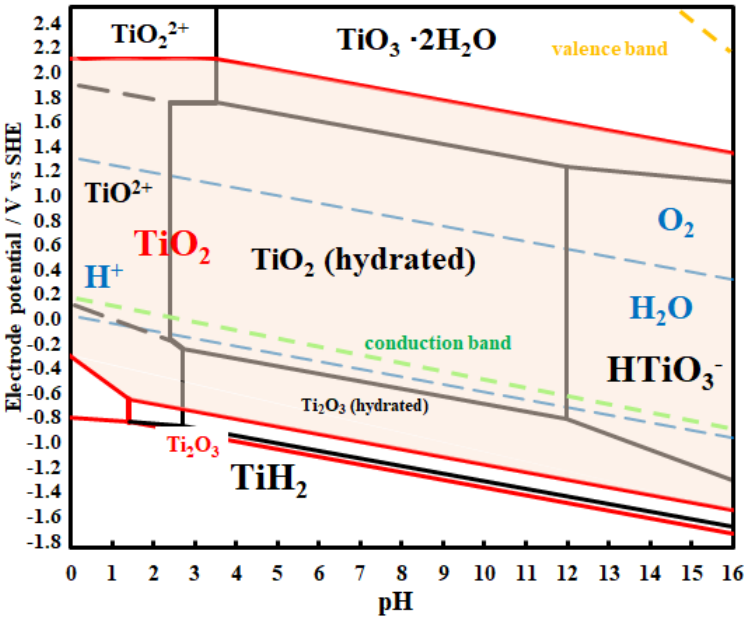

Figure 3.14: Potential-pH diagram of the system titanium-oxygen-hydrogen at 298 K, 1 atm and 10^{-6} dissolved species activities. Red lines for anhydrous oxides and black lines for (metastable) hydrated oxides [75]. SHE: Standard Hydrogen Reference Electrode.

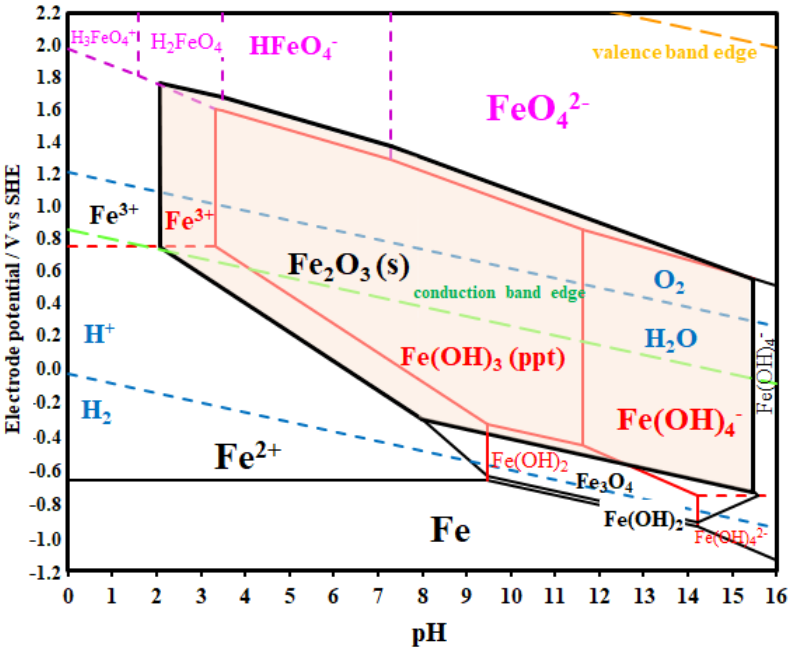

Figure 3.15: Potential-pH diagram of the system iron-oxygen-hydrogen at 298 K, 1 atm and 10^{-6} dissolved species activities. Red lines for anhydrous oxides and black lines for (metastable) hydrated oxides [75]. SHE: Standard Hydrogen Reference Electrode.

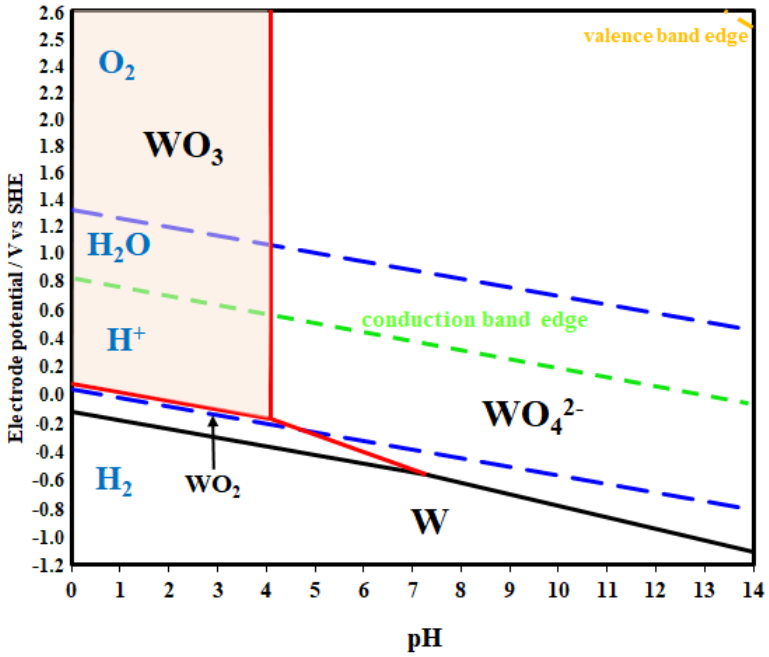

Figure 3.16: Potential-pH diagram of the system tungsten-oxygen-hydrogen at 298 K, 1 atm and 10^{-6} dissolved species activities. Red lines for anhydrous oxides and black lines for (metastable) hydrated oxides [75]. SHE: Standard Hydrogen Reference Electrode.

3.3.2. Materials for Photo-Cathodes

The operation of a photo-electrochemical cell is not limited to the use of only photo-anodes materials. As different materials have been studied for the synthesis of photo-anodes, materials have also been studied to produce photo-cathodes, which can be used in a cell with a traditional anode (e.g. platinum) or a photo-anode. Generally, semiconductors as GaAs, GaP and Si are doped to produce p-type semiconductor and can act as a photo-cathode. However they are not stable under hydrogen evolution conditions and the cost of making these materials are relatively high [74].On the other hand, metal oxides are considered cheaper materials, but most of this type of oxides are n-type semiconductors. Cu_2O is among the few metal oxides which exhibit p-type semiconductor properties, it's band-gap is ca. 2 – 2.2 eV, but the potential-pH diagram (Figure 3.17) of Cu_2O shows that it is not stable under oxygen and hydrogen evolution condition. Paracchino e*t al.* [76] reported that nanolayers of Al-doped zinc oxide and titanium oxide are capable of increase the life span of Cu_2O from ca. 5 minutes to about an hour [77].

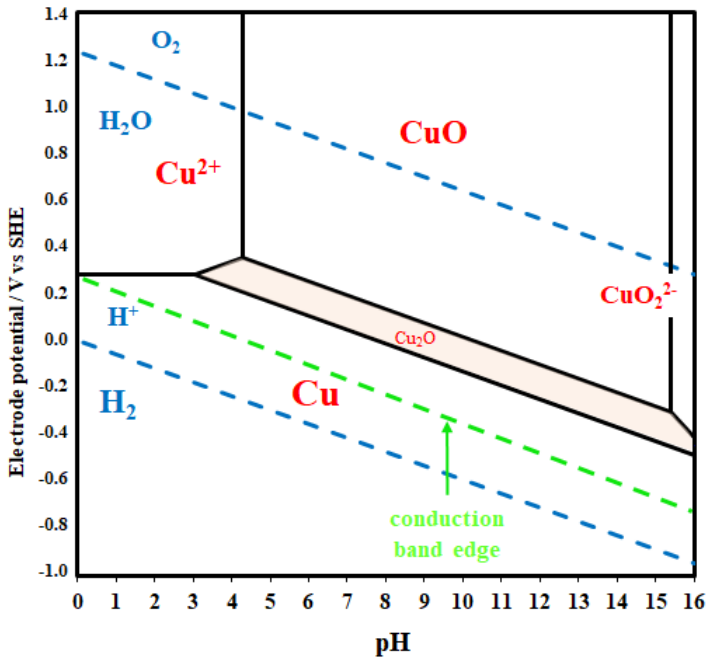

Figure 3.17: Potential-pH diagram of the system copper-oxygen-hydrogen at 298 K, 1 atm and 10^{-6} dissolved species activities [75].

3.4. Molybdenum Oxides and Synthesis Methods

Presently, molybdenum oxides have recently emerged as a promising alternative in the search of new semiconductor materials to fabricate photo-electrodes for driving the water splitting reaction [78] [79].It has been reported that some compounds of the MoO_x family present:(i) stability under acidic conditions (as can be seen in Figure 3.18), (ii) n-type semi-conduction [21] (iii) relative band edge positions in aqueous electrolytes [80] and ban-dgap energy values [21][81] (E_g >1.23 eV) suitable for harvesting enough energy to drive the oxygen evolution reaction (OER) in a water splitting photo-electrochemical cell [81] [17].

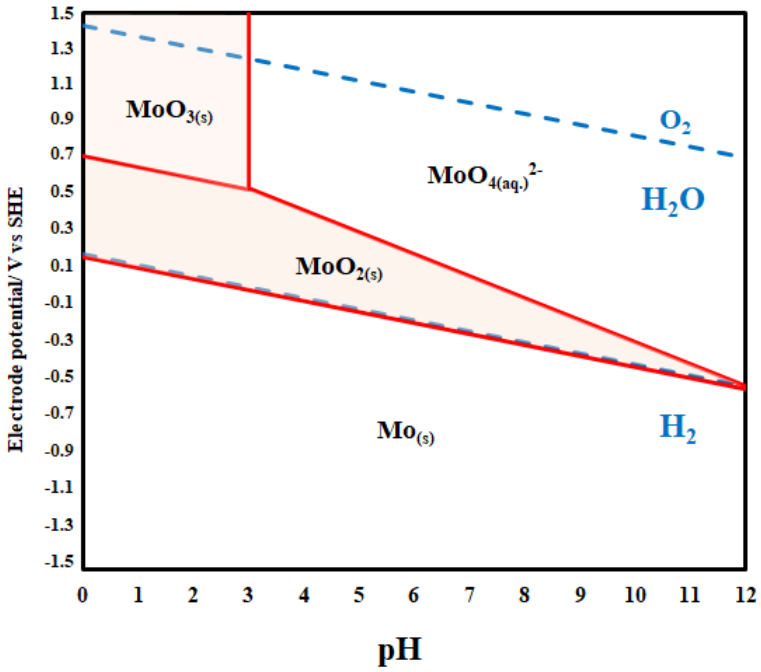

Figure 3.18: Potential-pH diagram of the system Molybdenum-Oxygen-Hydrogen at 298 K, 1 atm and 10^{-6} dissolved species activities [75]. SHE: Standard Hydrogen Reference Electrode.

Many deposition techniques, such as evaporation [82], chemical vapor deposition [83], sputtering [84][85] and various wet chemistry methods, such as sol–gel spin coatings processes [86], electrodeposition [24], spray pyrolysis [87], have been used to prepare MoO_x films. Among these, the electrodeposition and spin-coating techniques provide a simple, cheap and scalable way of manufacturing semiconductor materials. Next, the state of the art of the production of thin films of molybdenum oxides by electrodeposition and spin-coating methods is presented.

Shembel e*t al.* performed the electrodeposition of thin films of molybdenum oxides on steel [88] by varying the molybdenum precursor solution: the first was an aqueous solution saturated in ammonium molybdate $(NH_4)_6Mo_7O_{24}$, (with pH between 6.5 y 7.0), and the second one was sodium molybdate, Na_2MoO_4. The current densities used were invariant on the time (potentiometries) and comprised between 10 and 15 mA cm^{-2}. The films obtained contained non-stoichiometric oxides of the form $MoO_x{\cdot}nH_2O$ with x in the range 2.75-2.88 and n between 1.33-1.38.

Patil e*t al.* reported the structural and optical properties of molybdenum oxide thin films electrodeposited on FTO-coated glass from alkaline aqueous solutions of ammonium molybdate at room temperature [81]. The results obtained showed the formation of hydrous and amorphous $MoO_{2-n}(OH)_{2n}$ films, which turns into polycrystalline MoO_2 when annealed in dry argon at 450 °C for 1 hour. The changes in crystallinity and composition affected the optical absorption properties of the molybdenum oxide deposits obtained (ca. 219 nm thickness), whose band-gap narrowed from 2.64 eV to 2.58 eV when annealed.

Dukstiene e*t al.* reported the structural, optical and photo-electrochemical properties of

MoO_2 thin films electrodeposited on Se-SnO_2-coated glass and SnO_2-coated glass from alkaline solutions of sodium molybdate at room temperature, introducing sodium citrate as intermediary of the electrodeposition reaction [21]. The results obtained showed the formation of anhydrous and amorphous MoO_2 films, with a band-gap that goes from 2.53 eV to 2.38 eV depending on the electrodeposition potential applied (from -1.0 V to -1.2 V). The electrodes produced by this means showed an increase in the open circuit potential of ca. 0.31 V and photo-current generation when comparing their electrochemical behavior in the dark and under UV-illumination. Finally, a proposed band-gap model of the photo-electrodes fabricated suggest that unassisted photo-electrochemical oxygen evolution from water splitting is possible in a PEC with MoO_2-based photo-anodes in alkaline solutions.

On the other hand, considering that pure molybdenum cannot be electrodeposited from aqueous solutions, the co-deposition of this metal with other metals such as nickel and/or tungsten to produce metallic alloys has been widely studied [28] [29]. For instance, the use of nickel as a catalyst has stood out during the last years, with several applications [89]. It is well known that the presence of nickel in electrodes provides catalytic activity for both the oxygen and hydrogen evolution reactions in aqueous solution, which in addition with the properties mentioned at the beginning of section 3.4. for molybdenum oxides makes attractive the idea of studying photo-electrodes based on mixed molybdenum-nickel oxides.

An example that exposed above, is the research of Kuznetsov e*t al*. who studied the deposition processes of nickel-molybdenum alloys from ammonia-citrate solutions [90][91][92]. The dependence of the current and the chemical composition of cathodic deposits with the electrolysis time were studied under potentiostatic conditions [92]. The results obtained can conditionally be divided into two types: (i) at potentials less than –0.93 V vs SHE, a decrease in the current is observed with increasing electrolysis time, which is associated with the blockage of the electrode surface by molybdenum oxides; (ii) at potentials higher than –0.93 V vs SHE, in the course of the first few seconds a slight decrease in the current occurs, which is followed by an increase associated to the formation of a nickel–molybdenum alloy, $[NiCitMoO_2]_{ads}$, on the cathode.

Morales e*t al*. proposed a speciation model for the Mo(VI)-Ni(II)-citrate-S(VI)-N(III)-H_2O system and it was solved for a set of concentrations, varying the amount of Mo(VI) and Ni(II) and the pH of the solution, to obtain diagrams of predominance and distribution [24]. The plots obtained were used to discuss and choose adequate conditions for the electrodeposition process of molybdenum and nickel oxides films, which suggests that a pH = 9.0 and $pC_{Mo(VI)}$ = $pC_{Ni(II)}$ = 2.0 were recommendable when pC_{cit} =$pC_{S(VI)}$ = $pC_{N(III)}$ =1.0 was fixed. Additionally, Eh-pH diagrams for nickel and molybdenum species were obtained to determine the potential to be applied for the electrodeposition of molybdenum and nickel oxides. The results showed that a potential below -0.56 V vs SHE must be applied to the cathode to obtain a MoO_2-Ni/Ni_2H deposit, which would need further post-calcination treatment to obtain a stable photo-anode for water splitting applications.

Finally, although this research is mainly focused on the production of MoO_x films by electrodeposition, other alternatives such as spin-coating were also tested to obtain molybdenum oxide films. In fact, good results have been reported in the literature when using this technique to obtain films deposited on substrates such as FTO-coated glass or ITO-coated glass.

An example of the aforementioned is that reported by Chao-Sheng Hsu *et al.* who studied the structural and electrochromic properties of MoO_3 thin films prepared by sol–gel spin-coating technique on ITO-coated glass from precursor solutions of MoO_3 which were prepared by dissolving metallic molybdenum powder in hydrogen peroxide mixed with acetic acid [93]. The results obtained showed the formation of amorphous MoO_3 films which were calcined at a temperature between 100 °C and 500 °C for 1 h, producing nanocrystalline orthorhombic MoO_3 (α-MoO_3) thin films. The electrodes produced by this means were investigated by repetitive cyclic voltammetry (CV) tests in which not only the CV curves but also the optical transmittances showed good reversibility. The 350 °C heat-treated MoO_3 film showed excellent electrochemical reversibility and stability even after 100 CV cycles.

The results obtained by electrodeposition and spin-coating techniques have offered new information, which provides a further insight into molybdenum oxides films properties.

3.5. Project Objectives

Considering the aim of this thesis, previously mentioned in section 1.5, and based in the literature review of this chapter the following specific objectives are proposed:

- Determine the optimal conditions for the fabrication of photo-anodes based on molybdenum oxides films (through electrodeposition and spin-coating methods) on SnO_2:F-coated glass.

- Design and build a laboratory-scale photo-electrochemical cell for the production of hydrogen from the electrolysis of water using the photo-anodes fabricated by electrodeposition.

- Study the kinetics of the photocatalytic evolution of oxygen under darkness, white light and under UV-illumination conditions over the fabricated photo-anodes.

Chapter 4

Experimental Methods and Equipment

This chapter outlines the experimental methodology adopted to obtain the results discussed in this thesis. The procedure to synthesize the nickel/tungsten-doped molybdenum oxide photo-anodes are explained in sections 4.3 and 4.6 of this chapter. The design and manufacture of the photo-electrochemical cell used to test the nickel-doped molybdenum oxide photo-anodes is also described in section 4.2. Analytical instruments and electrochemical techniques used to characterize the photo-anodes produced are described briefly in sections 4.4 and 4.5 and subsections 4.6.2 and 4.6.3.

4.1. Overview of the Experimental Methodology

The PhD research project was organized in two main stages, in accordance with the objectives defined in chapter 3. The first stage was focused on the study of the electrodeposition process of molybdenum oxide films (undoped and nickel-doped) on FTO-coated glass, and the manufacture and performance characterization of a laboratory scale photo-electrochemical cell with molybdenum oxide-based photo-anodes for water splitting. The second stage focused on the study of photo-anodes based on molybdenum oxide films (undoped and tungsten-doped) deposited on FTO-coated glass using the spin-coating technique. The first stage was carried out in the Department of Chemical Engineering, Biotechnology and Materials of the Universidad de Chile, while the second stage was carried out in the Department of Chemical Engineering of the University of Bath, England. The scheme of Figure 4.1 summarizes these stages.

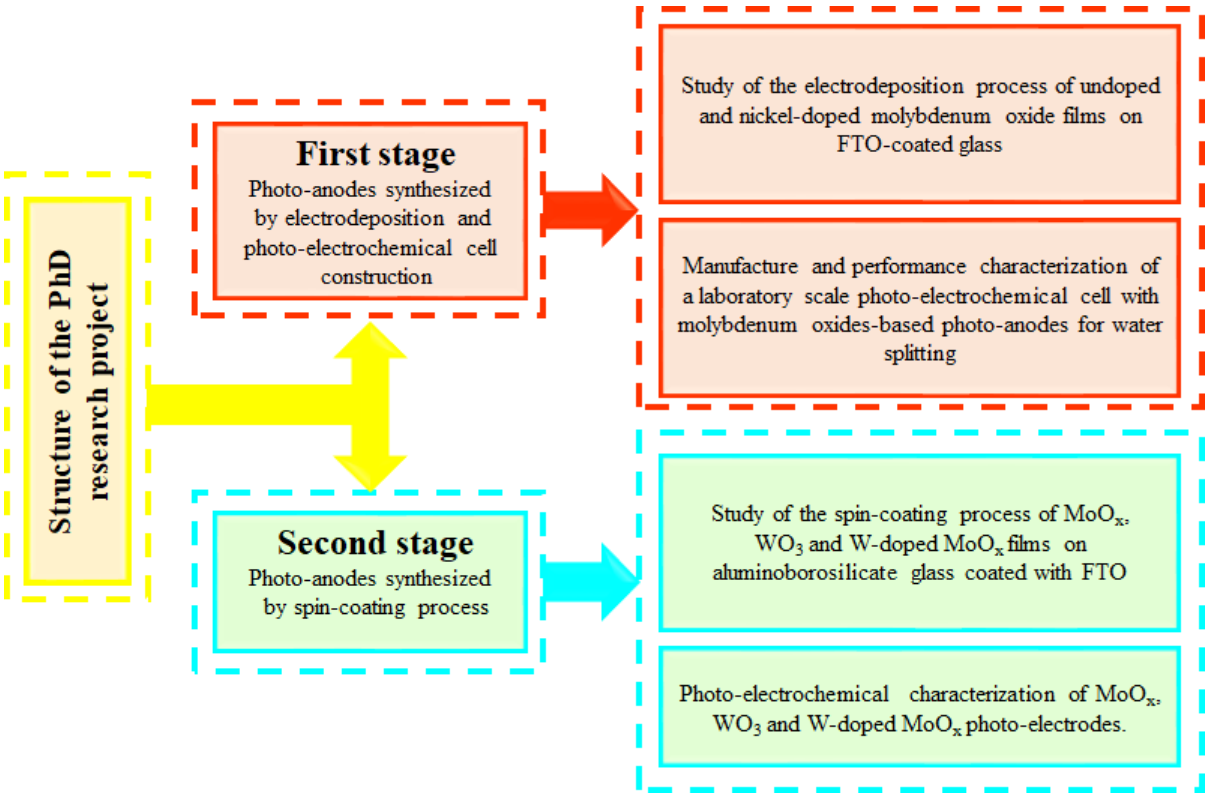

Figure 4.1: Scheme of the work plan. The methodology is organized in two macro-stages, each one represented by a color.

4.2. Photo-Electrochemical Cell Design and Fabrication

The photo-electrochemical properties (catalytic activity for oxygen evolution reaction and long-term stability under light and darkness conditions at room temperature) of the undoped and nickel-doped molybdenum oxide photo-electrodes produced needed to be characterized and analysed. For this purpose, a photo-electrochemical cell made of polytetrafluoroethylene (PTFE) and quartz glass were used.

In the next section materials selection and details on the fabrication of the photo-electrochemical cell are presented.

4.2.1. Cell Body

The material used to construct the cell body needs to be stable in Na_2SO_4 solutions and have low permeability to hydrogen gas. Considering the above, due to its chemical stability and low permeability to hydrogen gas ($4.45 \cdot 10^{-13}$ / mol cm^2 s^{-1} Pa^{-1} [94]), PTFE was chosen as the material for the construction of the cell body.

4.2.2. Optical Window

The optical window is the key component for enabling light illumination of the photo-anode inside the photo-electrochemical cell. The optical window must have high transmission in the UV and visible regions of the electromagnetic spectrum. Materials such as silica or quartz plates have excellent transmission at wavelengths (>300 nm), but quartz plates are cheaper [9]. Therefore, quartz was chosen as the material used for the optical window. The effective area in the quartz window used in the photo-electrochemical cell for sunlight to reach the photo-anode is approximately 11.75 cm^2 (length: 3.97 cm, width: 2.96 cm, thickness: 4 mm). The transmission spectra of quartz window is shown in figure 4.2.

As can be seen in Figure 4.2, the quartz window achieves an approximate transmittance of 91 % which is an excellent value in the region of 300-400 nm (highlighted region in the graph) of the electromagnetic spectrum. The transmittance measurements of the quartz window were carried out in the Chemical Engineering Department of the University of Bath, England. The transmission spectra was collected in a Cary 100 diffuse reflectance UV-Vis spectrophotometer.

4.2.3. Cell Design and Assembly

The photo-electrochemical cell design aimed mainly to reduce the number of joints in order to minimise points of possible liquid and gas leakage, which are quite common problems in modular and stackable cells [95]. In order to make that possible, the chosen design of the photo-electrochemical cell was of the cylindrical type. In the prototype designed a flat face was made where the quartz window is placed. The quartz window was sealed with a rubber separator and a support end plate to prevent leakage. Figure 4.3 and Figure 4.4 shows front and back views of the cell assembly. Besides, in the upper part of the cell a lid with holes that allow the placement of electrodes is used as illustrated in Figure 4.5. Photographs and more details of the dimensions of the fabricated photo-electrochemical cell are shown in Appendix I.

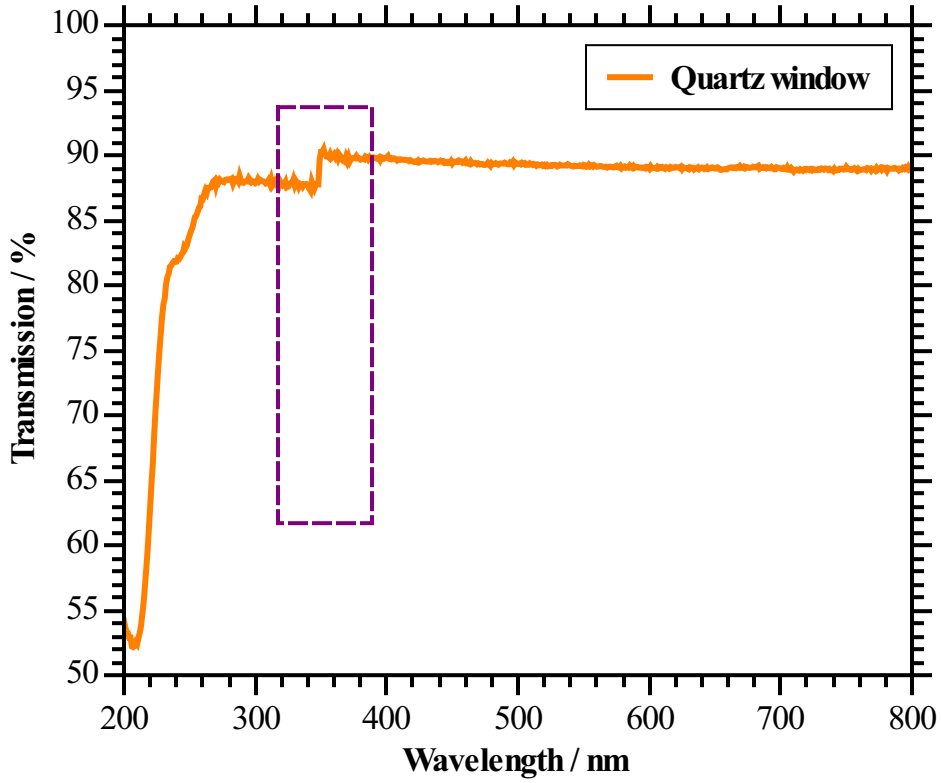

Figure 4.2: Transmission spectrum of quartz window of the photo-electrochemical cell

Finally, Figure 4.6 illustrates the fully assembled photo-electrochemical cell. It is possible to appreciate in this image that the cell has a simple and efficient design, which allows it to have a good performance without liquid and/or gas leakage when it is used in photo-activity measurements of the electrodes fabricated.

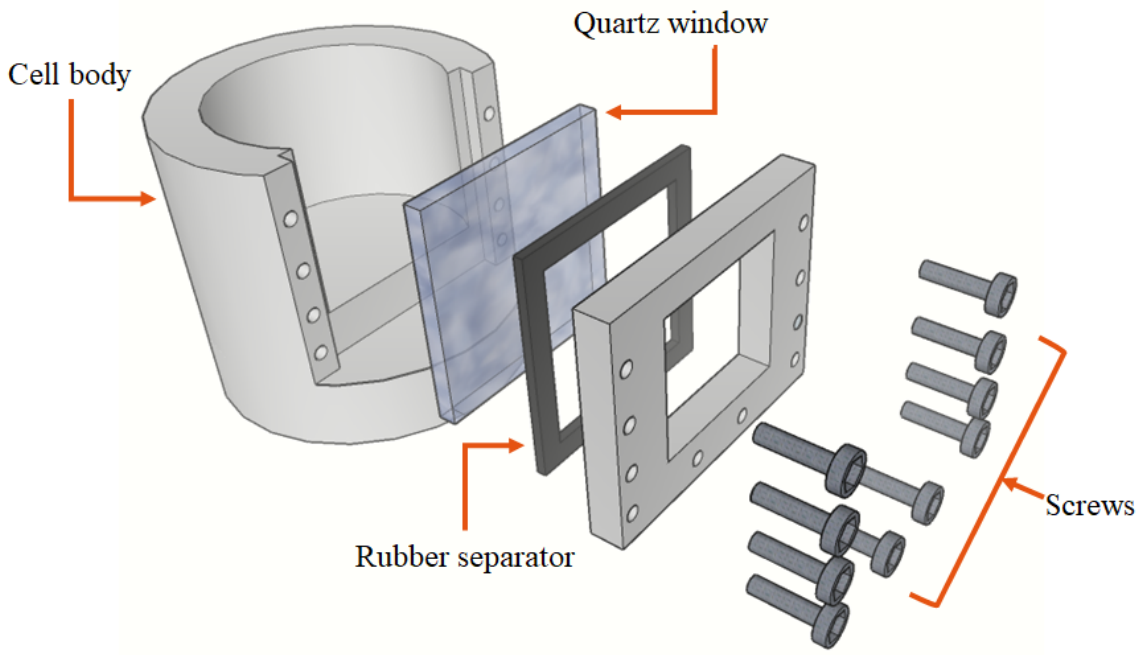

Figure 4.3: Front-view of assembly of the photo-electrochemical cell.

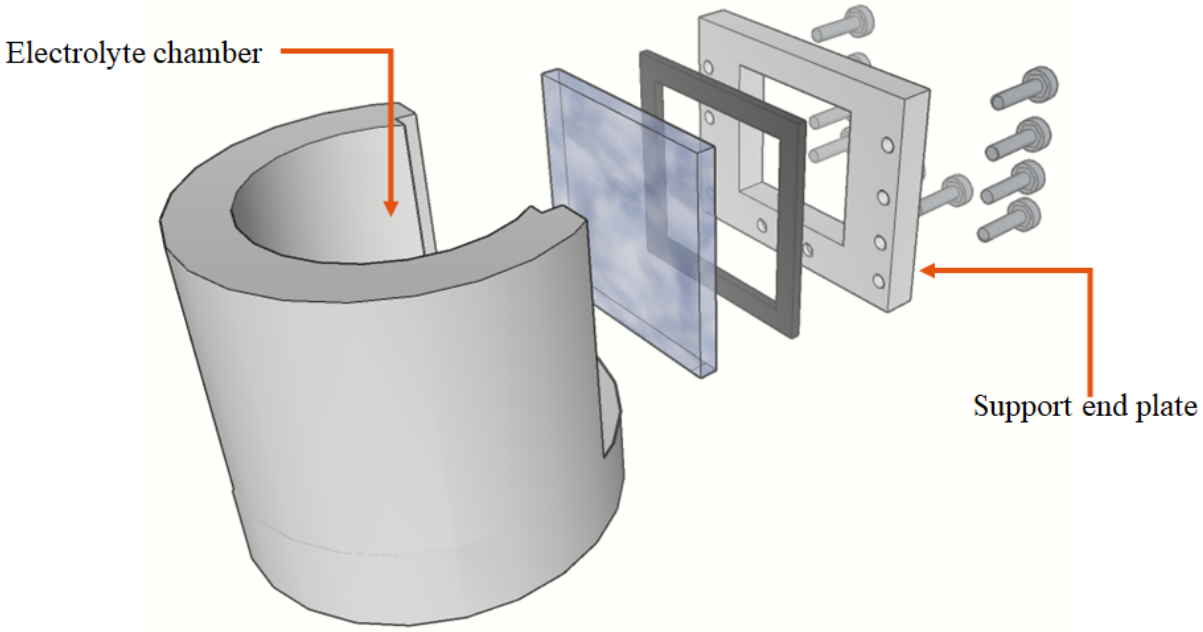

Figure 4.4: Back view of assembly of the photo-electrochemical cell.

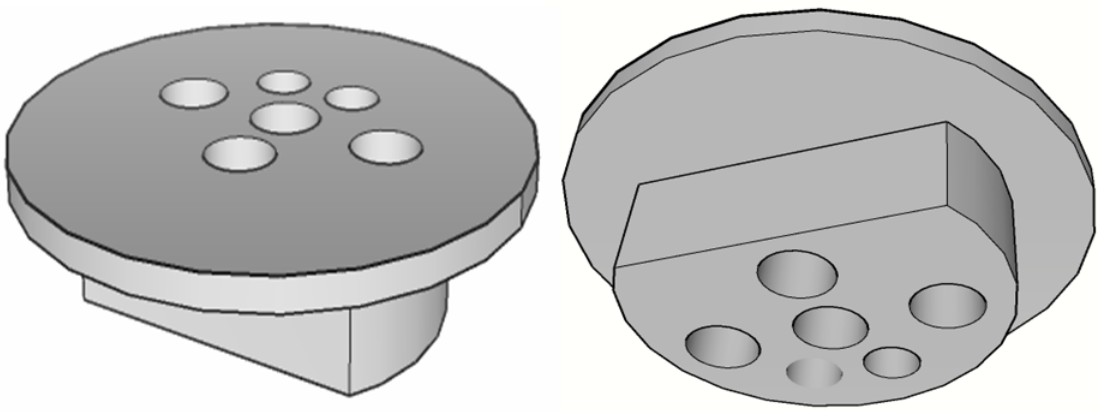

Figure 4.5: Lid of the photo-electrochemical cell.

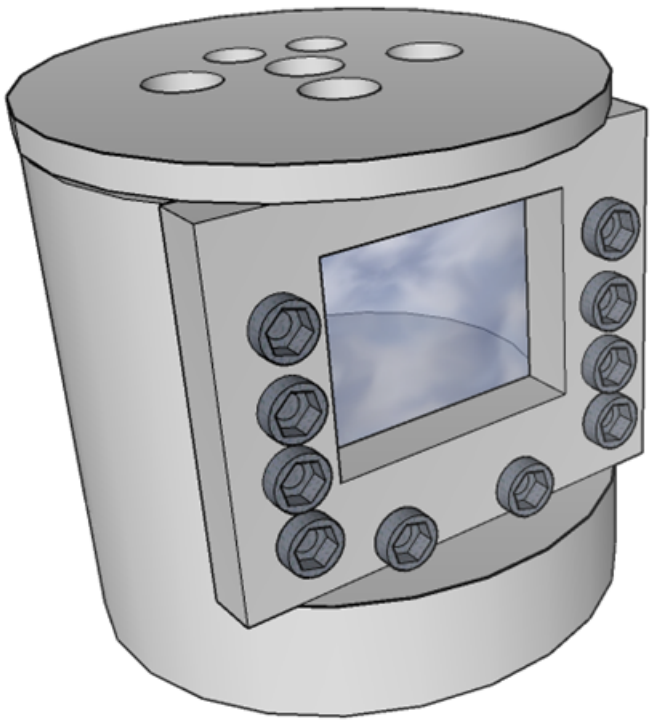

Figure 4.6: Fully assembled photo-electrochemical cell

4.3. Electrodeposition of Undoped and Nickel-Doped Molybdenum Oxide Films

A solution (hereinafter named S_1) containing 0.075 M of molybdenum trioxide (MoO_3, 99.97 % purity, Sigma Aldrich), 0.075 M of nickel ($NiSO_4{\cdot}6H_2O$, 99.00 % purity, Merck), 0.50 M of sodium citrate ($Na_3C_6H_5O_7{\cdot}2H_2O$, 99.00 % purity, Merck) and 0.70 M of ammonium hydroxide (NH_4OH, 25 % NH_3 in H_2O, Merck) was used as electrolyte for the electrodeposition of thin (nanometric) films of molybdenum oxide(s) doped with nickel on FTO-coated glass. Electrodeposition experiments done with a similar electrolyte solution but without nickel (hereinafter named S_2) are also discussed in this research, for comparison of the microstruc-

tural and compositional characteristics and the photo-electrochemical properties of MoO_x and MoO_x-Ni films. All solutions were prepared using deionised (DI) water. The initial pH of the solutions was adjusted to 9.0 using sulfuric acid (97 % purity, Merck), to favour the presence of molybdenum in the form of molybdate ($MoO^{2-}_{4(aq.)}$) and nickel in the form of the dimeric nickel-citrate complex $[Ni_2(OH)_2H_2cit_2]^{4-}_{(aq.)}$ during electrodeposition, as discussed in a previous work on the thermodynamics of the Mo(VI)-Ni(II)-citrate-S(VI)-N(III) aqueous system [24].

FTO-coated glass slides (TEC 8, 3.0 mm thickness, Sigma-Aldrich) were cut into pieces of 1.0 cm width and 2.5 cm length to be used as working electrodes. Copper foil and silver paste were used to fabricate the electrical connections of the FTO-coated glass pieces. The electrodeposition active area of the FTO-coated glass electrodes was a rectangle of 1 cm width and 1.5 cm length (see Figure 4.7). A platinum foil (1.25 cm^2) was used as counter electrode and an Ag/AgCl(3 M KCl) electrode as reference. The three electrodes were mounted in a glass-jacketed cell and temperature was controlled at 25 °C. A cathodic potential of -1.377 V vs Ag/AgCl (3M) was applied for 3 hours to the working electrode (using a Gamry Reference 3000 potentiostat/galvanostat/ZRA) to promote electrodeposition of molybdenum oxide(s) and nickel metal/hydride, considering that the reduction of molybdate ions occurs solely at high overpotentials [24].

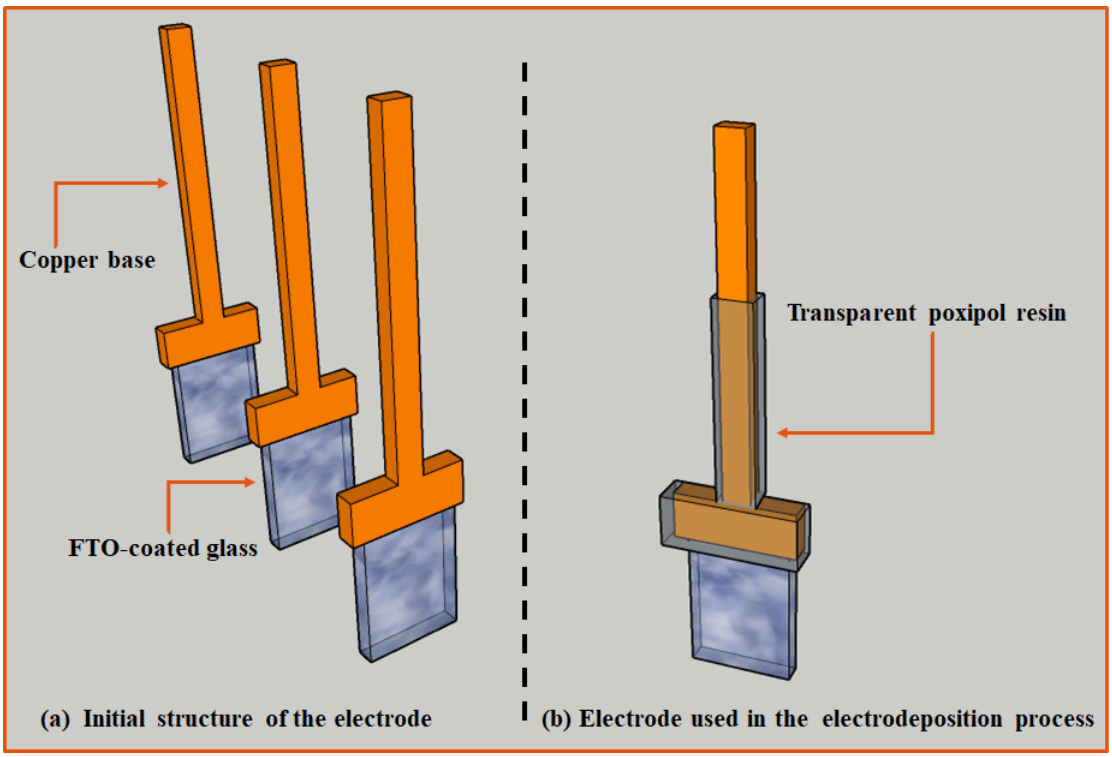

Figure 4.7: Diagram of the photo-anode: (a) initial structure of the photo-electrode, (b) photo-anode to be used in the cell.

4.4. Characterization of Undoped and Nickel-Doped Molybdenum Oxide Films

The microstructure, chemical composition and UV-visible light absorbance of the deposits obtained were characterized by scanning electron microscopy (SEM), energy-dispersive X-ray spectroscopy (EDS), X-ray photoelectron spectroscopy (XPS), atomic force microscope (AFM) and UV-visible spectroscopy.

A JEOL JSM-IT300 SEM coupled to an Oxford Instruments x-act Penta EDS device was used to perform the microstructural and elemental analysis, with a penetration depth of 2 μm at different magnifications.

A Physical Electronics 1257 XPS system was used in order to corroborate the elemental composition of the films and the oxidation states of the present elements. Its surface analysis chamber is equipped with radiation (non-monochromatic) at 1.4866 kV from an aluminium Kα source. The electrons are captured at 35° to the normal's sample. Spectra were acquired in the region of interest using the 0 to 1200 eV experimental range of binding energy, areas where it is expected to find signals of the elements: Mo, Ni, O, Sn, F and C.

The surface morphology and thickness of the films were examined using an atomic force microscope model NaioAFM (Nanosurf GmbH, Langen, Germany). The measurements were performed in the contact mode and with a maximum scan field area of 50 x 50 microns.

Finally, the UV-visible light absorbances (in the range between 300 and 800 nm) of the films produced were recorded using an Agilent 8553 UV-visible spectrometer with a tungsten lamp. The absorption coefficient and band gap of the films produced were determined by fitting the data of the UV-visible spectra obtained using Tauc plots.

4.5. Photo-electrochemical Measurements of the Oxygen Evolution Reaction using Electrodes Undoped and Nickel-Doped Molybdenum Oxide Films

The performance of the undoped and nickel-doped molybdenum oxide photo-electrodes was tested in the cell described the section 4.2. Photo-electrochemical measurements were performed using white (Chanson, 30 W, 6000-6500 K color temperature) and UV (Chanson, 20 W, $\lambda_{max} = 385$ nm) LED lights coupled to a power source with adjustable voltage/current output, and a Gamry Reference 3000 potentiostat/galvanostat/ZRA.

The photo-electrodes produced by electrodeposition of MoO_x-Ni films (or MoO_x) on FTO-coated glass were used as working electrodes, after cleaning with acetone and distilled water in an ultrasonic bath for 5 minutes and drying in air. A platinum foil (1.25 cm^2) was used as counter electrode and an Ag/AgCl(3 M KCl) electrode was used as reference. A solution of 0.1 M sodium sulfate (Na_2SO_4, 99.00 % purity, Sigma Aldrich) and pH equal to 3.5 adjusted using sulfuric acid (H_2SO_4, 98 % purity, Merck) was used as electrolyte.

These three electrodes were mounted in the PTFE cell, one of them, with the photo-

electrode placed in front of the quartz crystal window of the cell. In this setup, the light strikes perpendicularly to both the quartz glass window and the photo-electrode surface placed at 4 cm distance from the light source, with the MoO_x-Ni (MoO_x) film facing the light. The white light intensity was regulated to reproduce the illuminance level of a full daylight (10 klux), assuming neglectable reflection losses. A digital light lux-meter (Outest, GM1010) was used for this purpose. Likewise, the UV light intensity was regulated using a digital radiometer (Tenmars, TM-213) to provide an irradiance of 2 mW cm^{-2} at a distance of 4 cm from the light source.

Open circuit potential (OCP) measurements were performed for 45 minutes under dark, UV and white light to determine the type of semiconductor of the electrodeposited films. Linear voltammetries under dark, UV and white lights at scan rate of 25 mV s^{-1} and between 0 and 1.6 V vs Ag/AgCl (3M KCl) were carried out to study the photo-activity of the electrodes. Finally, current transients were carried out for 30 minutes under dark, UV and white light to study the stability (photo-corrosion) of the deposits obtained.

4.6. Photo-Anodes Synthesized by Spin-Coating

Looking for alternatives, spin-coating technique has been considered for the synthesis of photo-anodes to be studied in this research due to advantages described in section 2.4 of chapter 2.

The following subsections describe the synthesis of the photos-anodes by the spin-coating method and their photo-activity characterization in Dr. Eslava's Research Group at the University of Bath.

4.6.1. Deposition of MoO_x, WO_3 and W-doped MoO_x Films

WO_3-doped MoO_x and pure MoO_x and WO_3 films on Aluminoborosilicate glass (ABS) coated with fluorine-doped tin oxide (FTO) were prepared using a spin-coating system (SCK-200 Spin Coater, INTRAS). The solutions employed for the spin-coating deposition were prepared under environmental conditions. The precursor solution for tungsten-doped molybdenum oxide photo-anodes (electrodes S_5 and S_6)was prepared by dissolving 1.75 g of ammonium molybdate (para) tetrahydrate ($H_{24}Mo_7N_6O_{24} \bullet 4H_2O$, 81-83 % as MoO_3, Alfa Aesar) and 0.8 g of tungstic acid (H_2WO_4, 99 % purity, Sigma Aldrich) in 6 mL of ethylene glycol ($C_2H_6O_2$, 99.99 % purity, Sigma Aldrich). The precursor solution for the preparation of pure MoO_x films (eletrode S_3), was prepared dissolving 1.75 g of ammonium molybdate (para) tetrahydrate in 6 mL of ethylene glycol. Finally, the precursor solution of WO_3 film (eletrode S_4), was prepared by dissolving 0.8 g of tungstic acid in 6 mL of ethylene glycol. All the solutions were prepared using deionised (DI) water, stirred for 3 hours and subsequently sonicated for 1 hour.

Aluminoborosilicate glass (ABS) coated with fluorine-doped tin oxide (FTO) transparent conductive layer (R_s= 8 Ω sq $^{-1}$) was provided by Solaronix, CH. These FTO-ABS glass slides were cut into pieces of 1.2 cm width and 2.5 cm length and were cleaned ultrasonically in a 2 % aqueous Hellmanex III (industrial detergent) solution followed by ultrasonic baths in deionized water, acetone and isopropyl alcohol for minutes each. Finally, the substrates were

rinsed with deionized water and dried with compressed air to be used as working electrodes. The solutions prepared as stated in the previous paragraph were cast by spin-coating onto the FTO-ABS glass pieces using 4000 rpm for 40 s and dried to remove solvents. The coated glass samples were calcined at 470 °C for 120 minutes using a ramp rate of 10 °C min^{-1}. In the case of the samples prepared using the S_3 precursor solution, these had two synthesis protocols: the first form of preparation of the photos-electrodes using this solution is by the protocol described above, while the second type of electrodes obtained with this solution were prepared by repeating the described method 3 times in order to obtain thicker films. Figure 4.8 illustrates the preparation of photo-electrodes by the spin-coating process in this research.

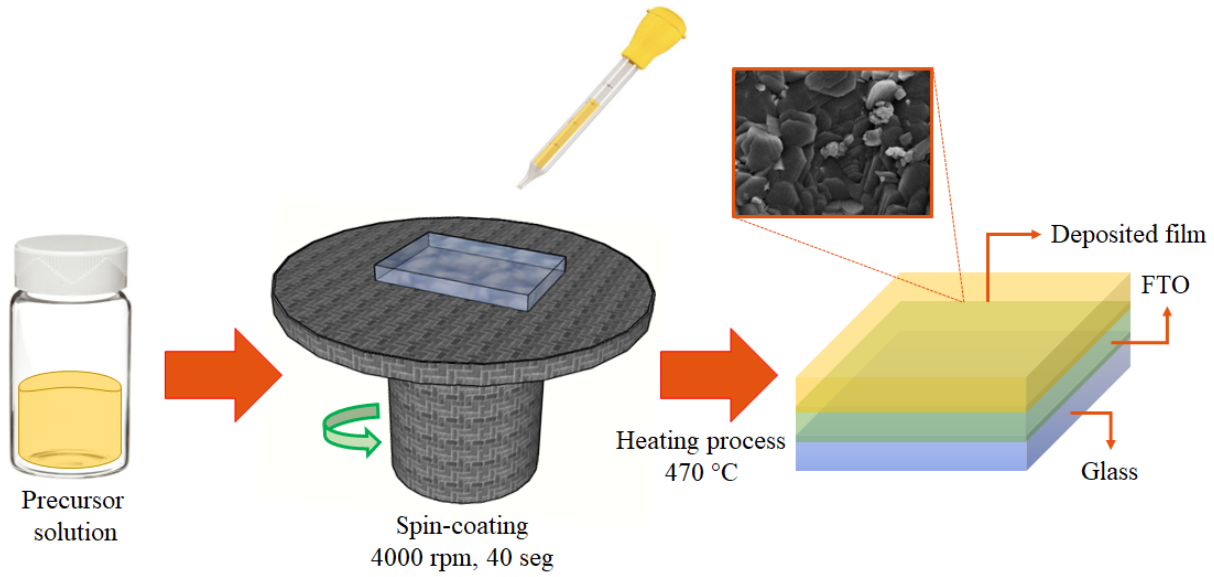

Figure 4.8: Schematic diagram of the synthesis of photo-anodes by spin-coating process.

4.6.2. Characterization of MoO_x, WO_3 and W-doped MoO_x Films

The microstructure, chemical composition and band-gaps of the deposits obtained were characterized by scanning electron microscopy (SEM), X-Ray diffraction (XRD) and UV-visible spectroscopy.

Field emission scanning electron microscopy images (FE-SEM) were acquired using a JEOL FESEM6301F.

X-Ray diffraction (XRD) patterns were collected in the 2 Theta range 10-80° with a Bruker AXS D8 Advance using Cu-Kα (λ= 0.154 nm) radiation with a total integration time of 960 s.

The necessary information for the construction of Tauc plots was collected in a Cary 100 diffuse reflectance UV-Vis spectrophotometer.

4.6.3. Photo-electrochemical Characterization of MoO_x, WO_3 and W-doped MoO_x Photo-Anodes

The photo-electrochemical performance of photo-anodes under AM 1.5G illumination (100 $mWcm^{-2}$) from a filtered 300W Xenon lamp source was evaluated using a CompactStat potentiostat (Ivium Technologies). PEC cells consisted of three electrodes, with Pt as the counter electrode, Ag/AgCl/3.5 M KCl as the reference electrode and the fabricated photo-anodes as the working electrodes. All experiments were carried out in a 0.2 M Na_2SO_4 (99 % purity, Sigma Aldrich) electrolyte solution (pH = 6.73 adjusted with sulfuric acid). Illumination was directed towards the back of the FTO-ABS working electrode and a mask was placed on top of the photoelectrode to regulate the illuminated area. Photocurrent-time curves were performed at an applied bias potential of 1.23 V vs the reversible hydrogen electrode (V vs RHE), which corresponds to the minimum potential that has to be applied between the electrodes (anode and cathode) of an electrochemical cell to promote the water splitting reaction. Photocurrent-potential curves were recorded at a scan rate of 20 mV s^{-1}. The potentials measured against the reference electrode were converted to the standard hydrogen electrode (SHE) scale using the Nernst equation:

$$E^{\circ}_{RHE} = E^{\circ}_{Ag/AgCl} + E_{Ag/AgCl} + 0{,}059pH \tag{4.1}$$

where $E^{\circ}_{Ag/AgCl}$ is 0.205 V vs SHE at 25 °C and $E_{Ag/AgCl}$ corresponds to measured potential.

The theoretical fundamentals of the electrochemical, micro structural, compositional and optical analysis used in the study and characterization of photo-anodes synthesized are presented in the appendices B, C and D.

Chapter 5

Synthesis and Characterization of Undoped and Nickel-Doped Molybdenum Oxide Photo-Anodes

This chapter presents the synthesis and characterization of undoped and nickel-doped molybdenum oxide photo-anodes films. The results studied include: (1) Eh-Ph diagrams developed by Morales in order to determine by a thermodynamic analysis the electrodeposited species on the substrate of each fabricated electrode; (2) microstructure analysis of the films performed by Scanning Electron Microscopy (SEM) and Atomic Force Microscopy (AFM); (3) the composition and chemical state of the elements forming the films obtained by X-Ray Photoelectron Spectroscopy (XPS) and Energy-dispersive X-ray Spectroscopy (EDS or EDX); (5) the study of photoactivity and conductivity type presented by the films performed by Open Circuit Potential (OCP) tests and (6) finally, representative linear sweep voltammograms of the electrodes obtained in an electrolyte of 0.1 M Na_2SO_4 at pH 3.5 in order to obtain a better understanding of the phenomena in the system in which the photo-electrochemical experiments were carried out.

5.1. Electrodeposition Process: Synthesis of Undoped and Nickel-Doped Molybdenum Oxide Photo-Anodes

The electrodeposition experiments (cronoamperometries) were carried out according to the protocol described in 4.3. Figure 5.1 shows curves of current densities versus time obtained at a potential of -1.377 V vs Ag/AgCL (3M) applied for 3 hours for the synthesis of undoped and nickel-doped molybdenum oxide electrodes.

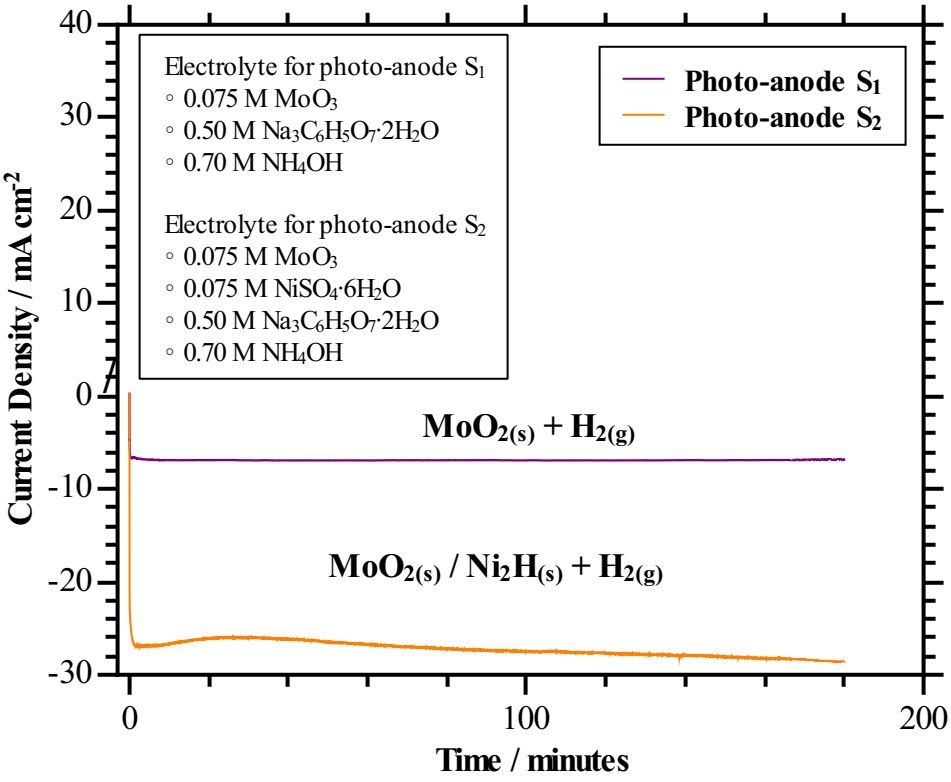

Figure 5.1: Current density-time curves obtained at a potential of -1.377 V applied for 3 hours. Photo-anode S_1: Undoped molybdenum oxide electrode; Photo-anode S_2:Nickel-doped molybdenum oxide electrode.

In order to obtain a better understanding of the phenomena in the system in which the electrodeposition experiments were carried out, Eh-pH diagrams for the molybdenum and nickel species have been elaborated by Morales *et al* [24] . Figure 5.2 shows the diagrams obtained which will be used to interpret and describe the processes that occur during the chronoamperometries illustrated in Figure 5.1.

The general data illustrated in Figure 5.1 show that the formation of nickel-doped molybdenum oxide films on FTO-coated glass (photo-anode S_2), present a larger cathodic current density curve than the cathodic current density curve obtained for the synthesis of undoped molybdenum oxide films (photo-anode S_1) in the same experimental conditions[7].

[7] Chronoamperometries for the synthesis of photo-anodes were carried out during 180 minutes at a potential of -1.377 V using an electrolyte at pH 9 and at a temperature of 25°C. More details in section 4.3.

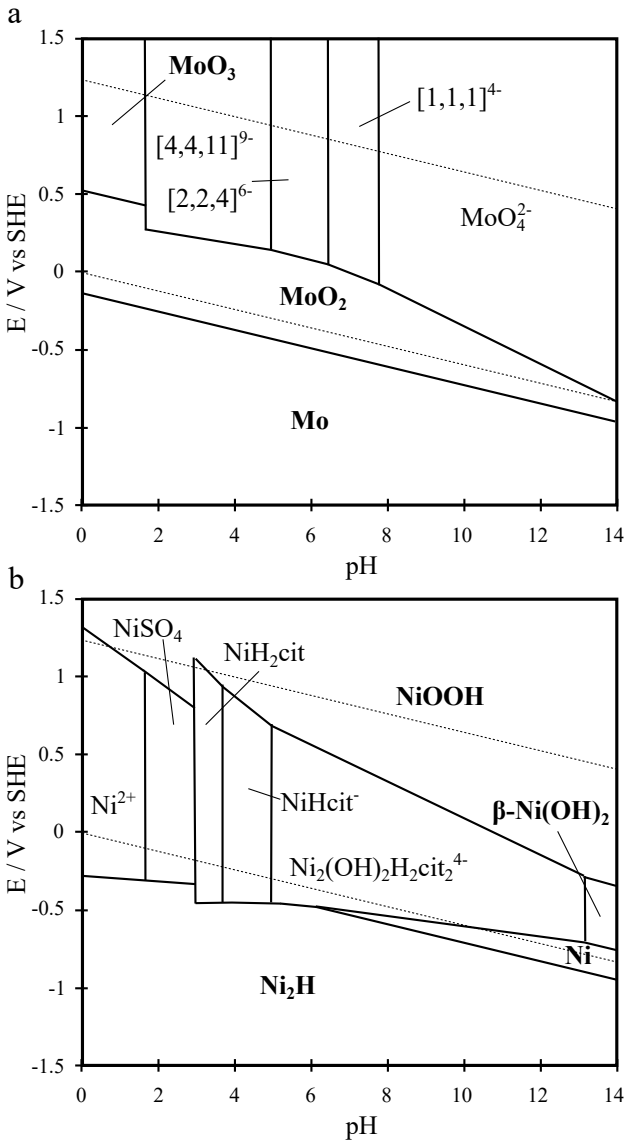

Figure 5.2: Eh-pH diagrams for (a) molybdenum[9]and (b) nickel species at 298 K and 10^5 Pa. Activity of molybdenum and nickel species equal to 10^{-2} and activity of citrate, ammonia and sulfate species equal to 10^{-1}. Solid species are showed in bold letter [24].

A zoom at the beginning of the current density curve of the electrode S_1 (Figure 5.3) shows a small decrease in the cathodic current density (<2 min). Although the electrodeposition process was carried out at pH 9 and at a potential of -1.377 V ($\sim$ -1.172 vs SHE), hypothetically favoring the formation of molybdenum in metallic state, as shown in diagram 5.2.(a), it is possible to assume that this form of the current density at the initial instants of the experiment is related to the formation of molybdenum oxides of the type MoO_2, which are probably partially blocking the surface of the electrode. The above would be caused because the high electronegativity of oxygen compared to hydrogen at room temperature (even in environments where there is a greater amount of hydrogen) would give greater stability to binary d-metal oxides, such as MoO_2 instead of metal forms with lower states of oxidation

[9]The notation for molybdenum-citrate complexes is taken from the work of Cruywagen, Rohwer and Wessels [97] [p,q,r] stands for the product of the reaction: $pMoO^{2-}_{4(aq.)} + qHcit^{3-}_{(aq.)} + rH^{-}_{(aq.)} \leftrightarrow [p,q,r]^{[2p+3q-r]-}_{(aq.)}$.

[96]. Studies carried out by Shembel e*t al.* [88] confirm that at potentials lower than -0.68 V vs SHE the most stable species due to the reduction of molybdate ions, MoO_4^{2-} is molybdenum dioxide, MoO_2. This justifies the formation of molybdenum oxides instead of metallic molybdenum, even in the presence of hydrogen generated during HER.

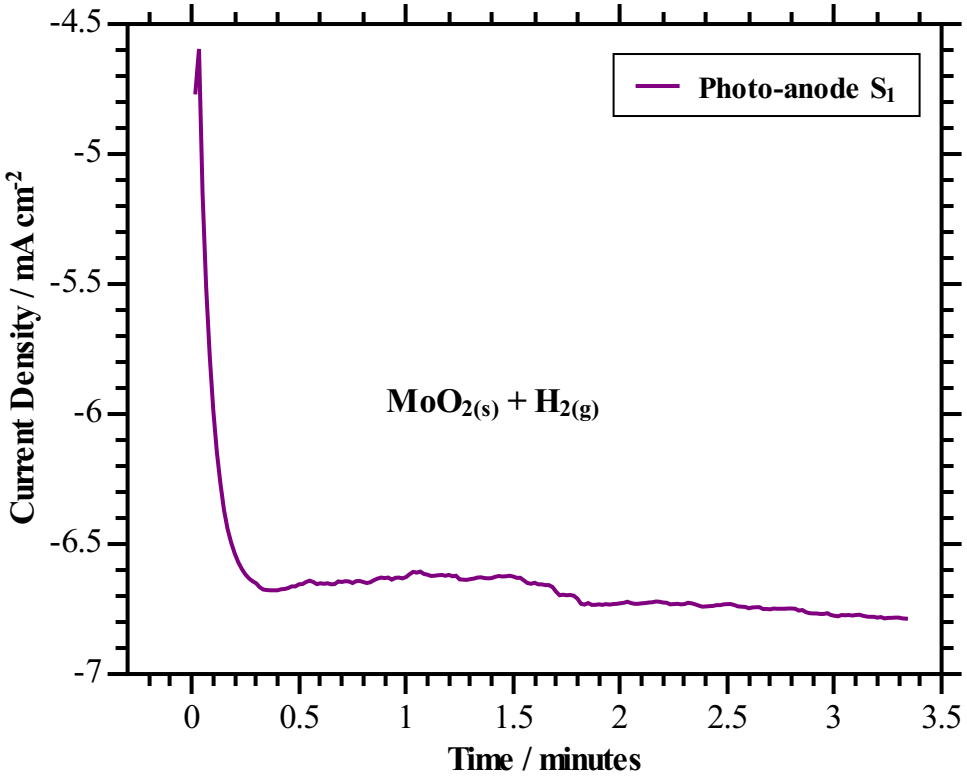

Figure 5.3: First 3.4 minutes of the current density-time curves obtained at a potential of -1.377 V vs Ag / AgCl (3M) and 3 hours during the synthesis of the photo-electrode S_1.

Despite of the current density curve obtained throughout the experiment would be a product of both the hydrogen evolution reaction and the reduction of molybdate ions to molybdenum dioxide, the steady-state value of the current density illustrated in Figure 5.1 would correspond mainly to the HER as reported by Kuznetsov e*t alt.* [90][91][92]. Probably the high electrical conductivity[10] of the MoO_2 deposited on FTO-coated glass would have a positive impact on the hydrogen evolution reaction, since it would allow the passage of electrons easily from the substrate to the electrode | electrolyte interface promoting HER at the cathode surface.

Considering the above, the possible reactions that describe the reduction of molybdate ions to molybdenum oxide and the evolution of hydrogen during electrodeposition are the following:

$$4H_2O_{(l)} + 4e^- \rightarrow 2H_{2(g)} + 4OH^-_{(aq.)} \tag{5.1}$$

[10] MoO_2 electrical conductivity: 10^4 S cm^{-1} [98].

$$MoO^{2-}_{4(aq.)} + 2H_2O_{(l)} + 2\mathrm{e}^- \rightarrow MoO_{2(s)} + 4OH^-_{(aq.)} \tag{5.2}$$

With regard to electrode S_2, clearly the cathodic current density had a more negative magnitude during the whole experiment as can be seen in Figure 5.1. During the first 70 minutes the curve presented a concave shape, this behavior could be due to two main factors:

- Initial formation of the complex $[\mathrm{NicitMoO_2}]_{ads}$ [92].
- Formation of the alloy $\mathrm{MoO_{2(s)}}$-$\mathrm{Ni_2H_{(s)}}$ from $[\mathrm{NicitMoO_2}]_{ads}$.

The initial current density curve shape could be related to the partial blockage of the electrode surface by an intermediate complex of the type $[\mathrm{NicitMoO_2}]_{ads}$ which would be formed under alkaline conditions at the working potential, as reported by Kuznetsov *et al* [92]. The possible formation of the intermediate complex mentioned above would be given by the following equation [92]:

$$MoO^{2-}_{4(aq.)} + Nicit_{(aq.)} + 2H_2O_{(l)} + 2\mathrm{e}^- \rightarrow [NicitMoO_2]_{\mathrm{ads}} + 4OH^- \tag{5.3}$$

Afterwards, the complex $[\mathrm{NicitMoO_2}]_{ads}$ gives rise to the formation of $[\mathrm{Ni_2(OH)_2H_2cit_2}]^{4-}_{(aq.)}$ and $\mathrm{MoO_{2(s)}}$ as shown in equation 5.4. It is possible to assume that due to the complexing ability of the citrate, the adsorbed species would slowly give way to the $\mathrm{MoO_{2(s)}}$-$\mathrm{Ni_2H_{(s)}}$ alloy formation within the first 70 minutes as illustrated in Figure 5.1 (equations 5.4 and 5.5).

$$[NicitMoO_2]_{\mathrm{ads}} + H_2O_{(l)} + 2\mathrm{e}^- \rightarrow MoO_{2(s)} + \frac{1}{2}[\mathrm{Ni_2}(OH)_2H_2cit_2]^{4-}_{(aq.)} \tag{5.4}$$

The complex, $[\mathrm{Ni_2(OH)_2H_2cit_2}]^{4-}_{(aq.)}$, which is the most stable form of the nickel at pH 9 [24] it would form $\mathrm{Ni_2H_{(s)}}$ as indicated in the equation 5.5. This agrees with diagram 5.2(b), which would indicate that at the electrodeposition experimental conditions, $\mathrm{Ni_2H_{(s)}}$ would be formed from the species adsorbed.

$$[\mathrm{Ni_2}(OH)_2H_2cit_2]^{4-}_{(aq.)} + H_2O_{(l)} + 5\mathrm{e}^- \rightarrow \mathrm{Ni_2}H_{(s)} + 3OH^-_{(aq.)} + 2Hcit^{3-}_{(aq.)} \tag{5.5}$$

In the next 110 minutes, the current density value continued to increase reaching approximately -29 mA $\mathrm{cm^{-2}}$ at 180 minutes. This current density had a more cathodic value than that presented by electrode S_1 during the same period. This behavior would be linked to the cathodic surface type. Chassaing [99] has reported that the nickel-molybdenum alloys are a good catalyst for the HER under similar experimental conditions (pH 9.5 and polarization range: from - 1.3 to -1.6V vs SSE) to those used in chronoamperometries made in this research. The above would explain the cathode current density increase in the last 110 minutes. This suggests that the $\mathrm{MoO_{2(s)}}$-$\mathrm{Ni_2H_{(s)}}$ alloy exhibits better electrical conductivity than the undoped molybdenum dioxide deposited on FTO-coated glass, promoting the hydrogen evolution reaction at the cathodic surface easily as shown in Figure 5.1.

5.2. Microstructural Analysis of the Undoped and Nickel-Doped Molybdenum Oxide Photo-Anodes

In order to characterize the morphology of the undoped and nickel-doped molybdenum oxide films deposited on FTO-coated glass, the electrodes S_1 and S_2 were analyzed by Scanning Electron Microscopy (SEM) and Atomic Force Microscopy (AFM).

The surface morphology of the undoped and nickel-doped molybdenum oxide photo-anodes was observed through SEM and the micrographs are presented in Figure 5.4. According to this figure, SEM analysis revealed the presence of several cracks on the surface of the photo-electrodes S_1 and S_2. The loss of water from the deposited films on FTO-coated glass and the hydrogen evolution reaction during the electrodeposition process are probably the main causes of the formation of cracks in these electrodes.

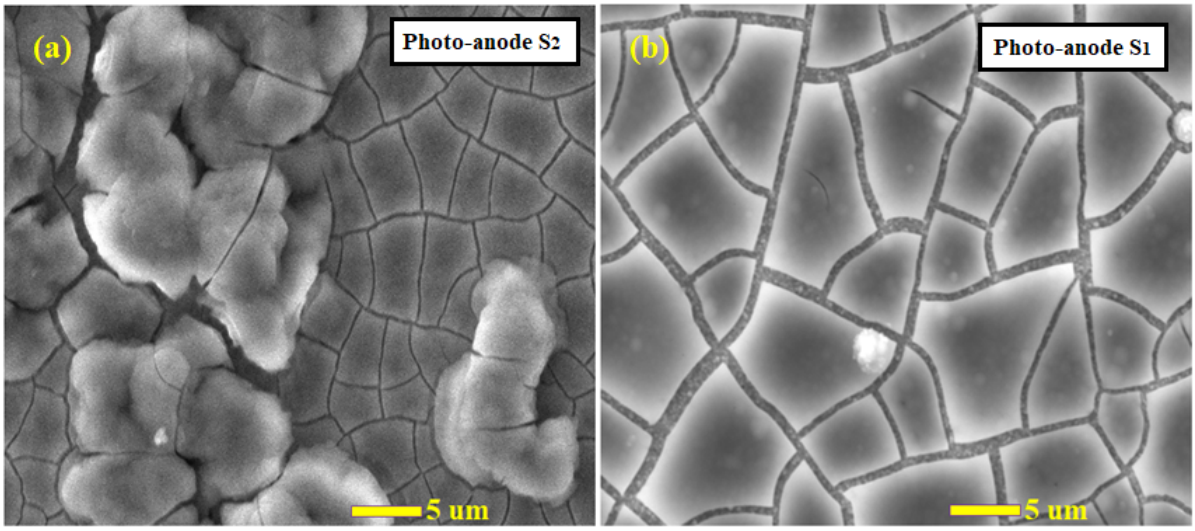

Figure 5.4: SEM micrographs of the deposits obtained by applying -1.377 V vs Ag/AgCl (3 M KCl): (a) Photo-anode S_2, (b) Photo-anode S_1. Magnification: 3,000x

Figure 5.4(a), shows a nickel-doped molybdenum oxide film on FTO-coated glass. This figure allows to appreciate a film of heterogeneous (this point will be discussed in detail in the AFM analysis section) and irregular morphology with conglomerates distributed on top of the sustrate. These islands have an irregular shape (raspberry structures) that promote large surface areas in the photo-anodes produced, which in turn must result in better light exposure and more active sites for the PEC oxygen evolution reaction.

An SEM image of an undoped molybdenum oxide film on top of FTO-coated glass is shown in Figure 5.4(b). Unlike the nickel-doped molybdenum oxide films, it does not show the presence of irregularly shaped conglomerates. Indeed, it forms an orderly and homogeneous pattern over the entire surface of the photo-anode S_1. This comparison reveals the advantage of the $MoO_{2(s)}$-$Ni_2H_{(s)}$ alloy in the electrode S_2, since the conglomerates of irregular shape in this type of film would favor the PEC oxygen evolution reaction, due to the greater surface area and availability of active sites on it.

An AFM image of a nickel-doped molybdenum oxide film is shown in Figure 5.5. According

to this figure, $MoO_{2(s)}$-$Ni_2H_{(s)}$ films exhibit an irregular surface morphology. Conglomerates and randomly located clusters are clearly observed on the film surface, which agrees with Figure 5.4(a) obtained by SEM analysis. A surface examination revealed that this hill-like structures have an average width of 182 nm. The height of these conglomerates varied from 250 to 1,159 nm. Moreover, Figure 5.5(a) shows that the film surface does not follow the pattern of the FTO-coated glass. In contrast to this, Figure 5.5(b) corroborates that the photo-anode S_1 presents a film deposited without the presence of irregularly shaped conglomerates as illustrated above in Figure 5.4(b). The AFM image of the undoped molybdenum oxide film presented in Figure 5.5(b), indicates the presence of a homogeneous film on the FTO-coated glass surface.

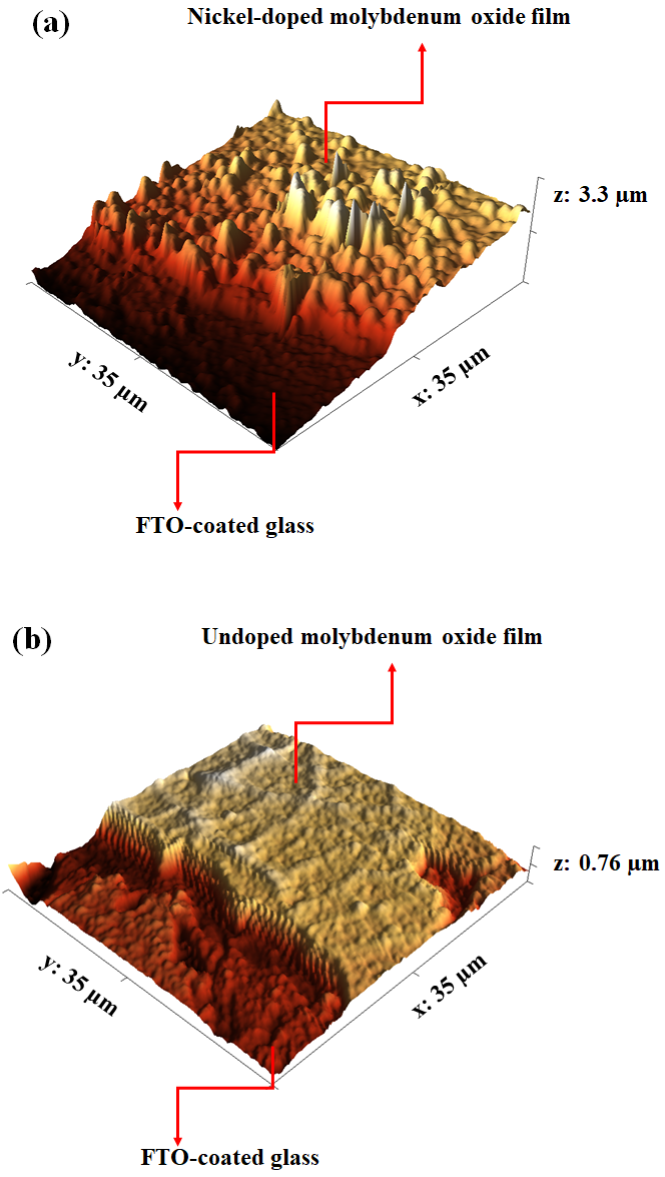

Figure 5.5: AFM image of the photo-anodes S_2 (a) and S_1 (b) surface: 3D topography.

To determine the thickness of the deposits, the step formed between the clean FTO-coated glass surface and the deposit was considered. The above is illustrated in Figure 5.6.

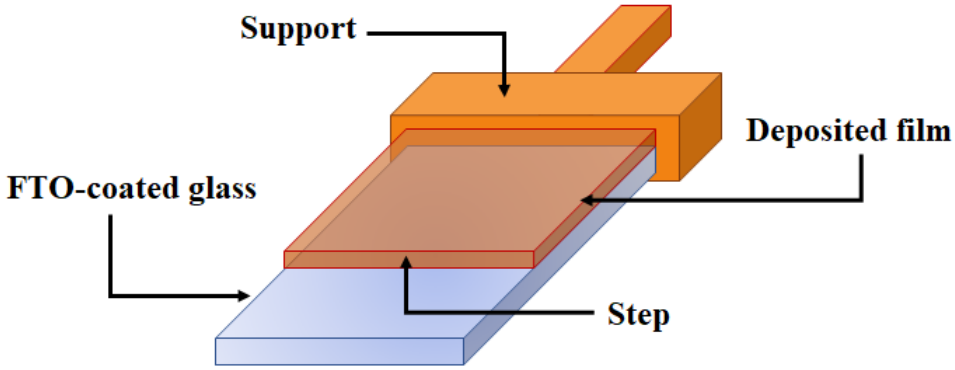

Figure 5.6: Step on the deposited film in the electrode S_2.

Previously, thicknesses ranging between ca. 219 nm [81] and 1150 nm [21] have been reported for molybdenum oxide films obtained by electrodeposition. In this research the thicknesses determined by AFM showed that the photo-anode S_2 presents a film [11] on the substrate with an average thickness of 763 nm, while the electrode S_1 has a deposited film with an average thickness of 438 nm on FTO-coated glass, which is thinner than the film obtained on the substrate of the electrode S_2. Both values are within the ranges reported in the literature [81] [21]. For the photo-anode S_2 it is possible to assume that the nickel presence could modify the morphology and the thickness of the generated films. Indeed, Bozena Losiewicz [100] has reported that the nickel-based coatings are among the most often used in order to obtain electrodes with very developed, rough, thick or porous electrode surface. This is due to the easiness with which Ni^{2+} penetrates within of interstitial spaces and besides the reaction of Ni with the basal (molybdenum) or lateral (oxygen) atoms of the metal oxide strucutre, modifying the morphology and properties of the semiconductor material [101].

5.3. Compositional Analysis of the Undoped and Nickel-Doped Molybdenum Oxide Photo-Anodes

The composition and chemical state of the elements forming the films were characterized by Energy-dispersive X-ray Spectroscopy (EDS or EDX) and X-Ray Photoelectron Spectroscopy (XPS).

Figures 5.7 and 5.8 show the EDS analyses for selected points (same micro-area used in the SEM analysis presented in Figure 5.4) of the photo-anodes S_1 and S_2.

EDS spectra of the electrodes S_1 and S_2 corroborate a strong presence of molybdenum (over 40 wt.% in both cases) in all the deposited films, which would be in the photo-anodes mainly as MoO_2 (as suggested in Section 5.1 and by the XPS analysis) and MoO_3 (formed from the partial oxidation of MoO_2 in contact with the atmosphere).

The presence of oxygen at the electrodes is also shown in the EDS spectra. The high

[11] The conglomerates present on the deposited film surface were not considered in the thickness measurements. More details in appendix H

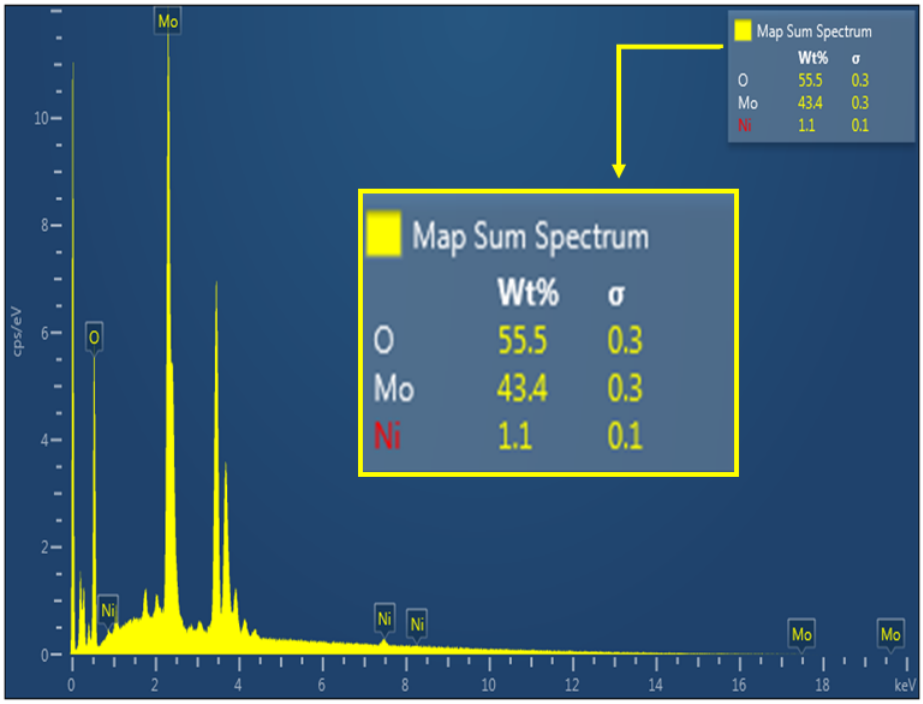

Figure 5.7: EDS spectrum of the deposits obtained by applying -1.377 V vs Ag/AgCl. Photoanode S_2.

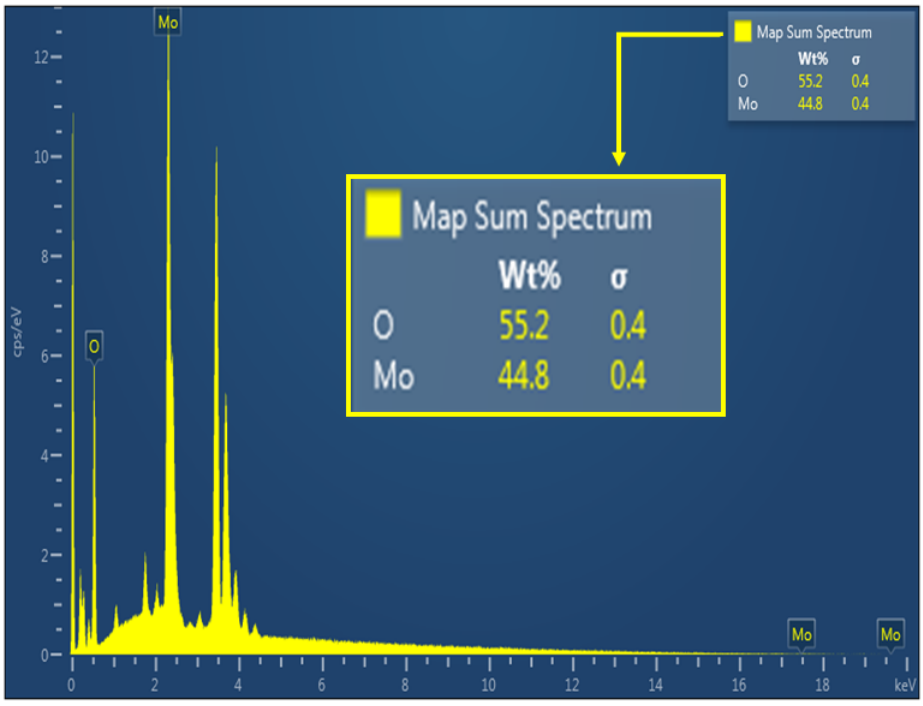

Figure 5.8: EDS spectrum of the deposits obtained by applying -1.377 V vs Ag/AgCl. Photoanode S_1.

amount of oxygen (over 55 wt. % in both cases) corroborates the presence of MoO_2/MoO_3.

For the case of the photo-anode S_2, as can be seen in Figure 5.7, it is possible to find nickel on the film surface of the photo-anode S_2 (1.1 wt. %), which would be mainly as Ni_2H obtained from the electrodeposition and NiOOH obtained from the partial oxidation of nickel hydride in contact with the electrolyte during the electrodeposition.

Figures 5.9 and 5.10 show the Mo 3d XPS spectra for the undoped and nickel-doped molybdenum oxide films. As can be seen, the deposited films on the photo-anodes S_1 and S_2 contain the characteristic peaks of Mo^{4+} situated approximately at binding energies of 230 and 232 eV, attributed to the presence of MoO_2 (Table G.1), which agrees with the reaction 5.2 for both types of electrodes in section 5.1. However, at the same time it is possible to see in all the films two characteristic peacks of Mo^{6+} situated approximately at binding energies of 232 and 235 eV, which would indicate the presence of MoO_3 as well (Table G.1). The presence of this type of oxide in the films would be explained by the exposure of the electrodes to the atmosphere prior to the XPS analysis, which would lead to the surface oxidation of deposited films. Consistent with this research, Scanlon e*t al.* [79] reported that for the peak Mo 3d, samples of MoO_2 seemed to have a MoO_3 surface layer when these samples were exposed to the atmosphere prior to XPS analysis and, therefore, it is likely that the data included components associated with changes in the sample induced by exposure to oxygen.

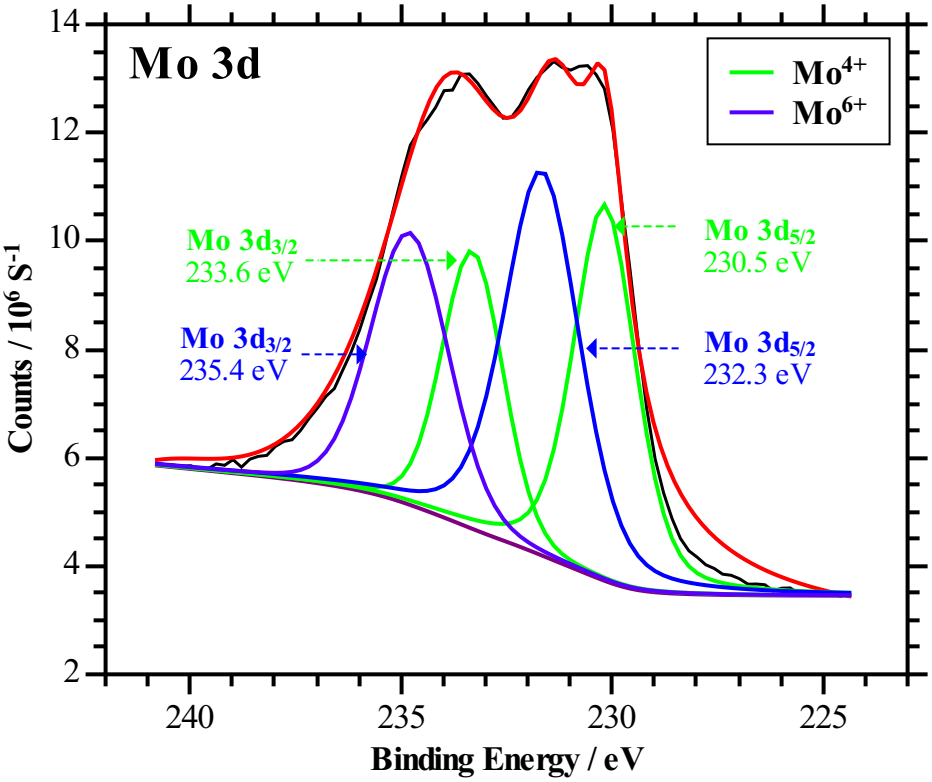

Figure 5.9: XPS spectrum of Mo 3d of photo-anode S_2.

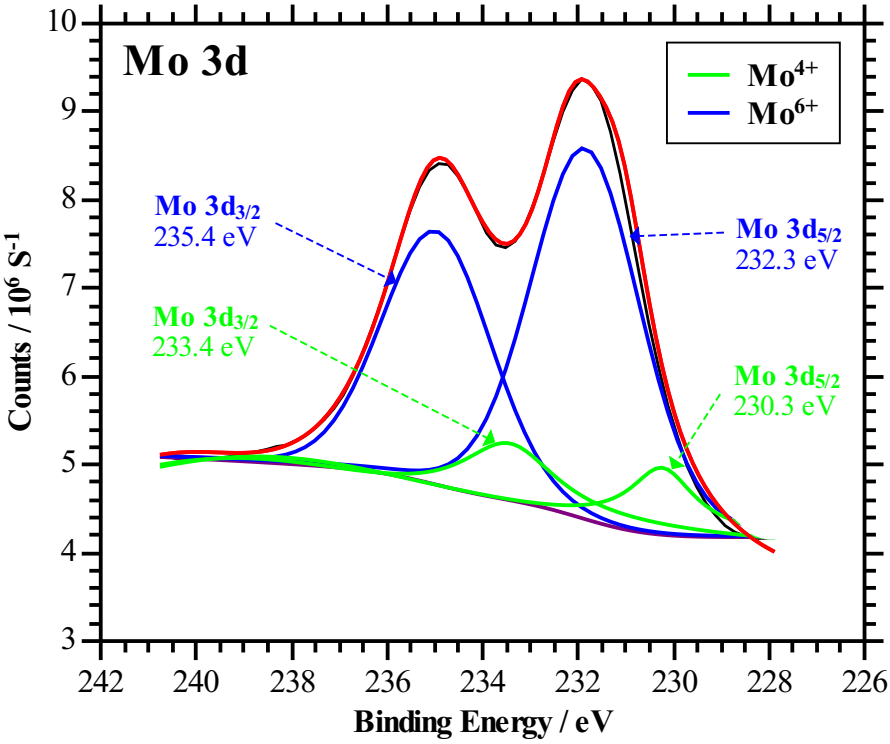

Figure 5.10: XPS spectrum of Mo 3d of photo-anode S_1.

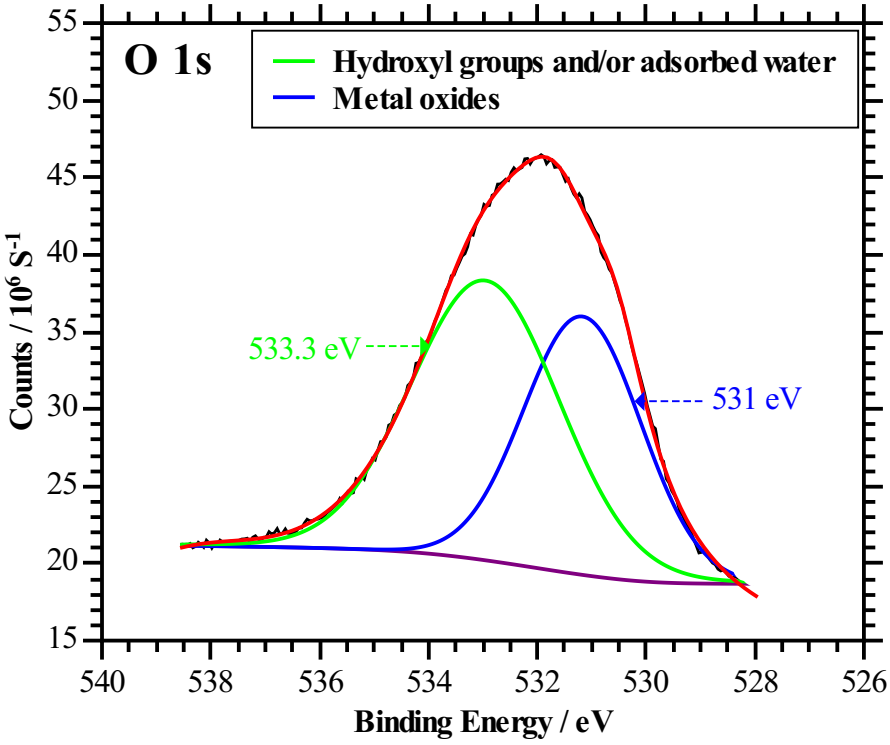

Figure 5.11: XPS spectrum of O 1s of photo-anode S_2.

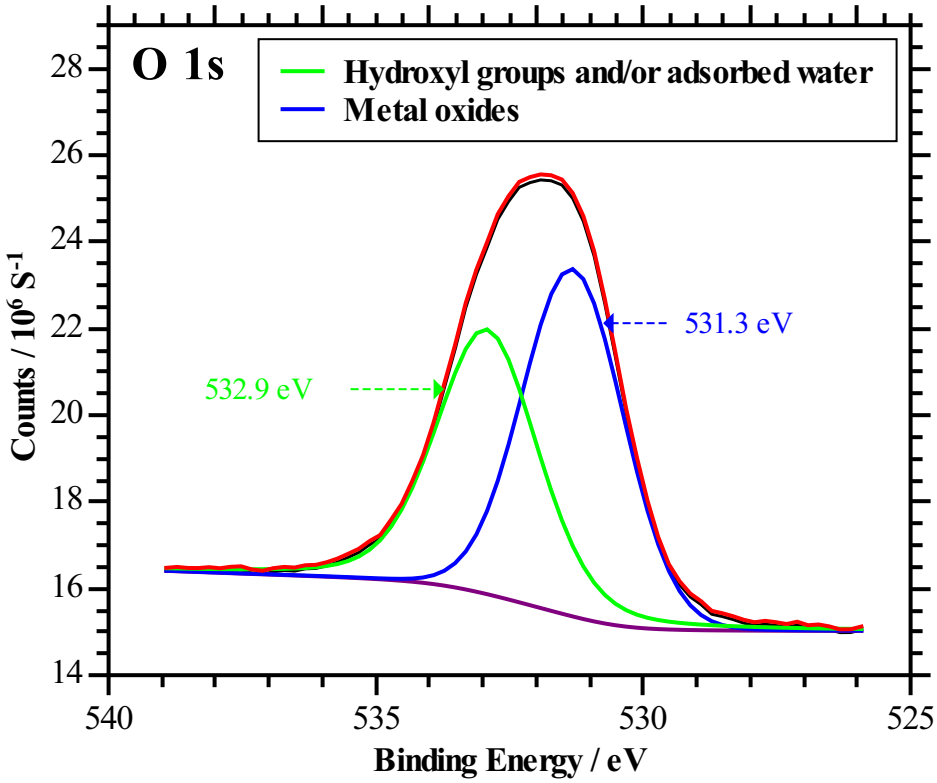

Figure 5.12: XPS spectrum of O 1s of photo-anode S_1.

The O 1s spectra for the films of the photo-anodes S_1 and S_2 are shown in Figures 5.11 and 5.12. It is possible to appreciate in all the films two peaks situated approximately at binding energies at 531 and 532 eV. In both photo-anodes the peaks at lower binding energies mainly corresponds to metal oxides such as MoO_2 and/or MoO_3, whereas the peaks at higher binding energies correspond to hydroxyl groups or adsorbed water on the surface i.e. Mo-OH [102][103].

All the photo-anodes (S_1 and S_2) presented a peak associated with carbon. The C 1s XPS spectra are presented in appendix G (Figures G.1 and G.2). The carbon signal detected would be associated with adventitious carbon normally found on the surface of the samples exposed to the air or growth of carbonates on the surface of oxides.

In Figure 5.13, the XPS spectra in the region of Ni 2p is shown for electrode S_2. For this sample, the Ni 2p exhibits a doublet Ni $2p_{1/2}$ and Ni $2p_{3/2}$. Analysis of the Ni $2p_{3/2}$ region shows a main component centred at 858 eV for the peak Ni^{3+}. This peak is assignable to nickel oxyhydroxide (NiOOH) [104][105], which could be formed from the partial oxidation of the nickel hydride formed in the film (see section 5.1) due to the presence of water in the electrolyte. The above can be described by the following equation:

$$Ni_2H_{(s)} + 2H_2O_{(l)} \rightarrow 2NiOOH_{(s)} + \frac{3}{2}H_{2(g)} \tag{5.6}$$

An additional peak at a higher binding energy (centered at 861 eV) can be seen in Figure

5.13, which could correspond to a satellite structure [12] [104][105]. It is important to mention that the presence of satellite structures for nickel compounds with 0, +2 and +3 oxidation states is common at higher binding energies [104][105]. In fact, in the case of the photo-anode S_2, the correct assignment can be compromised by the complex main line splitting due to multiplet contributions in oxyhydroxides and by satellite structures at higher binding energies particularly in the most intense Ni 2p spectra where often the satellite structures are wide.

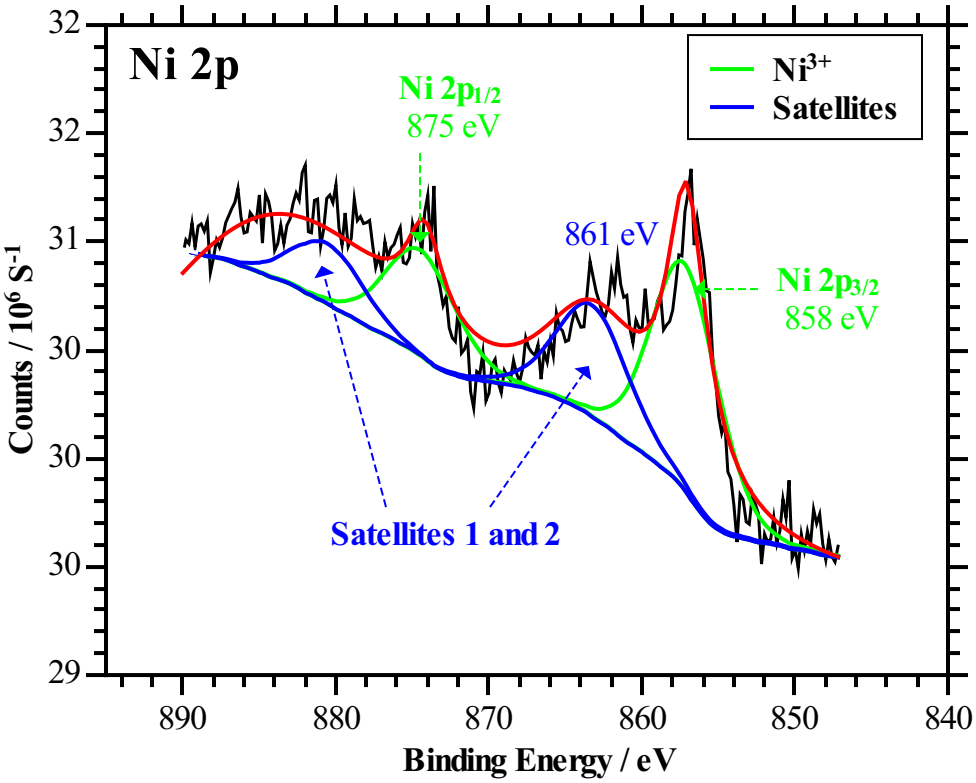

Figure 5.13: XPS spectrum of Ni 2p of photo-anode S_2.

5.4. Optical Characterization of Undoped and Nickel-Doped Molybdenum Oxide Photo-Anodes

In order to have a complete optical characterization, analysis by UV-Visible Spectroscopy and Tauc plots for the undoped and nickel-doped molybdenum oxide photo-anodes were performed.

UV-Visible Spectroscopy analysis was used in order to determinate the absorbance of the photo-anodes S_1 and S_2. Figure 5.14 shows the absorption spectra of the undoped and nickel-doped molybdenum oxide electrodes.

According to Figure 5.14, the photo-anodes S_1 and S_2 formed a similar pattern in the wavelengths range used in UV-Visible analysis. As can be seen, in the undoped and nickel-doped

[12] Satellite structures are due to a sudden change in Coulombic potential as the photo ejected electron passes through the valence band [106].

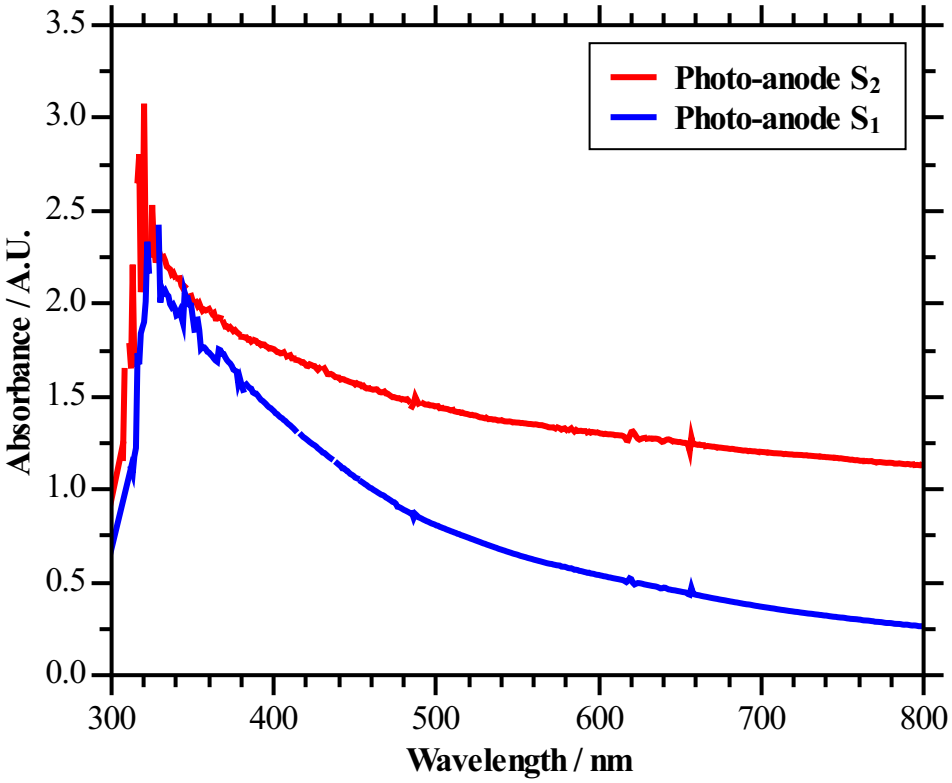

Figure 5.14: Absorption spectra of the obtained deposits in the synthesis of photo-anodes S_1 and S_2.

molybdenum oxide deposited films on FTO-coated glass, the absorption peak is reached at wavelengths below 400 nm. It is evident that the photo-anode S_2 had a greater absorption of light energy in the whole range of analyzed wavelengths, reaching its maximum in the UV region (the maximum absorbance of this electrode was ca. 3.1 at λ= 330 nm). As mentioned in Section 5.2, this behaviour can be attributed to the film morphology on the eletrode S_2 surface. The presence of irregularly shaped conglomerates on the electrode surface, promote large surface areas favoring the absorption of light energy [80].

In solar energy conversion systems, the optical band-gap energy (E_g) of a semiconductor electrode is a key parameter. Only photons of equal or higher energy than the band-gap energy will be absorbed by the semiconductor film. The optical band-gap value of the deposited films was determined by the analysis of Tauc plots.

Tauc plots of electrodes S_1 and S_2 are depicted in Figures 5.15 and 5.16. According to the Figure 5.15, the photo-anode S_2 exhibits a band energy value of 2.58 eV, which could be attributed to the incorporation of Ni^{3+} in the MoO_2/MoO_3 structures, contributing to the formation of a shallow donor energy level below of the conduction band of the molybdenum oxide. In contrast to this, the photo-anode S_1 has a higher band-gap (ca. 3.15 eV, Figure 5.16) than the values obtained in direct transitions in other research [21][81] for electrodeposited molybdenum oxides in similar conditions to this research, which implies that this type of electrode could present a greater resistance to the passage of electrodes from the valence band to the conduction band of the molybdenum oxide deposited on the FTO-coated glass.

Semiconductor materials large band-gap as in the case of the undoped molybdenum oxide photo-anodes results in a reduced use of the solar spectrum [66].

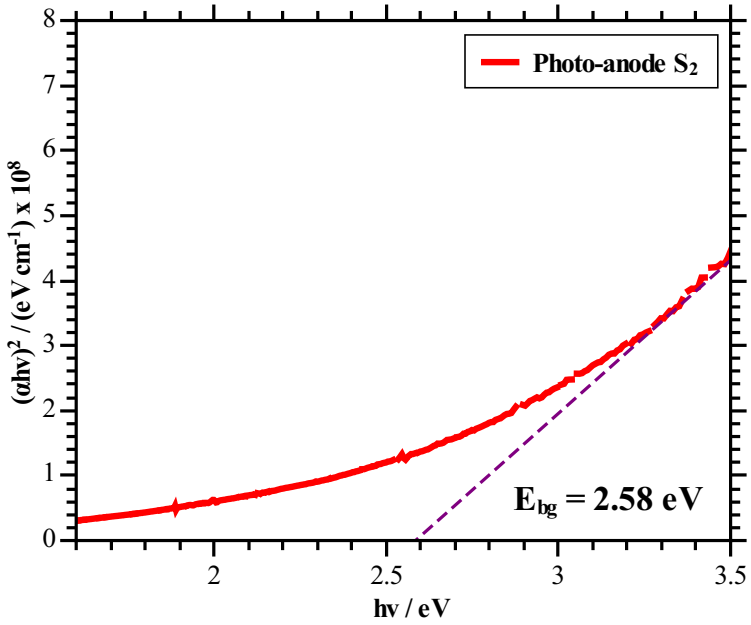

Figure 5.15: Allowed direct band-gap Tauc plot of the deposits obtained in the synthesis of the photo-anode S_2.

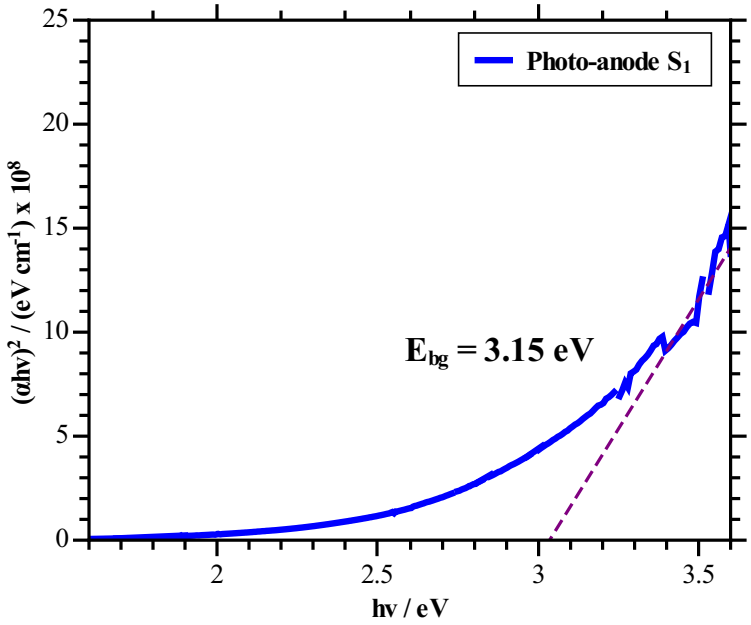

Figure 5.16: Allowed direct band-gap Tauc plot of the deposits obtained in the synthesis of the photo-anode S_1.

5.5. Photo-Electrochemical Characterization of the Undoped and Nickel-Doped Molybdenum Oxide Photo-Anodes

To determine the presence of photo-activity and conductivity type presented by the films, Open Circuit Potential (OCP) tests were performed. Each measurement was made alternating periods of darkness and light. In these experiments, white light and ultraviolet light (λ_{max} = 385 nm) were used as the source of illumination. The results are shown in Figures 5.17 and 5.18.

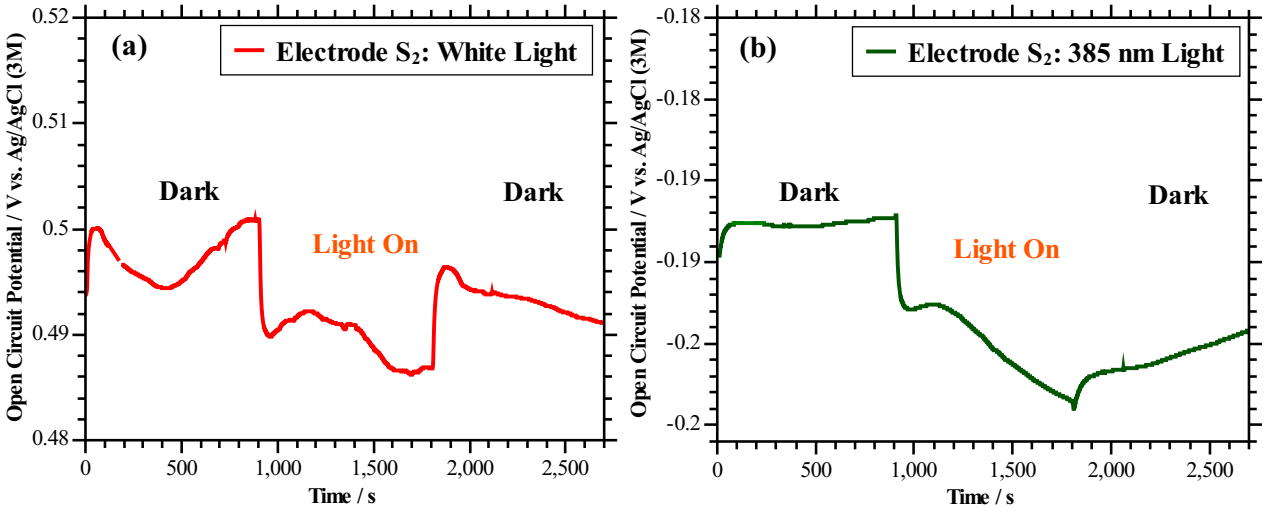

Figure 5.17: Open circuit potential curves of the electrode S_2. The measurements were made under white light and darkness for 45 minutes.

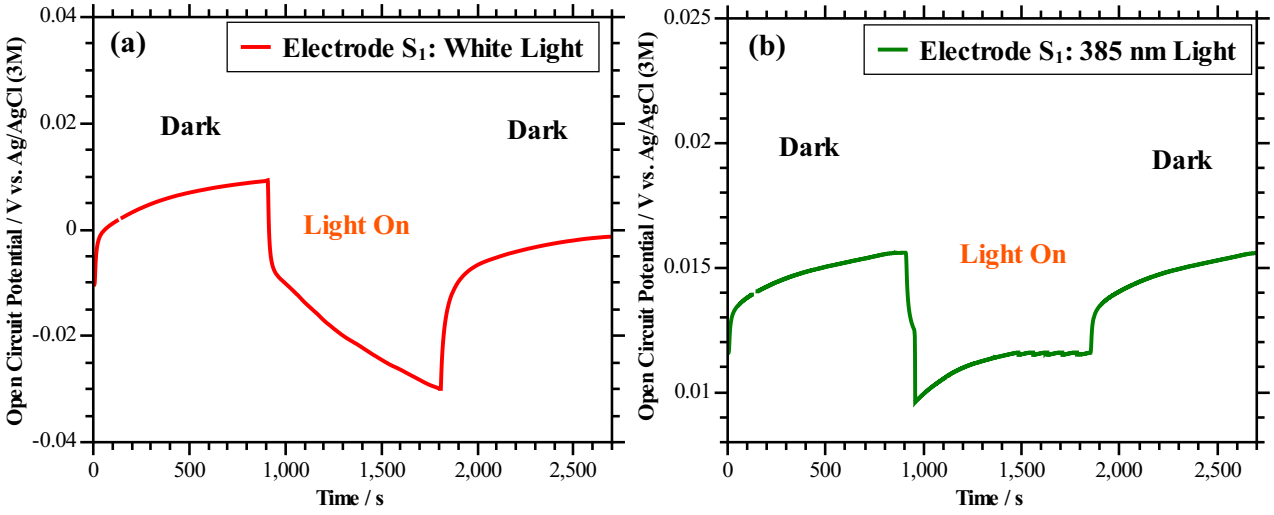

Figure 5.18: Open circuit potential curves of the electrode S_1. The measurements were made under white light and darkness for 45 minutes.

The photo-anodes S_1 and S_2 form a similar pattern during the OCP analysis. According to the information provided by Figures 5.17 and 5.18, when the electrodes are illuminated the potential curves move towards more cathodic values, regardless of the source of illumination. This indicates that photo-electrons and photo-holes are effectively separated (presence of photo-activity). Besides, these potential curve behavior is associated with n-type conductive materials (Appendix B, section B.1).

Representative linear sweep voltammograms of the electrodes S_1 and S_2 obtained in an electrolyte of Na_2SO_4 0.1 M at pH 3.5 are presented in Figures 5.19 and 5.20. Aditionally, in order to obtain a better understanding of the phenomena in the system in which the photo-electrochemical experiments were carried out, Eh-pH diagrams for the molybdenum and nickel species have been elaborated. Figures 5.21 and 5.22 shows the diagrams obtained which will be used to interpret and describe the processes that occur during the linear sweep voltammetries.

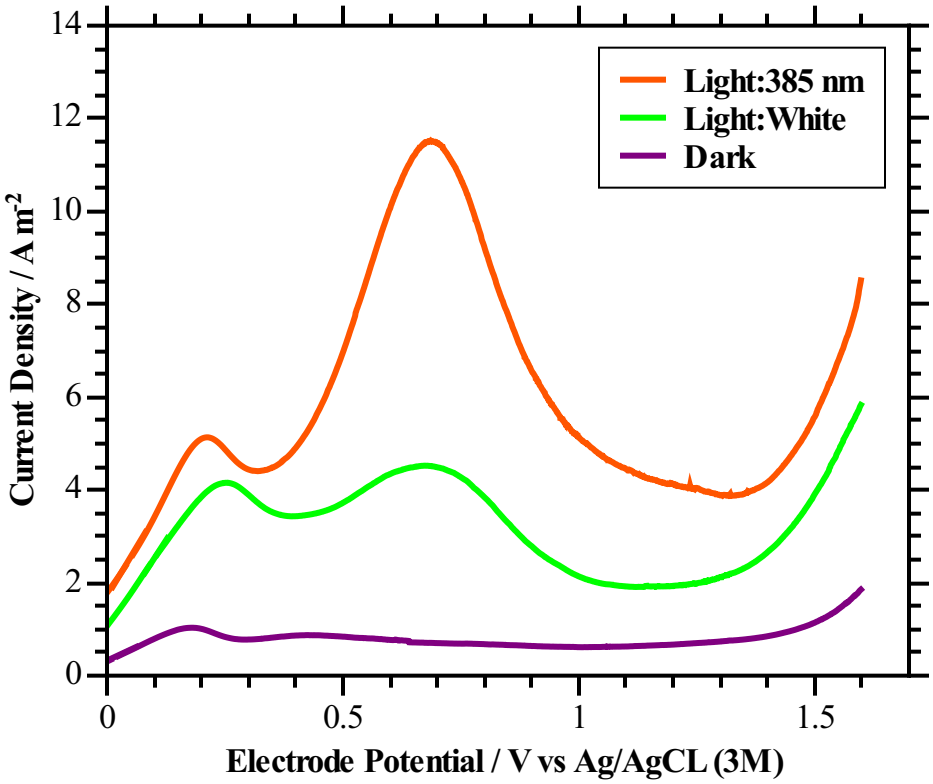

Figure 5.19: Linear sweep voltammograms of the electrode S_2 obtained in an electrolyte of Na_2SO_4 0.1 M at pH 3.5 under dark, white light and UV illumination (wavelength = 385 nm).

The analysis of the linear sweep voltammetries (Figure 5.19) for the photo-anode S_2 shows two peaks centered at 0.2 V (ca. 0.4 V vs SHE) and 0.75 V (ca. 0.95 V vs SHE) when the electrode is illuminated (white light and UV light). These peaks could be associated to the redox transition of Mo^{4+} to Mo^{6+}. Likely, in the acidic electrolyte used in this voltammetry, the formation of H_2MoO_4 from the MoO_2 present in the electrode surface begins at this

potential range according to the following reaction mechanism:

$$HMoO_{3(s)} + H^{+}_{(aq.)} + \mathrm{e}^{-} \leftarrow MoO_{2(s)} + H_2O_{(l)} \tag{5.7}$$

$$H_2MoO_{4(aq.)} + H^{+}_{(aq.)} + \mathrm{e}^{-} \leftarrow HMoO_{3(s)} + H_2O_{(l)} \tag{5.8}$$

The above agrees with the information provided by Eh-Ph diagram in Figure 5.22, where it is possible to appreciate that at the indicated pH and potential range, the formation of H_2MoO_4 from the MoO_2 is favored.

On the other hand, the second peak also could be caused by the formation of $NiO_2(H_2O)$ from NiOOH present in the film surface, according to the Eh-pH diagram in Figure 5.21. The formation of $NiO_2(H_2O)$ is given by the following reaction:

$$NiO_2(H_2O)_{(s)} + H^{+}_{(aq.)} + \mathrm{e}^{-} \leftarrow NiOOH_{(s)} + H_2O_{(l)} \tag{5.9}$$

As can be seen in the voltamogram in Figure 5.19, when the electrode is illuminated under UV and white light there is an increase in the current density curves from ca. 1.3 V (ca. 1.5 V vs SHE) that would correspond mainly to two phenomena: (i) the PEC oxygen evolution reaction present at the anode surface, which is to be expected in that potential zone. The PEC oxygen evolution reaction is given by the next equation:

$$\frac{1}{2}O_2(g) + 2H^{+}_{(aq.)} + 2\mathrm{e}^{-} \leftarrow H_2O_{(l)} \tag{5.10}$$

And (ii) the possible increase in the photo-corrosion of the deposited film. It is possible to assume that this behavior could be due to the photogenerated charge carriers in that potential zone favor a more accelerated and/or strong semiconductor decomposition, resulting in instability under illumination in the electrolyte [107].

In the LSV under dark polarization conditions of the photo-anode S_2, the presence of a small peak around 0.2 V can be observed. This peak indicates that the MoO_2 present in the deposited film could be dissolving in the electrolyte (equations 5.7 and 5.8). The current increase at 1.4 V under darkness is related to the electrochemical oxidation of water molecules (equation 5.10).

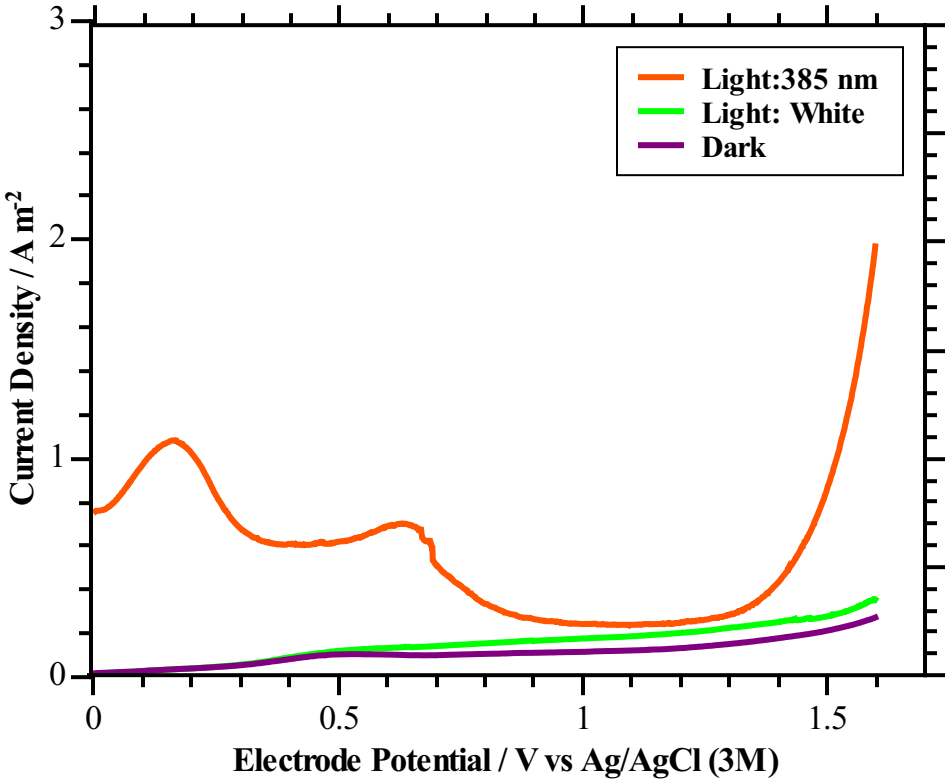

Figure 5.20: Linear sweep voltammograms of the electrode S_1 obtained in an electrolyte of Na_2SO_4 0.1 M at pH 3.5 under dark, white light and UV illumination (wavelength = 385 nm).

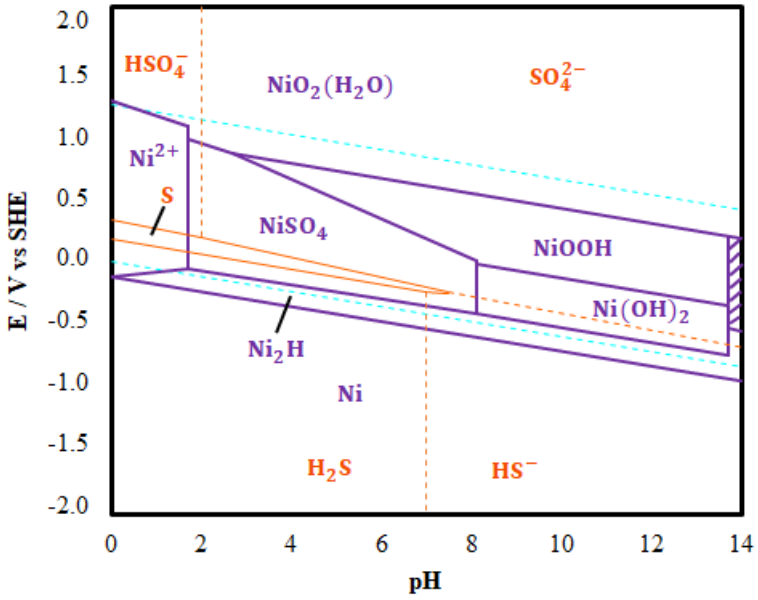

Figure 5.21: Eh-pH diagrams for nickel at 298 K and 10^5 Pa. Activity of nickel species equal to 10^{-6} and activity of sulfate species equal to 10^{-2}.

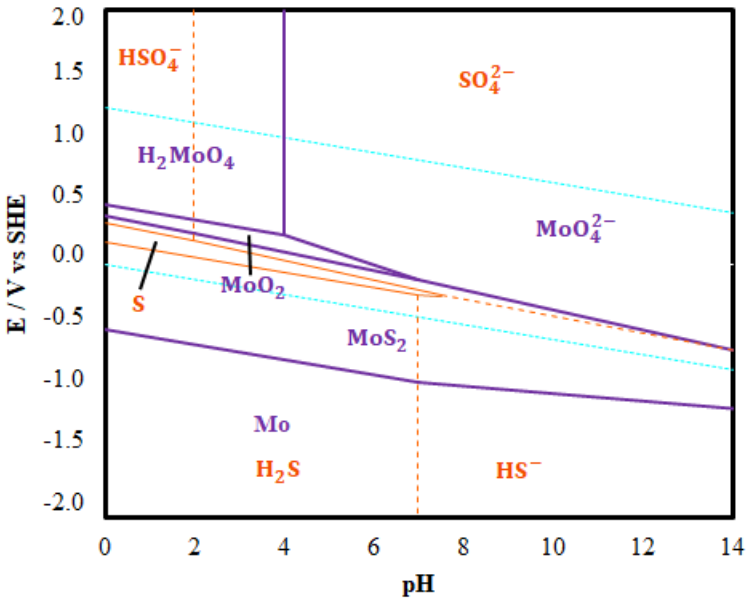

Figure 5.22: Eh-pH diagrams for molybdenum at 298 K and 10^5 Pa. Activity of molybdenum species equal to 10^{-6} and activity of sulfate species equal to 10^{-2}.

With respect to the photo-anode S_1, it is possible to see that under ultraviolet illumination the current density curve (Figure 5.20) presents similar peaks to the voltammograms obtained for the photo-anode S_2 under light conditions. This suggests that the formation of H_2MoO_4 is present during the study performed by voltametry in this electrode. When the voltammetries are performed with white light or in dark conditions, the presence of a small peak around 0.6 V (ca. 0.8 V vs SHE) can be observed. This peak indicates that the MoO_2 present in the deposited film could be dissolving in the solution. In the case of this electrode, an increase in the current density curve under UV illumination can also be observed from ca. 1.4 V (ca. 1.6 V vs SHE) which correspond to the PEC oxygen evolution reaction present at the anode surface.

For the undoped and nickel-doped molybdenum oxide photo-anodes, long term stability tests under UV and white illumination at 1.23 V vs RHE were performed to simulate water splitting conditions (since most materials studied to date cannot split water spontaneously), during 60 minutes. Figures 5.23-5.26 show the behavior of these electrodes in the stability tests.

The results of these tests show that for the undoped and nickel-doped molybdenum oxide photo-electrodes that the current densities decrease rapidly ($<$600 seconds) reaching values close to zero when applying a potential of 1.23 V. Photocurrent-time curves confirm that these photo-electrodes exhibit a poor photo-stability. It is possible that this behavior is a combination of (i) a chemically unstable photo-anode in the solution under the experimental conditions, and (ii) photo-corrosion.

The analysis performed using LSVs and Eh-pH diagrams showed that photo-anodes are chemically unstable in solution in the dark or during illumination generating mainly H_2MoO_4 from MoO_2. In this case, efforts should be made to find an adequate electrolyte and suita-

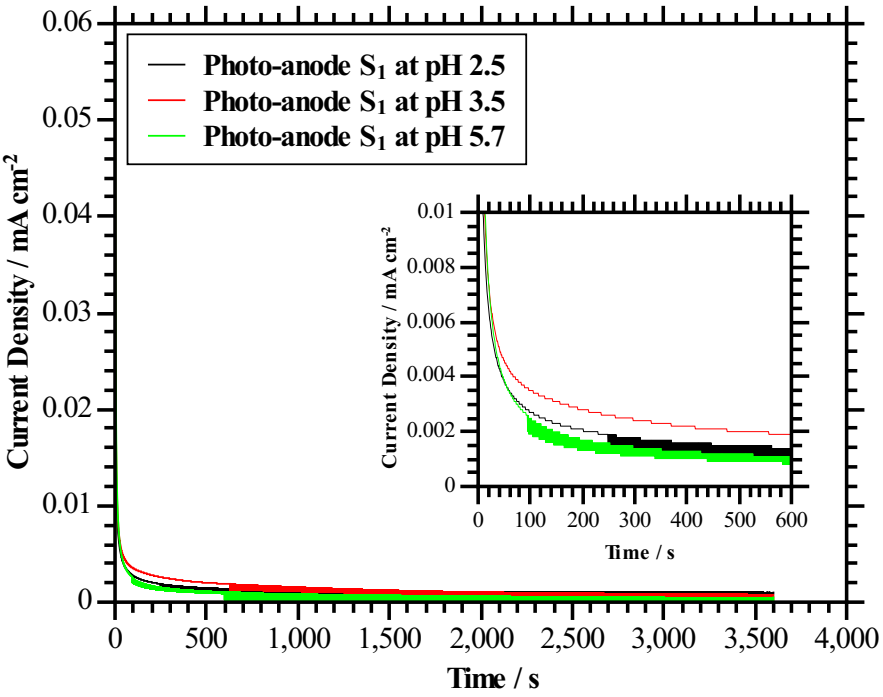

Figure 5.23: Photo-current vs Time Curves at 3 different pH: 2.5; 3.5 and 5.7. All of them at 1.23 V vs RHE at 20 mV s^{-1}, during 60 minutes and UV light (385 nm).

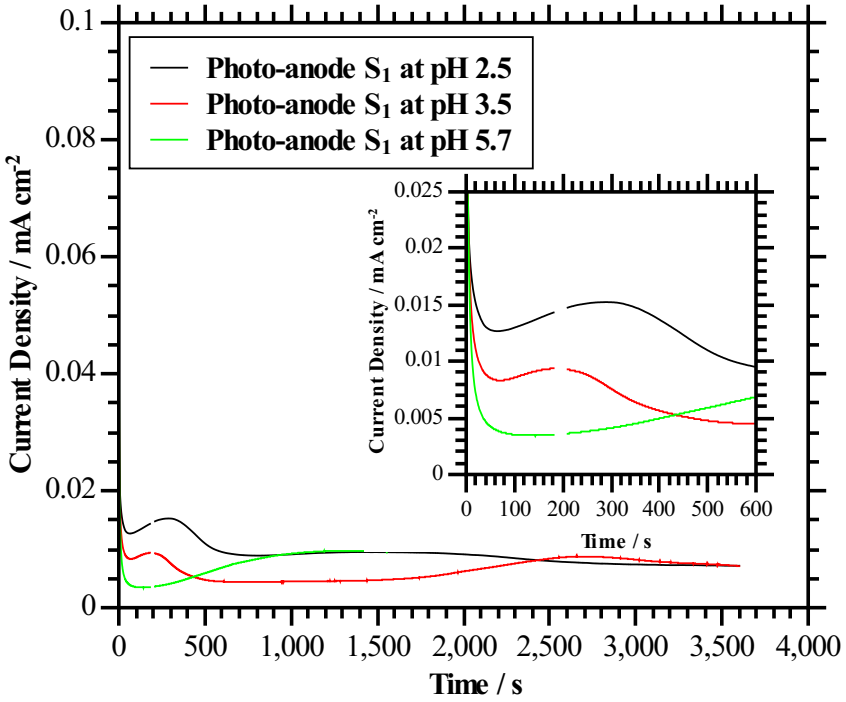

Figure 5.24: Photo-current vs Time Curves at 3 different pH: 2.5; 3.5 and 5.7. All of them at 1.23 V vs RHE at 20 mV s^{-1}, during 60 minutes and white light.

ble experimental conditions (potential, pH or post-calcination treatment) in order that the

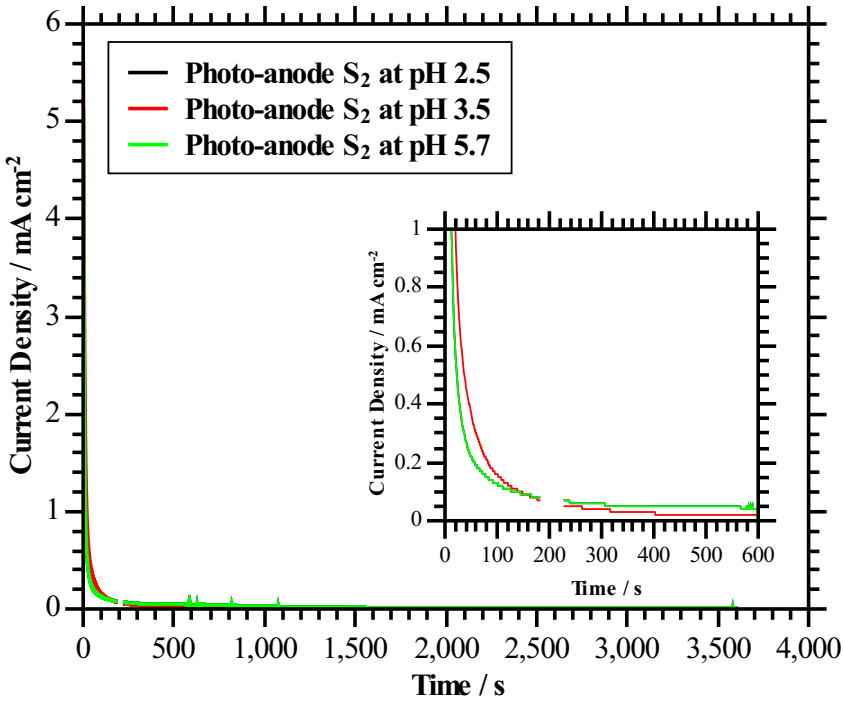

Figure 5.25: Photo-current vs Time Curves at 3 different pH: 2.5; 3.5 and 5.7. All of them at 1.23 V vs RHE at 20 mV s^{-1}, during 60 minutes and UV light (385 nm).

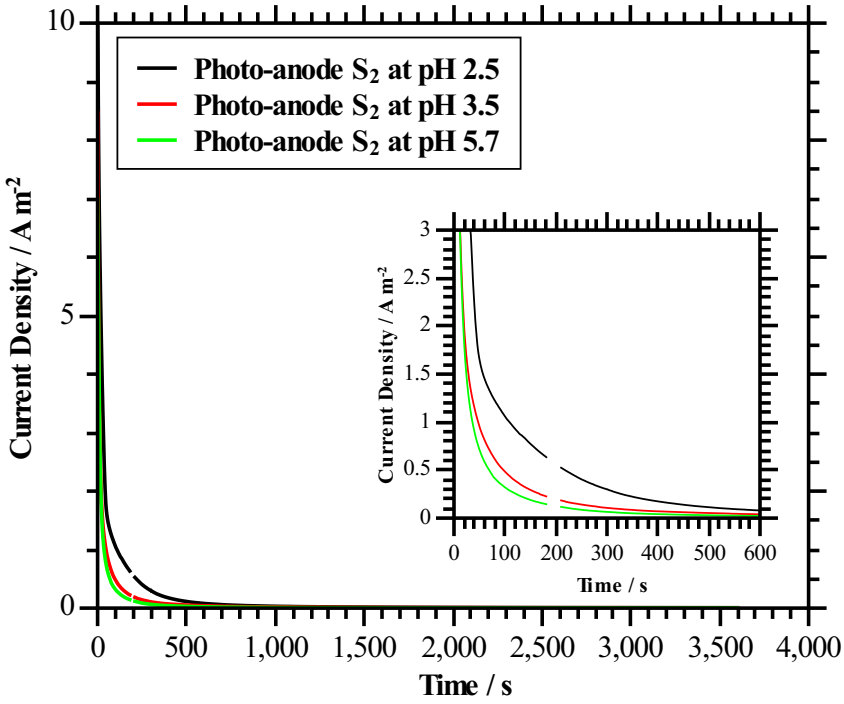

Figure 5.26: Photo-current vs Time Curves at 3 different pH: 2.5; 3.5 and 5.7. All of them at 1.23 V vs RHE at 20 mV s^{-1}, during 60 minutes and white light.

electrodes can efficiently absorb sunlight to generate electron-hole pairs and that have a high mobility and long lifetime to prevent electron-hole recombination within the material before the electron-hole pairs reach the electrode(s) | electrolyte interface. Indeed, Morales *et. al* [24] have reported that for water splitting applications, these films would need a post-calcination treatment in order to obtain a stable photo-anode.

Additionally, the LSVs performed when the photo-anodes are illuminated (UV and white light) showed the possible influence of the photo-corrosion on the electrodes photo-stability. Photo-corrosion in aqueous environments is one of the most significant obstacles to the widespread deployment of semiconductor materials as PEC cells for solar hydrogen production. The photo-generated holes and electrons in semiconductor electrodes are generally characterized by strong oxidizing and reducing potentials, respectively. Instead of driving the OER or HER, these holes and electrons may oxidize or reduce the semiconductor itself, causing undesired physical and chemical changes. Ling-Ju *et. al.* [107] have reported that the energy position of the conduction and valence bands edges, rather than the width of the band-gap, determines the stability of a semiconductor under illumination in aqueous solution. Considering the results obtained in the LSVs and stability tests, it is possible to assume that the photo-anodes surface is susceptible to oxidative photo-decomposition which means that photogenerated holes prefer to drive the self-decomposition of the photo-anodes instead of the water oxidation reaction when the electrodes are illuminated. The above would be caused because of the less positive oxidative photo-decomposition potential than the OER potential X. For a more thorough understanding, Figure 5.27.(a) illustrates a stable photo-electrode against photo-corriosion, while Figure 5.27.(b) shows a semiconductor which is susceptible to oxidative photo- decomposition because of the less positive oxidative photo-decomposition potential than the OER potential as is the case of the undoped and nickel-doped molybdenum oxide photo-electrodes.

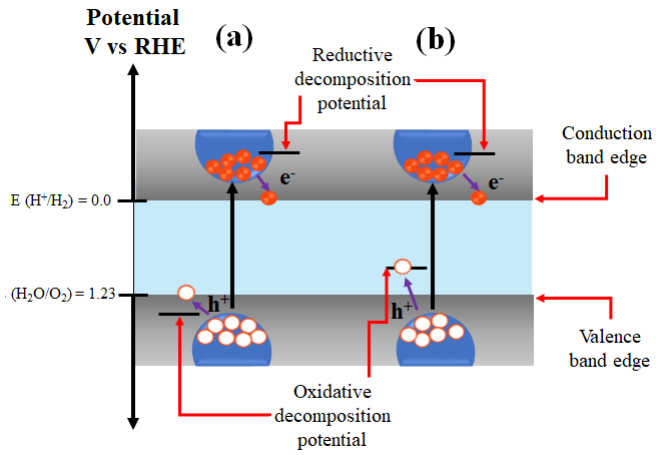

Figure 5.27: Classification of the semiconductor decomposition-redox potentials with respect to the water-redox potentials: (a) The semiconductor is stable against photo-corrosion; (b) The semiconductor is susceptible to oxidative photo-decomposition. Adapted from [107]

.

5.6. Chapter Summary and Conclusions

Undoped and nickel-doped molybdenum oxide films were electrodeposited by applying -1.377 V vs Ag/AgCl (3 M KCl) during 3 hours on an FTO-coated glass substrate immersed in molibdate-citrate aqueous solutions.

Eh-pH diagrams developed by Morales *et. al.* [24] were used in order to identify the electrodeposited species on the substrate for each fabricated electrode. From this study, it was determined that the MoO_2 is the species formed on the undoped molybdenum oxide electrode surface (photo-anode S_1), while the MoO_2-Ni_2H alloy would form the the nickel-doped molybdenum oxide film (photo-anode S_2).

The microstructure of the photo-anodes was analysed using SEM and AFM techniques. From these analysis, it was determined that unlike the undoped molybdenum oxide film morphology which forms an orderly and homogeneous pattern over the entire photo-anode surface, the nickel-doped molybdenum oxide films morphology is heterogeneous and irregular with "hill- like" conglomerates of random orientation on top of sustrate. In addition, the doped film has an average thickness of 763 nm, while the electrode S_1 has a deposited film with an average thickness of 438 nm. All this suggests that the nickel doping had a significant impact on the morphology type and the deposited film thickness.

The composition and chemical state of the elements forming the films were characterized by X-Ray Photoelectron Spectroscopy (XPS) and Energy-dispersive X-ray Spectroscopy (EDS or EDX). It was concluded that the photo-anodes surface was partially modified (oxidized) due to the interaction with the atmosphere and the electrolyte during the electrodeposition. It was revealed by XPS that MoO_3 and NiOOH are present as a result of partial oxidation of the MoO_2-Ni_2H alloy in the photo-anode S_2, while MoO_3 was detected in the photo-anode S_1 product of the partial oxidation of MoO_2 on the eletrode surface. On the other hand, EDS analysis shows in all the electrodes the presence of Mo (over 40 % wt.) and O (over 55 % wt.), which confirms that the films are composed of molybdenum oxides. Moreover, nickel in small quantities (1.1 % wt.) was found in the nickel-doped molybdenum oxide photo-anode, which would be mainly as Ni_2H obtained from the electrodeposition and NiOOH obtained from the partial oxidation of nickel hydride in contact with the electrolyte during the electrodeposition process.

The photo-anodes S_1 and S_2 absorb UV and blue light (ca. wavelengths from 300 to 500 nm) and present a direct (allowed transitions) band-gap. Tauc plots showed that the nickel-doped molybdenum oxide film of irregular morphology had the lowest optical band-gap energy value (2.58 eV) as compared with the photo-anode S_1 (3.15 eV), that results in a better use of the solar spectrum.

These photo-anodes are susceptible to oxidative photo-decomposition which means that photogenerated holes prefer to drive the self-decomposition of the photo-anodes instead of the water oxidation reaction when the electrodes are illuminated. The above would be caused due to the oxidative photo-decomposition potential is less positive than the OER potential.

The undoped and nickel-doped molybdenum oxide photo-anodes have an optimal band-gap (electrode S_1: 3.15 eV and electrode S_2: 2.58 eV) for harnessing sufficient sunlight but

it do not present a favorable band-edge positions for driving overall water splitting and do not exhibit a stability in aqueous solution, which are the main limiting factors for the use of conventional photovoltaic semiconductors as photo-electrodes.

For chemically stable photo-anodes, efforts should be made to find an adequate electrolyte and suitable experimental conditions (potential, pH or post-calcination treatment). In the case of the undoped and nickel-doped molybdenum oxide photo-electrodes, Morales e*t. al* [24] have reported that for water splitting applications, these films would need a post-calcination treatment in order to obtain stable photo-anodes. It is suggested to avoid contact with acid solutions of these photo-anodes, since it favor the degradation of deposited films. Moreover, when carrying out characterizations by voltammetries, it is recommended not to apply cathodic potentials, due to the possible formation of sulfides on the electrodes surfaces.

Chapter 6

Synthesis and Characterization of MoO_x, WO_3 and W-doped MoO_x Photo-Anodes

This chapter presents and discusses the synthesis and characterization of MoO_x, WO_3 and W-doped MoO_x photo-anodes. The films were synthesized by spin-coating at 4,000 RPM applied for 40 seconds. Post-deposition heat treatment of the films was performed at 470 °C. The films composition and crystallinity were characterized by XRD analysis.

In order to have a complete optical characterization, UV-visible spectrophotometry data was analysed using Tauc plots, to determine the films band-gap, and photo-electrochemical performance of photo-anodes was evaluated by photocurrent-potential (J-V) and photocurrent-time (J-t) curves.

6.1. Spin-Coating Process: Synthesis of MoO_x, WO_3 and W-doped MoO_x Photo-Anodes

The spin-coating experiments were carried out according to the protocol described in subsection 4.6.1. Figure 6.1 shows the films obtained at 4,000 RPM applied for 40 seconds for the synthesis of photo-anodes and subsequent heat treatment at 470 °C for 2 hours.

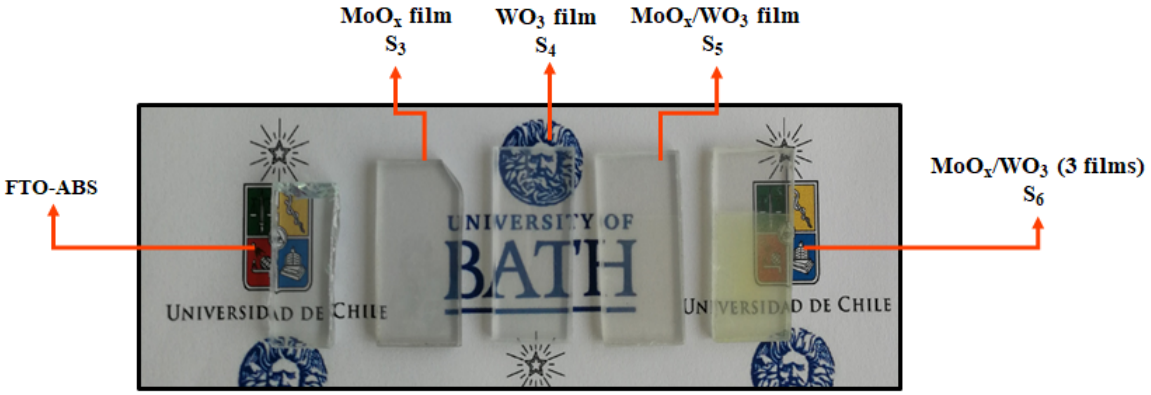

Figure 6.1: Obtained deposits by spin-coating.

As can be seen in Figure 6.1, most of the films obtained by spin-coating are almost transparent (electrodes S_3, S_4 and S_5). It is important to mention that all these transparent electrodes have a film composed of a single layer. The only exception is the photo-anode S_6 which has a film composed of three layers. This electrode presents a slight yellow coloration due to the presence of tungsten oxide [108] .

In order to have a global characterization of these films, microstructural, compositional, optical and photo-electrochemical analyzes were performed, which are described in the following subsections.

6.2. Microstructural Analysis of MoO_x, WO_3 and W-doped MoO_x Photo-Anodes

The morphology of the synthesized films was evaluated using Scanning Electron Microscopy (SEM). Figure 6.2 shows SEM images of the surface of the photo-anodes prepared by spin-coating and subsequent annealing at 470 °C.

The pure MO_x film image is shown in Figure 6.2(a). The photo-anode S_3 does not exhibit a homogeneous morphology, since it is possible to see substrate areas. In addition, the deposit presents conglomerates of irregular shape. Probably these areas are composed of molybdenum trioxide, MoO_3, because it is the most stable form of the molybdenum oxides after of annealing processes at high temperatures.

An SEM image of a pure WO_3 film is shown in Figure 6.2(b). It seems that only FTO-ABS is present in this sample, which could be explained by an extremely thin WO_3 film produced on the surface of the substrate. This observation is corroborated by XRD analysis

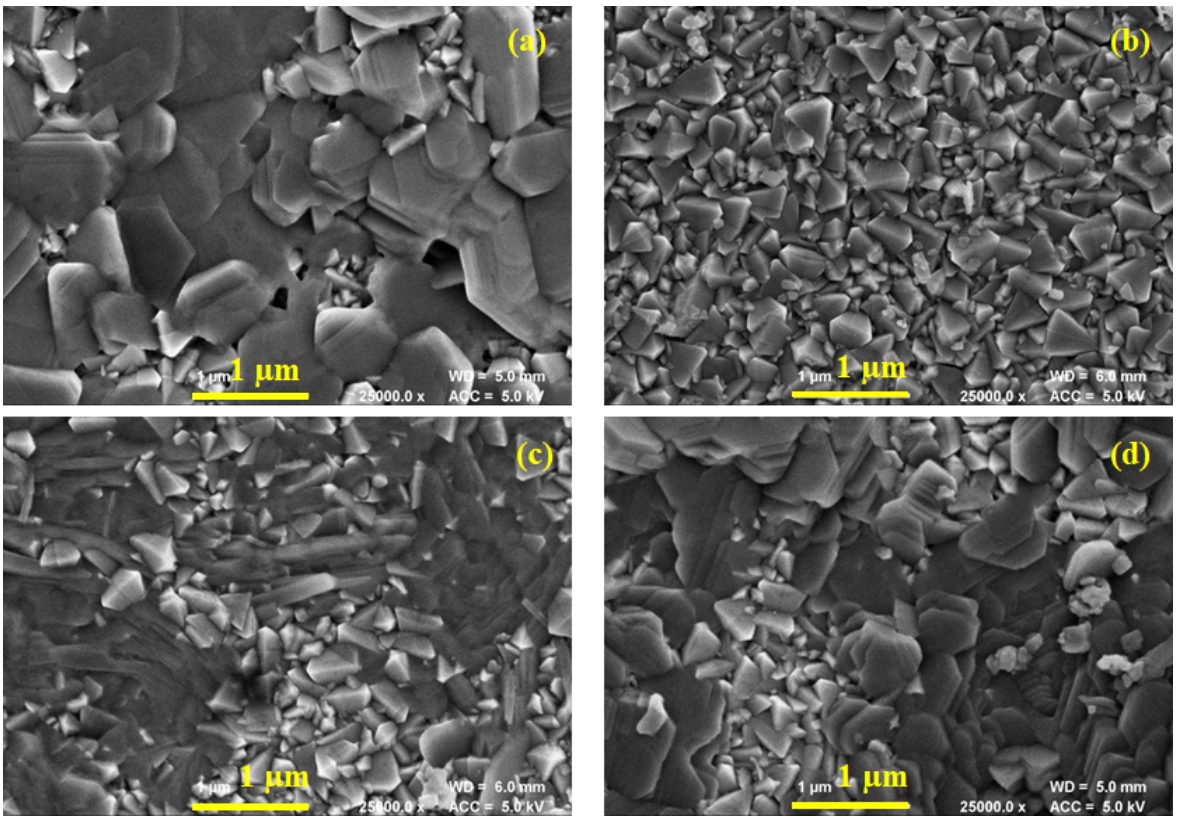

Figure 6.2: SEM images of electrodes: (a) S_3, (b) S_4, (c) S_5 and (d) S_6.

and photo-activity measurements, which show that there is a deposited film on the sustrate (see Sections 6.3 and 6.5 for more details).

The surface morphology of the films S_5 and S_6 are presented in Figures 6.2(c)-(d). It is possible to appreciate that the electrodes S_5 and S_6 present a microstructure similar to that presented by the electrode S_3 (MoO_3 film). Probably this photo-anodes are composed by MoO_3 (conglomerates of irregular shape) and WO_3 (areas that at first glance seem to be only substrate).

6.3. Compositional Analysis of the MoO_x, WO_3 and W-doped MoO_x Photo-Anodes.

The films composition and crystallinity were characterized by XRD analysis. Figure 6.3 shows the XRD patterns of the resulting films on FTO-ABS.

According to the XRD patterns of the fabricated films on FTO-ABS in Figure 6.3, the photo-anodes S_3, S_5 and S_6 exhibit diffraction peaks corresponding to orthorhombic structure of MoO_3. Indeed, these diffraction peaks (at 2θ 25.8 and 37.8°) are indexed to the diffraction planes (0 4 0) and (0 6 0) of crystalline orthorhombic structure of MoO_3 (database: JCPDS no. 05–0508 [109]). This suggests that after annealing at 450 °C, that irregular shape conglomerates distributed on top of the sustrate could be molybdenum oxide (VI). Complementary studies such as EDS analsis would help in determining a more accurate composition of these

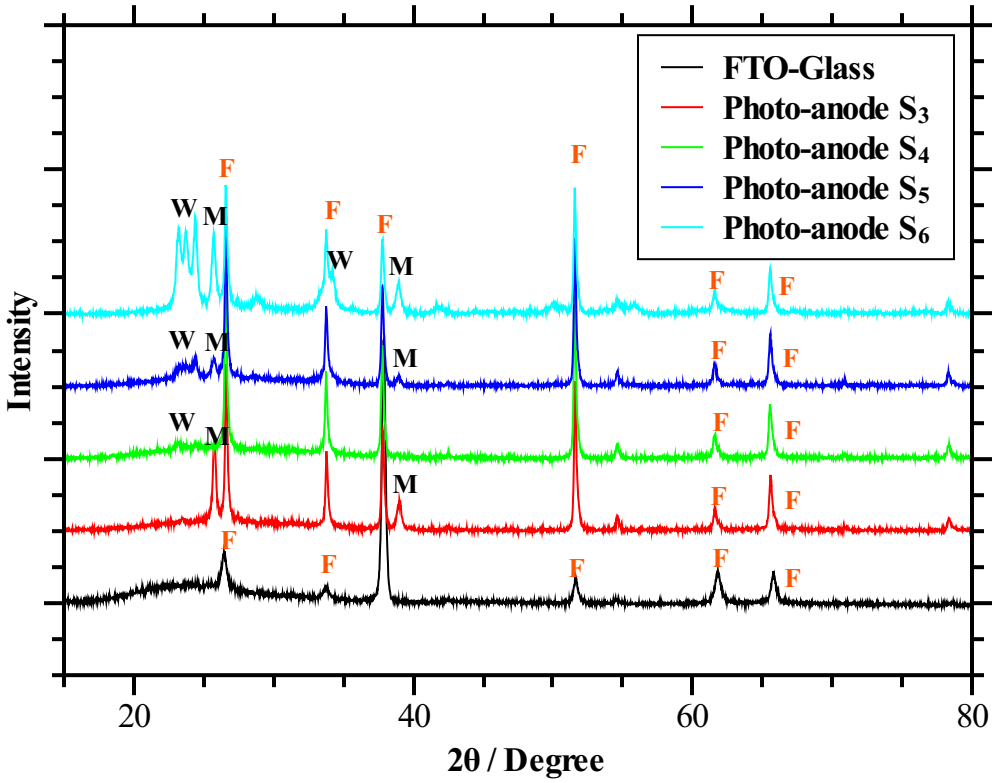

Figure 6.3: XRD patterns of the MoO_x, WO_3 and W-doped MoO_x photo-anodes.

electrodes.

The XRD data show a diffraction peak triplet at 2θ 23.2, 23.7 and 24.4 ° in the photo-anodes S_4, S_5 and S_6 and aditionally, a minor intensity peak at 34.4 ° in the electrode S_6 which corresponds to (0 0 2), (0 2 0), (2 0 0) and (2 0 2) diffraction planes, indicating a monoclinic crystal structure of WO_3 in accordance with JCPDS-ICDD card no. 89-4476 [110]. It is important to mention that, although the morphological analysis by SEM did not show the presence of WO_3 films in the S_4 electrode, the XRD analysis confirms that this photo-anode has a WO_3 layer on top of the sustrate, which probably was not detected by SEM due to its thickness. From this analysis it can be concluded that the electrodes S_5 and S_6 are composed of an alloy of MoO_3-WO_3.

6.4. Optical Characterization of MoO_x, WO_3 and W-doped MoO_x Photo-Anodes

Analysis by UV-Visible Spectroscopy for the photo-anodes was performed. The above is illustrated in Figure 6.4.

According to this Figure, the photo-anodes formed a similar absorption pattern in the wavelengths range used in UV-Visible analysis. As can be seen, in these electrodes the absorption peak is reached at wavelengths below 400 nm. It is evident that the photo-anode S_6 had a greater absorption of light energy in the whole range of analyzed wavelengths, reaching

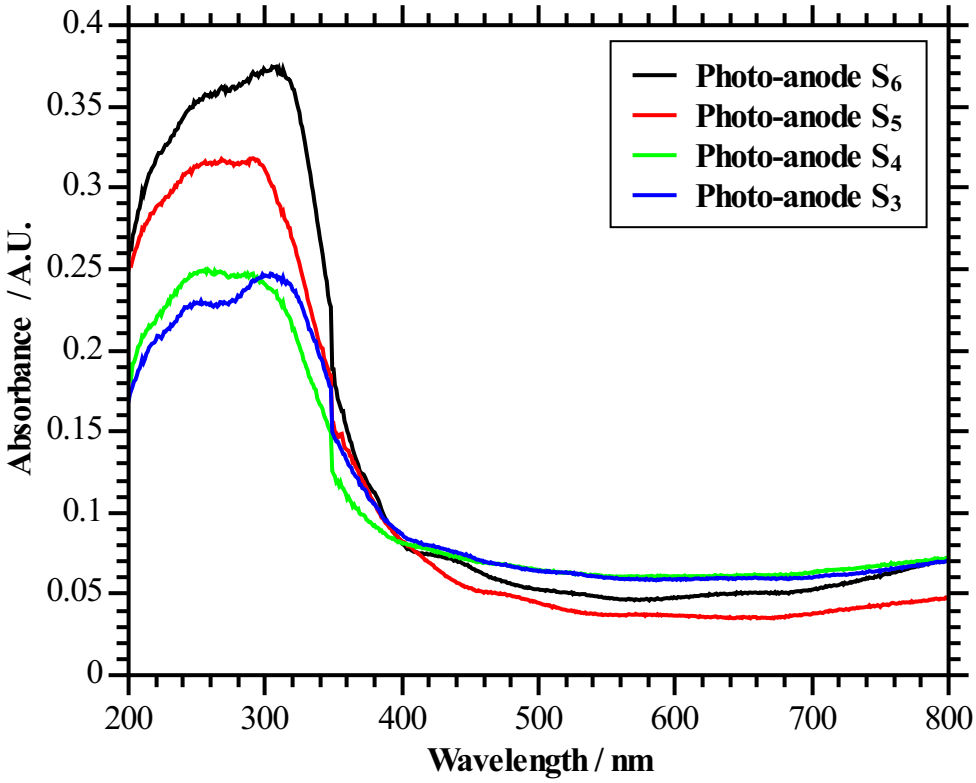

Figure 6.4: Absorption spectra of the obtained deposits in the synthesis of photo-anodes S_3, S_4, S_5 and S_6.

its maximum in the UV region. This behavior could be caused by the greater amount of material in this electrode (3 deposited layers in the film).

On the other hand, XRD patterns in Figure 6.3 show that there are two different phases in some samples (electrodes S_5 and S_6). This means that in this photo-anodes there are two types of crystals, so it was expected to obtain two absorption peaks, but it is only possible to see a peak not well defined on the UV-Vis spectra for this samples. The previous behavior could be caused because of overlapping and not well defined crystals (or small crystals). In such situation, the band-gap can not be measured reliably because the band-gap does not exist well defined.

6.5. Photo-Electrochemical Characterization of MoO_x, WO_3 and W-doped MoO_x Photo-Anodes

The Photo-electrochemical performance of the photo-anodes synthesized was evaluated by photocurrent-potential (j-E) and photocurrent-time (j-t) curves, which are shown in Figure 6.5 and Figure 6.6, respectively.

Aditionally, in order to obtain a better understanding of the phenomena in the system in which the photo-electrochemical experiments were carried out, Eh-pH diagrams for the molybdenum and tungsten species have been elaborated. Figures 6.7 and 5.22 show the

diagrams obtained which were used to interpret and describe the processes that occur during the photo-electrochemical measurements.

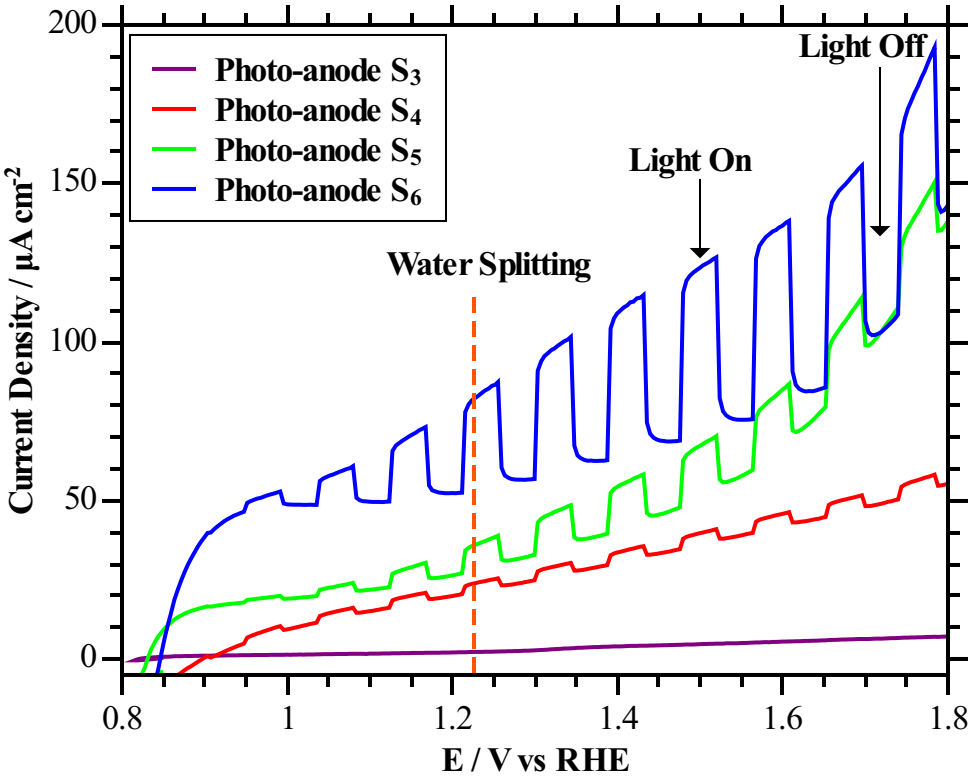

Figure 6.5: Current density-potential curves of the photo-anodes S_3, S_4, S_5 and S_6.

j-E curves (Figure 6.5) indicate that photo-anode S_6 outperforms the rest, reaching about 80 μA cm^{-2} at 1.23 V vs RHE which is the minimum potential required for the water splitting. This suggests that the amount of layers forming the film obtained by spin-coating has a significant effect on the photo-anode performance. This improvement would be due to the fact that there is more material that promote large surface areas in the photo-anodes produced, which in turn must result in better light exposure and more active sites for the PEC oxygen evolution reaction.

Photo-current time curves at 1.23 V vs RHE in Figure 6.6 also confirm that photo-anode S_6 exhibits a good photo-current performance in comparison to the rest. However, these results also reveal that all the electrodes lose stability during the experiment (the photo-current decrease). According to the Eh-pH diagrams in Figures 6.7 and 5.22, the conditions at which the experiments were performed could influence the electrode stability in the photo-electrochemical tests. In fact, WO_4^{2-} and MoO_4^{2-} seem to be the most stable forms of tungsten and molybdenum at the applied potential and at the pH of the electrolyte used in these experiments (pH 6.73 and 1.23 V vs RHE). This, suggests that changing some experimental parameters such as pH or/and electrolyte composition could be considered for future experiments.

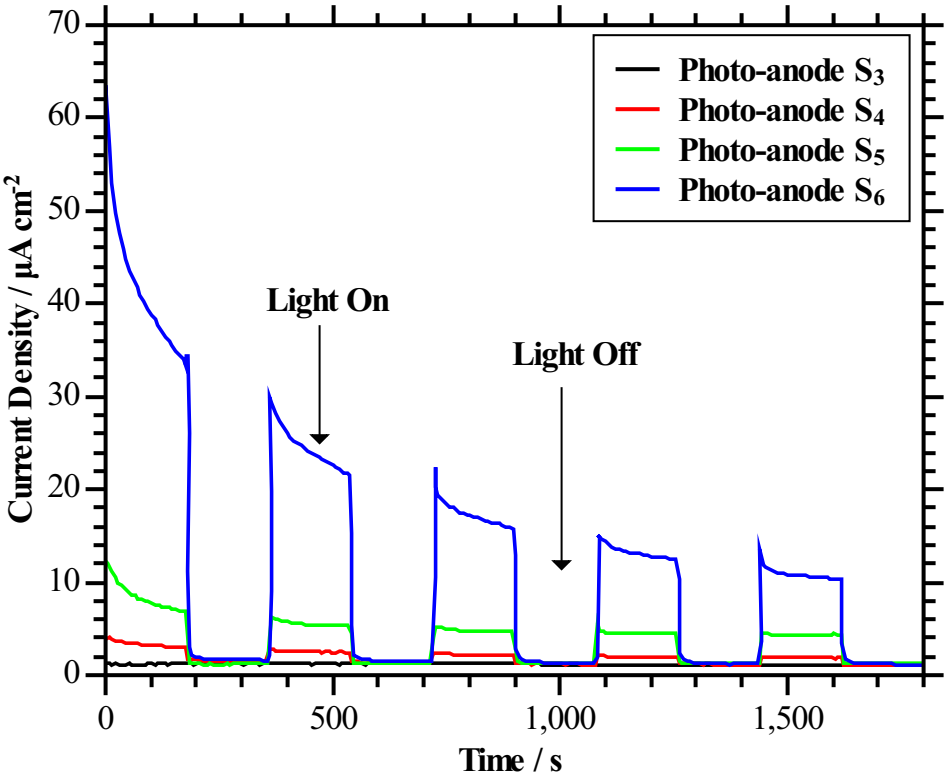

Figure 6.6: Current density-time curves of the photo-anodes S_3, S_4, S_5 and S_6.

6.6. Chapter Summary and Conclusions

MoO_x, WO_3 and W-doped MoO_x films were deposited on FTO-ABS by spin-coating at 4000 RPM applied for 40 seconds and subsequent heat treatment at 470 °C for 2 hours.

The microstructure of the photo-anodes was analyzed by SEM. It was determined that the films morphology of the electrodes containing molybdenum oxide (photo-anodes S_3, S_5 and S_6) was heterogeneous and with irregular conglomerates of random orientation.

It was not possible to determine by SEM analysis the presence of tungsten oxides in the electrodes S_4, S_5 and S_6, due to the low thickness of these films or the zones possibly W-rich.

The composition of the films was characterized by XRD analysis. It was concluded that the photo-anodes S_3, S_5 and S_6 exhibit diffraction peaks at $2\theta = 25.8$ and 37.8°, corresponding to the orthorhombic structure of MoO_3 ((0 4 0) and (0 6 0) diffraction planes), whereas photo-anodes S_4, S_5 and S_6 present diffraction peaks at $2\theta = 23.2$, 23.7, 24.4 °, and aditionally, a minor intensity peak at 34.4 ° in the electrode S_6 corresponding to monoclinic structure of WO_3 ((0 0 2), (0 2 0), (2 0 0) and (2 0 2) diffraction planes). Therefore, the electrodes S_5 and S_6 present films composed for an alloy of MoO_3-WO_3.

Some samples presented two phases not well defined (electrodes S_5 and S_6). In such situation, the band-gap can not be measured reliably because the band-gap does not exist well defined either.

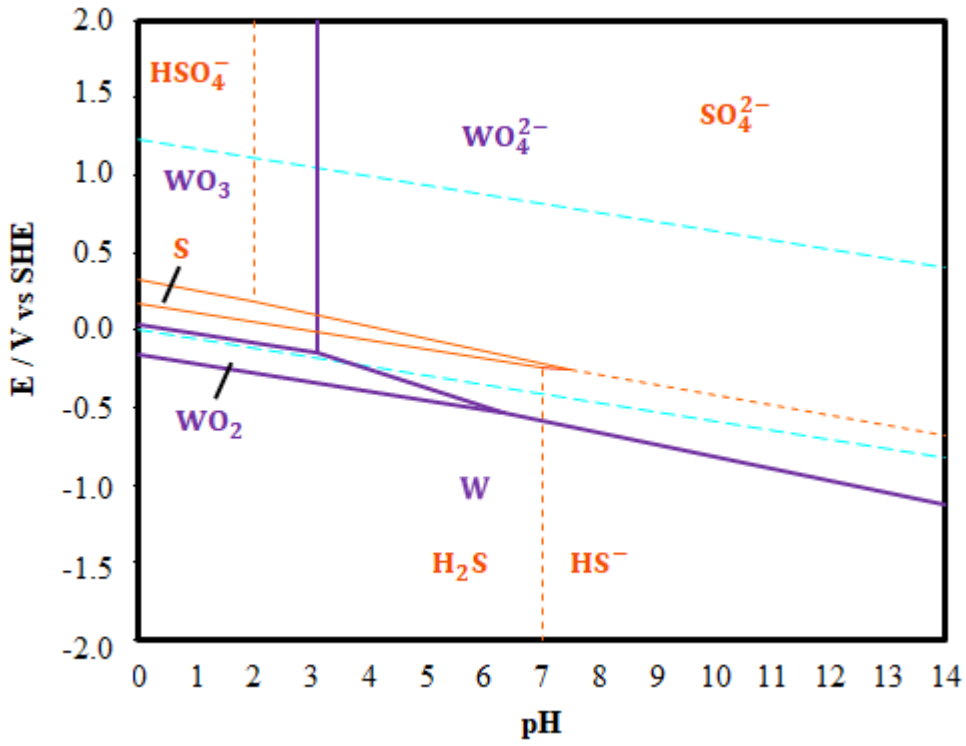

Figure 6.7: Eh-pH diagrams for tungsten at 298 K and 10^5 Pa. Activity of molybdenum species equal to 10^{-6} and activity of sulfate species equal to 10^{-2}.

According to j-E curves (Figure 6.5) the photo-anode S_6 outperforms the rest throughout the experiment, reaching about 80 μA cm^{-2} at 1.23 V vs RHE. This suggests that the amount of layers forming the film obtained by spin-coating has a significant effect on the photo-anode performance. This improvement would be due to the fact that there is more material that promote large surface areas in the photo-anodes produced, which in turn must result in better light exposure and more active sites for the PEC oxygen evolution reaction.

Photocurrent-time curves at 1.23 V vs RHE in Figure 6.6 also confirm that photo-anode S_6 exhibits a good photo-current performance in comparison to the rest. However, this study reveals that all the electrodes lose stability during the experiment (photo-current decrease).

Eh-Ph diagrams were developed in order to analyse by a thermodynamic analysis the films stability in each fabricated electrode. From this study, it was determined that in the experimental conditions in which photo-electrochemical characterization (photocurrent-time curves) was performed (pH 6.73 and 1.23 V vs RHE), WO_4^{2-} and MoO_4^{2-} seem to be the most stable forms of tungsten and molybdenum. Therefore, it is suggested that pH or electrolyte composition is revised for future work. An alternative is to use 0.1 M H_2SO_4 as electrolyte in the photo-electrochemical characterization tests instead of use Na_2SO_4. Pennisi *et. al.* have reported that tungsten-molybdenum oxide electrodes have a suitable stability and good electrochromic properties using this type of electrolyte in voltammetries ranging from 0.6 to -0.6 V vs SCE.

Chapter 7

Conclusions

This thesis informed the study and performance characterization of photo-anodes based on molybdenum oxides synthesized by two routes: (i) electrodeposition and (ii) spin-coating.

- **Undoped and nickel-doped molybdenum oxide photo-anodes**

Undoped and nickel-doped molybdenum oxide films were electrodeposited by applying -1.377 V vs Ag/AgCl (3 M KCl) during 3 hours on an FTO-coated glass substrate immersed in molibdatecitrate aqueous solutions at pH 9. A thin undoped MoO_2/MoO_3 film (438 nm) was obtained on the sustrate surface for the photo-anode S_1 and a thick MoO_2/MoO_3-Ni_2H/NiOOH film (763 nm) was deposited on the sustrate surface for the photo-anode S_2.

Specifically, for a n-type semiconductor (as the undoped and nickel-doped Molybdenum oxide films) in a PEC, photogenerated holes initiate the OER at the surface of the semiconductor electrode and oxidize water to oxygen; whereas photogenerated electrons entering the counter electrode drive the HER and reduce water to hydrogen. A semiconductor material that can efficiently absorb sunlight to generate electron-hole pairs and that has a high mobility and long lifetime to prevent electron-hole recombination within the material before the electron-hole pairs reach the electrode | electrolyte interface is needed to achieve efficient solar-to-hydrogen (STH) conversion. Although, the undoped and nickel-doped molybdenum oxide photo-electrodes have an optimal band-gap (electrode S_1: 3.15 eV and electrode S_2: 2.58 eV) for harnessing sufficient sunlight, the photo-electrochemical characterization showed that these electrodes do not exhibit a stability in aqueous solution, which is one of the main limiting factor for the use of conventional photovoltaic semiconductors as photo-electrodes. For chemically stable photo-anodes, efforts should be made to find an adequate electrolyte and suitable experimental conditions (potential, pH or post-calcination treatment). In the case of the undoped and nickel-doped molybdenum oxide photo-electrodes, Morales e*t. al* [24] has reported that for water splitting applications, these films would need a post-calcination treatment in order to obtain stable photo-anodes. Moreover, for these electrodes, it is also suggested to avoid contact with acid solutions, since it favor the degradation of deposited films on the photo-anodes surface and it is recommended not to apply cathodic potentials, due to the possible formation of sulfides such as MoS_2 on the electrodes surface when the photo-electrochemical characterization is performed.

On the other hand, photo-corrosion in aqueous environments is one of the most significant obstacles to the widespread deployment of semiconductor materials as PEC cells for solar hydrogen production. When photo-corrosion affects an anode in a PEC, photo-generated holes prefer to drive the self-decomposition of the semiconductor instead of the water oxidation reaction, resulting in instability under illumination in aqueous solution. This is caused due to the semiconductor has a less positive oxidative photo-decomposition potential than the OER potential. The undoped and nickel-doped molybdenum oxide films are susceptible to oxidative photo-decomposition as indicated in section 5.5. Various strategies to solve this instability problem have been explored. The most attractive is the protection of the semiconductor by a suitable oxide thin film, resistant to the electrolyte and transparent to sunlight [112] and, therefore it is suggested to consider this option for a future work.

- **MoO_x, WO_3 and W-doped MoO_x photo-anodes**

MoO_x, WO_3 and W-doped MoO_x films on FTO-ABS were deposited by spin-coating at 4,000 RPM applied for 40 seconds and subsequent heat treatment at at 470 °C for 2 hours . Most obtained films were almost transparent (electrodes S_3, S_4 and S_5). It is important to mention that all these transparent electrodes had a film composed of a single layer. The only exception was the photo-anode S_6 which had a film composed of three layers.

The XRD analysis indicated that the deposited films on FTO-ABS were crystalline in all the samples and that there was the presence of MoO_3 of orthorhombic structure on the electrode S_3 , while the electrode S_4 had monoclinic WO_3 on its surface. In the case of electrodes S_5 and S_6, showed films formed by orthorhombic MoO_3 and monoclinic WO_3. A more detailed films analysis composition by EDS and XPS analysis should be performed in order to determine the percentage composition and oxidation state of the species that formed the films.

The morphology of the WO_3 and MoO_3-WO_3 samples (phot-anodes S_4, S_5 and S_6) was complex to study, because through SEM analysis the WO_3 presence could not be confirmed due to the thinness of the films. Complementary characterizations such as AFM would help to have more detailed information on the morphology of the synthesized films.

Almost all applications of semiconductors involve controlled doping, which is the substitution of impurity atoms, into the lattice. Very small amounts of dopants dramatically affect the conductivity of semiconductors. The microstructural analysis revealed that the electrodes S_5 and S_6 are composed of two phases instead of being doped.

The j-E and j-t curves indicated that the electrode S_6 had a better performance in the photo-electrochemical characterization. This improvement would be due to the fact that there is more material that promote large surface areas in the photo-anodes produced.

On the other hand, the electrodes did not have good stability (j-t curves decrease). As were suggested for the undoped and nickel-doped molybdenum oxide photo-anodes, for chemically stable photo-anodes an appropriate electrolyte and suitable experimental conditions must be selected (potential, pH or post calcination). In order that these electrodes have a longer lifetime, an alternative is to use 0.1 M H_2SO_4 as electrolyte in the photo-electrochemical characterization tests instead of use Na_2SO_4. Pennisi *et. al.* have reported that tungsten-

molybdenum oxide electrodes have a suitable stability and good electrochromic properties using this type of electrolyte in voltammetries ranging from 0.6 to -0.6 V vs SCE.

Chapter 8

Future Work

From the photo-electrochemical characterization results reported for the performances and stability of fabricated photo-anodes, future work could focus on:

1. Most metal oxides used as photo-electrodes belong to the so-called d^0 group, such as the MoO_3/MoO_2. In order to improve light harvesting by reducing the band-gap and get a better stability, the VB level of the semiconductor based photo-electrode can be raised by partially substituting oxygen with other anionic species, such as N, S, or C [66]. Therefore, it could be considered these impurities in the synthesis of the molybdenum oxides photo-anodes (by electrodeposition and / or spin-coating) in order to compare the stability of the generated fillms and their performance in photo-electrochemical cells.

2. To consider the use of stable materials in the synthesis of photo-anodes, instead of use molybdenum oxides films on FTO-coated glass. Crystalline structures of the form ABO_3 are promising candidates for both photo-anodes and photo-cathodes, since their electronic properties can be often tailored by substituting the A or B site cations without strong perturbation of the crystal structure and stability [66]. With the substitution of proper metals the Fermi level, the band-gap energy and the density of states in the conduction and valence bands can be tuned. Moreover, both transitions from n- to p-type behaviour (and vice versa) and CB level tuning (e.g., in $SrTiO_3$ or $BaTiO_3$) can be obtained by introducing suitable dopants [66].

Bibliography

[1] Roser, M. and Ortiz-Ospina, E. World population growth. *Our World in Data*, 2017.

[2] The World Bank. Energy use in kg of oil equivalent per capita. `https://data.worldbank.org/indicator/EG.USE.PCAP.KG.OE`, 2019.

[3] The World Bank. Total population. `https://data.worldbank.org/indicator/sp.pop.totl`, 2019.

[4] International Energy Agency. Key world energy statistics 2016. `https://www.worldenergy.org/wp-content/uploads/2016/10/World-Energy-Resources_FullReport_2016.pdf`, 2016.

[5] Díaz, F. and Gracia, F. Oxidative steam reforming of glycerol for hydrogen production: thermodynamic analysis including different carbon deposits representation and CO_2 adsorption. *International Journal of Hydrogen Energy*, 37(19):14820–14830, 2012.

[6] Bak, T., Nowotny, J., Rekas, M., and Sorrell, C. Photo-electrochemical hydrogen generation from water using solar energy. materials-related aspects. *International journal of hydrogen energy*, 27(10):991–1022, 2002.

[7] NIST (2016). National institute of standards and technology. `http://webbook.nist.gov`, 2016.

[8] US Department of Energy (2019). Hydrogen data book. `http://hydrogen.pnl.gov/hydrogen-data/basic-hydrogen-properties`, 2019.

[9] Ong, C. K. *Design and performance of photo-electrochemical reactors with Fe_2O_3 photo-anodes for water splitting*. PhD thesis, Imperial College London, 2013.

[10] Kelsall, G. Course notes. section 5: Energy conversion and storage. 8^{th} European Summer School on Electrochemical Engineering, France, 2018.

[11] Bossel, U. Well-to-wheel studies, heating values, and the energy conservation principle. Technical report, European Fuel Cell Forum, Morgenacherstrasse, 2003.

[12] The Physics Factbook. Energy density of hydrogen. `https://hypertextbook.com/facts/2005/MichelleFung.shtml`, 2005.

[13] Ordin, P. Safety standard for hydrogen and hydrogen systems: Guidelines for hydrogen system design, materials selection, operations, storage, and transportation. office of safety and mission assurance. *National Aeronautics and Space Administration, Washington DC*, 1997.

[14] Steinbach, A. Doe hydrogen and fuel cells program 2015 annual progress report. *Report no. FC104 (US Department of Energy, Washington, DC, USA, 2015)*.

[15] Archer, M. Electrochemical aspects of solar energy conversion. *Journal of Applied Electrochemistry*, 5(1):17–38, 1975.

[16] Walter, G, Warren, E., McKone, J., Boettcher, S., Mi, Q., Santori, E., and Lewis, N. Solar water splitting cells. *Chemical reviews*, 110(11):6446–6473, 2010.

[17] Krol, R. and Grätzel, M. *Photo-electrochemical hydrogen production*, volume 90. Springer, 2012.

[18] SOLARGIS. Distribution of solar irradiation in the world. `https://solargis.com/maps-and-gis-data/overview/`, 2019.

[19] Conibeer, G. and Richards, B. A comparison of pv/electrolyser and photo-electrolytic technologies for use in solar to hydrogen energy storage systems. *International Journal of Hydrogen Energy*, 32(14):2703–2711, 2007.

[20] Xu, Y. and Schoonen, M. The absolute energy positions of conduction and valence bands of selected semiconducting minerals. *American Mineralogist*, 85(3-4):543–556, 2000.

[21] Dukstiene, N., Sinkeviciute, D., and Guobiene, A. Morphological, structural and optical properties of MoO_2 films electrodeposited on SnO_2 glass plate. *Central European Journal of Chemistry*, 10(4):1106–1118, 2012.

[22] Al-Kandari, H., Mohamed, A., Al-Kharafi, F., Zaki, M., and Katrib, A. Modification of the catalytic properties of MoO_{2-x}(OH) y dispersed on TiO_2 by pt and cs additives. *Applied Catalysis A: General*, 417:298–305, 2012.

[23] Ober, A. Mineral commodity summaries 2018. Technical report, US Geological Survey, 2018.

[24] Morales, J., Colet, M., and García, M. Speciation model of the mo (vi)-ni (ii)-citrate-s (vi)-n (iii) aqueous system for the study of the electrodeposition of molybdenum and nickel oxides films. *Journal of The Electrochemical Society*, 165(9):D344–D353, 2018.

[25] Wang, H., Wang, Y., and Chen, X. Synthesis of uniform silver nanowires from agcl seeds for transparent conductive films via spin-coating at variable spin-speed. *Colloids and Surfaces A: Physicochemical and Engineering Aspects*, 565:154–161, 2019.

[26] Balzarotti, R., Cristiani, C., and Francis, L. Combined dip-coating/spin-coating depositions on ceramic honeycomb monoliths for structured catalysts preparation. *Catalysis*

Today, 2019.

[27] Lee, M., Lee, I., Tsai, S., Chen, C., Wu, M., and Juang, Y. Spin coating of polymer solution on polydimethylsiloxane mold for fabrication of microneedle patch. *Journal of the Taiwan Institute of Chemical Engineers*, 70:42–48, 2017.

[28] Podlaha, E. and Landolt, D. Induced codeposition i. an experimental investigation of ni-mo alloys. *Journal of the Electrochemical Society*, 143(3):885–892, 1996.

[29] Marlot, A., Kern, P., and Landolt, D. Pulse plating of ni–mo alloys from ni-rich electrolytes. *Electrochimica Acta*, 48(1):29–36, 2002.

[30] Jiangtian, L. and Nianqiang, W. Correction: Semiconductor-based photocatalysts and photoelectrochemical cells for solar fuel generation: a review. *Catalysis Science & Technology*, 4(12):4440–4440, 2014.

[31] Oldham, K., Myland, J., and Bond, A. *Electrochemical science and technology: fundamentals and applications*. John Wiley & Sons, 2011.

[32] Bamford, C., Tipper, C., and Compton, R. *Electrode kinetics: Principles and methodology*, volume 26. Elsevier, 1986.

[33] Aravena, C. Estudio y caracterización de ánodos de litio metálico. ms thesis, university of chile, 2015.

[34] Bockris, J. and Reddy, A. Electroquímica moderna, 1980.

[35] Compton, R. and Banks, C. *Understanding voltammetry*. World Scientific, 2011.

[36] Morales, J. Síntesis de un fotoánodo basado en óxidos de molibdeno a partir de electrodeposición en soluciones diluidas de molibdato y citrato.thesis, university of chile, 2017.

[37] Takeno, N. Atlas of eh-ph diagrams. *Geological survey of Japan open file report*, 419: 102, 2005.

[38] Shriver, D., Weller, M., Overton, T., Armstrong, F., and Rourke, J. Inorganic chemistry. *Geological survey of Japan open file report*, 419:102, 2005.

[39] Tzedakis, T. Course notes. section 3: Mass transport. 8^{th} European Summer School on Electrochemical Engineering, France, 2018.

[40] Plawsky, J. *Transport phenomena fundamentals*. CRC Press, 2009.

[41] Dharmadasa, I. and Haigh, J. Strengths and advantages of electrodeposition as a semiconductor growth technique for applications in macroelectronic devices. *Journal of The Electrochemical Society*, 153(1):G47–G52, 2006.

[42] Chen, Z., Dinh, H., and Miller, E. *Photoelectrochemical water splitting*. Springer, 2013.

[43] Ossila. Spin coating: A guide to theory and techniques. https://www.ossila.com/pages/spin-coating, 2019.

[44] Dilli, Z. Intrinsic and extrinsic semiconductors, fermi-dirac distribution function, the fermi level and carrier concentrations, 2009.

[45] Atkins, P. Atkins' physical chemistry 7th edition., 2006.

[46] Rajeshwar, K. Fundamentals of semiconductor electrochemistry and photoelectrochemistry. *Encyclopedia of electrochemistry*, 6:1–53, 2007.

[47] Rodriguez, J., Candal, R., Solís, J., Estrada, W., and Blesa, M. El fotocatalizador: síntesis, propiedades y limitaciones. *Solar Safe Water*, 9:135–152, 2005.

[48] Encyclopaedia Britannica. Fermi-dirac statistics. https://www.britannica.com/science/Fermi-Dirac-statistics, 2019.

[49] Nowotny, J., Sorrell, C., Sheppard, L., and Bak, T. Solar-hydrogen: environmentally safe fuel for the future. *International journal of hydrogen energy*, 30(5):521–544, 2005.

[50] Grätzel, M. Photoelectrochemical cells. *nature*, 414(6861):338, 2001.

[51] Licht, S. A description of energy conversion in photoelectrochemical solar cells. *Nature*, 330(6144):148, 1987.

[52] Lopes, T., Andrade, L., Ribeiro, H., and Mendes, A. Characterization of photoelectrochemical cells for water splitting by electrochemical impedance spectroscopy. *international journal of hydrogen energy*, 35(20):11601–11608, 2010.

[53] Carver, C., Ulissi, Z., Ong, C.K., Dennison, S., Kelsall, G., and Hellgardt, K. Modelling and development of photoelectrochemical reactor for h2 production. *International Journal of Hydrogen Energy*, 37(3):2911–2923, 2012.

[54] Hashimoto, K., Fujishima, A., and Murasawa, S. Water purification using efficient TiO_2 photocatalyst: application to aquarium water filter systems. In *Proceedings of the symposium on water purification by photocatalytic, photoelectrochemical, and electrochemical processes. USA: The Electrochemical Society*, pages 368–71, 1994.

[55] Pickett, J. *Electrochemical reactor design*, volume 9. Elsevier Science Ltd, 1979.

[56] Ho, S.P. Design and analysis of an electrochemical cell for caustic concentration and power generation. *Industrial & Engineering Chemistry Process Design and Development*, 24(2):444–450, 1985.

[57] Edson, G. Electrolytic reactor, 1986.

[58] Xu, L., Deng, X., Abken, A., Cao, X., Du, W., Vijh, A., Ingler, W., Chen, C., Fan, Q., and Collins, R. Critical research for cost-effective photoelectrochemical production of hydrogen. Technical report, Midwest Optoelectronics, LLC, Toledo, OH (United

States), 2014.

[59] Haussener, S., Xiang, C., Spurgeon, J., Ardo, S., Lewis, N., and Weber, A. Modeling, simulation, and design criteria for photoelectrochemical water-splitting systems. *Energy & Environmental Science*, 5(12):9922–9935, 2012.

[60] Fan, Q., Onischak, M., and Liss, W. Solar cell electrolysis of water to make hydrogen and oxygen, July 10 2007. US Patent 7,241,950.

[61] Linkous, C. and Slattery, D. *Solar Photocatalytic H_2 Production from Water Using Dual Bed Photosystem.* 2001.

[62] Aroutiounian, V., Arakelyan, V., and Shahnazaryan, G. Metal oxide photoelectrodes for hydrogen generation using solar radiation-driven water splitting. *Solar Energy*, 78 (5):581–592, 2005.

[63] Kelly, N. and Gibson, T. Solar energy concentrating reactors for hydrogen production by photoelectrochemical water splitting. *International Journal of Hydrogen Energy*, 33 (22):6420–6431, 2008.

[64] Wang, Z., Chou, H., Wu, J., Tsai, D., and Mul, G. CO_2 photoreduction using $NiO/InTaO_4$ in optical-fiber reactor for renewable energy. *Applied Catalysis A: General*, 380(1-2):172–177, 2010.

[65] Marinangeli, R. and Ollis, D. Photo-assisted heterogeneous catalysis with optical fibers. part iii: Photoelectrodes. *AIChE Journal*, 28(6):945–955, 1982.

[66] Meda, L. and Abbondanza, L. Materials for photo-electrochemical water splitting. *Reviews in Advanced Sciences and Engineering*, 2(3):200–207, 2013.

[67] Nowotny, J., Bak, T., Nowotny, M., and Sheppard, L. Titanium dioxide for solar-hydrogen i. functional properties. *International journal of hydrogen energy*, 32(14): 2609–2629, 2007.

[68] Rajeshwar, K. Hydrogen generation at irradiated oxide semiconductor–solution interfaces. *Journal of Applied Electrochemistry*, 37(7):765–787, 2007.

[69] Sivula, K., Le Formal, F., and Grätzel, M. Solar water splitting: progress using hematite (α-Fe_2O_3) photoelectrodes. *ChemSusChem*, 4(4):432–449, 2011.

[70] Glasscock, J., Barnes, P., Plumb, I., Bendavid, A., and Martin, P. Structural, optical and electrical properties of undoped polycrystalline hematite thin films produced using filtered arc deposition. *Thin Solid Films*, 516(8):1716–1724, 2008.

[71] Cowan, A., Barnett, C., Pendlebury, S., Barroso, M., Sivula, K., Gratzel, M., Durrant, J., and Klug, D. Activation energies for the rate-limiting step in water photooxidation by nanostructured α-Fe_2O_3 and TiO_2. *Journal of the American Chemical Society*, 133 (26):10134–10140, 2011.

[72] Barroso, M., Cowan, A., Pendlebury, S., Gratzel, M., Klug, D., and Durrant, J. The role of cobalt phosphate in enhancing the photocatalytic activity of α-Fe_2O_3 toward water oxidation. *Journal of the American Chemical Society*, 133(38):14868–14871, 2011.

[73] Butler, M. Photoelectrolysis and physical properties of the semiconducting electrode WO_2. *Journal of Applied Physics*, 48(5):1914–1920, 1977.

[74] Wang, H., Lindgren, T., He, J., Hagfeldt, A., and Lindquist, S. Photolelectrochemistry of nanostructured WO_3 thin film electrodes for water oxidation: mechanism of electron transport. *The Journal of Physical Chemistry B*, 104(24):5686–5696, 2000.

[75] Kelsall, G. Eh-ph daigrams. personal communication, g.kelsall@imperial.ac.uk. 2017.

[76] Kondo, J. CuO_2 as a photocatalyst for overall water splitting under visible light irradiation. *Chemical Communications*, (3):357–358, 1998.

[77] Paracchino, A., Laporte, V., Sivula, K., Grätzel, M., and Thimsen, E. Highly active oxide photocathode for photoelectrochemical water reduction. *Nature materials*, 10(6): 456, 2011.

[78] Zhao, Y., Zhang, Y., Yang, Z., Yan, Y., and Sun, K. Synthesis of MoS_2 and MoO_2 for their applications in H_2 generation and lithium ion batteries: a review. *Science and technology of advanced materials*, 14(4):043501, 2013.

[79] Scanlon, D., Watson, G., Payne, D., Atkinson, G., Egdell, R., and Law, D. Theoretical and experimental study of the electronic structures of MoO_3 and MoO_2. *The Journal of Physical Chemistry C*, 114(10):4636–4645, 2010.

[80] Dukštienė, N. and Sinkevičiūtė, D. Photoelectrochemical properties of MoO_2 thin films. *Journal of Solid State Electrochemistry*, 17(4):1175–1184, 2013.

[81] Patil, R., Uplane, M., and Patil, P. Structural and optical properties of electrodeposited molybdenum oxide thin films. *Applied Surface Science*, 252(23):8050–8056, 2006.

[82] Adedokun, O. Review on transparent conductive oxides thin films deposited by sol-gel spin coating technique. *International Journal of Engineering Science and Application*, 2(3):88–97.

[83] Granqvist, C. Transparent conductors as solar energy materials: A panoramic review. *Solar energy materials and solar cells*, 91(17):1529–1598, 2007.

[84] Ali, M., Ibrahim, K., Hamad, O., Eisa, M., Faraj, M., and Azhari, F. Deposited indium tin oxide (ito) thin films by dc-magnetron sputtering on polyethylene terephthalate substrate (pet). *Rom. J. Phys*, 56(5-6):730–741, 2011.

[85] Moon, C. and Han, J. Low temperature synthesis of ito thin film on polymer in ar/H_2 plasma by pulsed dc magnetron sputtering. *Thin Solid Films*, 516(19):6560–6564, 2008.

[86] Hjiri, M., Ghribi, F., and El Mir, L. Characterization of ito thin films prepared by

sol-gel spin-coating technique. *Sensors & Transducers*, 27(5):198, 2014.

[87] Dawood, Y., Hassoni, M., and Mohamad, M. Effect of solution concentration on some optical properties of indium oxide doped with SnO_2 thin films prepared by chemical spray pyrolysis technique. *International Journal of Pure and Applied Physics*, 2(1):1–7, 2014.

[88] Shembel, E., Apostolova, R., Nagirny, V., Kirsanova, I., Grebenkin, P., and Lytvyn, P. Electrolytic molybdenum oxides in lithium batteries. *Journal of Solid State Electrochemistry*, 9(2):96–105, 2005.

[89] Ananikov, V. Nickel: the "spirited horse" of transition metal catalysis, 2015.

[90] Kuznetsov, V., Pavlov, M., Kuznetsov, K., and Kudryavtsev, V. Kinetics of cathodic processes of deposition of nickel–molybdenum alloys from an ammonia–citrate electrolyte. *Russian journal of electrochemistry*, 39(12):1338–1341, 2003.

[91] Kuznetsov, V., Pavlov, M., Chepeleva, S., and Kudryavtsev, V. Effect of concentration of ammonia and citrate ions on the kinetics of cathodic reactions during electrodeposition of a nickel-molybdenum alloy. *Russian Journal of Electrochemistry*, 41(1):75–81, 2005.

[92] Kuznetsov, V., Morozova, N., and Kudryavtsev, V. Chronoamperometric studies in an ammonia citrate electrolyte for the deposition of a nickel-molybdenum alloy. *Russian Journal of Electrochemistry*, 42(6):665–669, 2006.

[93] Hsu, C., Chan, C., Huang, H., Peng, C., and Hsu, W. Electrochromic properties of nanocrystalline moo_3 thin films. *Thin Solid Films*, 516(15):4839–4844, 2008.

[94] McKeen, L. *Permeability properties of plastics and elastomers*. William Andrew, 2016.

[95] Njoka, F., Ahmed, M., and Ookwawara S. Desing of a novel photoelectrochemical reactor for hydrogen prodution. *WIT Transactions on Ecology and the Environment*, 224:349–361, 2017.

[96] Borgschulte, A., Sambalova, O., Delmelle, R., Jenatsch, S., Hany, R., and Nüesch F. Hydrogen reduction of molybdenum oxide at room temperature. *Scientific reports*, 7: 40761, 2017.

[97] Cruywagen, J., Rohwer, E., and Wessels G. Molybdenum (vi) complex formation—8. equilibria and thermodynamic quantities for the reactions with citrate. *Polyhedron*, 14 (23-24):3481–3493, 1995.

[98] Antonietti, M. and Müllen, K. *Chemical Synthesis and Applications of Graphene and Carbon Materials*. John Wiley & Sons, 2016.

[99] Chassaing, E., Quang, K., and Wiart, R. Mechanism of nickel-molybdenum alloy electrodeposition in citrate electrolytes. *Journal of Applied Electrochemistry*, 19(6):839–844, 1989.

[100] Popczyk, M. and Łosiewicz, B. Effect of molybdenum (iv) oxide on the process of hydrogen evolution on ni+ mo electrolytic composite coatings. In *Solid State Phenomena*, volume 228, pages 277–282. Trans Tech Publ, 2015.

[101] David O Scanlon, Graeme W Watson, DJ Payne, GR Atkinson, RG Egdell, and DSL Law. Theoretical and experimental study of the electronic structures of MoO_3 and MoO_2. *The Journal of Physical Chemistry C*, 114(10):4636–4645, 2010.

[102] Yan, J., Wu, G., Guan, N., Li, L., Li, Z., and Cao, X. Understanding the effect of surface/bulk defects on the photocatalytic activity of TiO_2: anatase versus rutile. *Physical Chemistry Chemical Physics*, 15(26):10978–10988, 2013.

[103] Sanjines, R., Tang, H., Berger, B., Gozzo, F., Margaritondo, G., and Levy, F. Electronic structure of anatase TiO_2 oxide. *Journal of Applied Physics*, 75(6):2945–2951, 1994.

[104] Grosvenor, A., Biesinger, M., Smart, R., and McIntyre, M. New interpretations of xps spectra of nickel metal and oxides. *Surface Science*, 600(9):1771–1779, 2006.

[105] Oliveira, M. and do Rego, A. The effect of the hypophosphite ion oxidation on the ni surface electrode—an xps study. *Journal of Alloys and Compounds*, 425(1-2):64–68, 2006.

[106] Casa XPS. Satellite peaks. `www.casaxps.com/help_manual/XPSInformation/IntroductiontoXPS.htm`, 2005.

[107] Ling-Ju, G., Jun-Wei, L., Tao, H., Su-Huai, W., and Shu-Shen, L. Photo-corrosion limited maximum efficiency of solar photo-electrochemical water splitting. *Physical Review Applied*, 10(6):064059, 2018.

[108] Kim, J., Shin, K., Cho, S., Lee, T., and Park, J. Synthesis of transparent mesoporous tungsten trioxide films with enhanced photoelectrochemical response: application to unassisted solar water splitting. *Energy & Environmental Science*, 4(4):1465–1470, 2011.

[109] Klinbumrung, A., Thongtem, T., and Thongtem, S. Characterization of orthorhombic α-MoO_3 microplates produced by a microwave plasma process. *Journal of Nanomaterials*, 2012:10, 2012.

[110] Bathe, S. and Patil, P. Electrochromic characteristics of pulsed spray pyrolyzed polycrystalline WO_3 thin films. *Smart Materials and structures*, 18(2):025004, 2008.

[111] Farjana, H., Torben, D., Kourosh, K., and Jian Zhen, O. Two-dimensional transition metal oxide and chalcogenide-based photocatalysts. *Nano-micro letters*, 10(2):23, 2018.

[112] Pennisi, A., Simone, F., and Lampert, CM. Electrochromic properties of tungsten-molybdenum oxide electrodes. *Solar energy materials and solar cells*, 28(3):233–247, 1992.

[113] EESEMI (2005). Electromagnetic spectrum tables. `http://eesemi.com/emspectrum`.

htm, 2005.

[114] PRO-LITE (2019). Electromagnetic spectrum. http://www.pro-lite.co.uk/File/laser_safety_laser_basics.php, 2019.

[115] Goldstein, J., Newbury, D., Michael, J., Ritchie, N., Scott, J., and Joy, D. *Scanning electron microscopy and X-ray microanalysis*. Springer, 2017.

[116] Callister, W. and Rethwisch, D. Applications and processing of metal alloys. *Materials Science and Engineering: an Introduction. 8th ed. Hoboken, NJ: John Wiley & Sons*, pages 391–406, 2010.

[117] PHYSICAL ELETRONICS. Xps / esca. https://www.phi.com/surface-analysis-techniques/xps-esca.html, 2019.

[118] M., Wenjie,. Fundamental theory of atomic force microscopy. http://www.nanoscience.gatech.edu/zlwang/research/afm.html, 2019.

[119] Stenzel, O. *The physics of thin film optical spectra*. Springer, 2005.

[120] Choi, J. and Thompson, L. Xps study of as-prepared and reduced molybdenum oxides. *Applied Surface Science*, 93(2):143–149, 1996.

[121] Baltrusaitis, J., Mendoza, B., Fernandez, V., Veenstra, R., Dukstiene, N., Roberts, A., and Fairley, N. Generalized molybdenum oxide surface chemical state xps determination via informed amorphous sample model. *Applied Surface Science*, 326:151–161, 2015.

Appendix A

Electromagnetic Spectrum

For a better understanding of this work, two resources are attached: a summary of the electromagnetic spectrum in Figure A.1 and Table A.1 where the range of wavelengths, frequency and energy of each of the types of electromagnetic radiation are specified.

Table A.1: Wavelength ranges, frequency and energy of the electromagnetic spectrum. Obtained from EESEMI [113]

	Electromagnetic spectrum		
Name	**Wavelength**	**Frequency (Hz)**	**Energy (eV)**
Gamma Rays	<0.02 nm	>15 EHz	>62.1 keV
X-Rays	0.01 nm – 10 nm	30 EHz – 30 PHz	124 keV – 124 eV
Ultraviolet	10 nm – 400 nm	30 PHz – 750 THz	124 eV – 3 eV
Visible Light	390 nm – 750 nm	770 THz – 400 THz	3.2 eV – 1.7 eV
Infrared	750 nm – 1 mm	400 THz – 300 GHz	1.7 eV – 1.24 meV
Microwaves	1 mm – 1 m	300 GHz – 1 GHz	1.24 meV – 1.24 μeV
Radio	1 mm – 100,000 km	300 GHz – 3 Hz	1.24 meV – 12.4 feV

Table A.2: Visible spectrum. Obtained from EESEMI [113].

Visible radiation	Wavelength (10^{-6}m)
Extreme infrared	$40 < \lambda < 1000$
Far infrared	$6 < \lambda < 40$
Medium infrared	$1.5 < \lambda < 6$
Near infrared	$0.77 < \lambda < 1.5$
Red	$0.622 < \lambda < 0.770$
Orange tree	$0.597 < \lambda < 0.622$
Yellow	$0.577 < \lambda < 0.597$
Green	$0.492 < \lambda < 0.577$
Blue	$0.455 < \lambda < 0.492$
Violet	$0.390 < \lambda < 0.455$
Near ultraviolet	$0.30 < \lambda < 0.39$
Far ultraviolet	$0.20 < \lambda < 0.30$
Extreme ultraviolet	$0.01 < \lambda < 0.20$

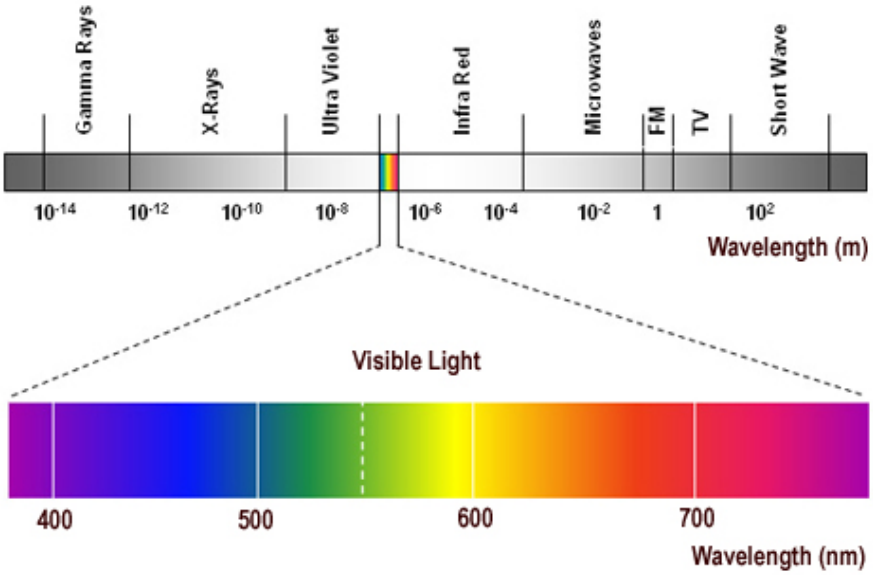

Figure A.1: Electromagnetic spectrum [114].

Appendix B

Electrochemical Analysis

In this research project, two electrochemical techniques were used to study the phenomena occurring in each system:

- Linear sweep voltametry: in the case of the photo-anodes obtained by electrodeposition, this technique was used to determine the potential range at which electrodeposition of undoped or nickel-doped molybdenum oxide films on FTO-coated glass occurs, and to study the photo-activity of these electrodes for the oxygen evolution reaction in dark, white light and under UV illumination. Regarding the photo-anodes obtained by spin-coating, this technique was only used in order to study the photo-activity of the tungsten-doped molybdenum oxide photo-electrodes in light and dark conditions.

- Chronoamperometry: In the case of nickel-doped molybdenum oxide photo-anodes this technique was used to promote the electrodeposition of molybdenum oxide films on FTO-coated glass. Also this technique was used to analyse the stability of the photo-anodes obtained by spin-coating and electrodeposition at constant potential.

Additionally to these electrochemical techniques, measurements of the open circuit potential (OCP) the photo-anodes (undoped and nickel-doped molybdenum oxide electrodes) were done to analyze the presence of photo-activity and conductivity type presented by the films.

In the following sections is presented a brief description of the electrochemical techniques used to study the nickel/tungsten-doped molybdenum oxide photo-anodes.

B.1. Open Circuit Potential (OCP)

It is important to determine the conductivity and flat-band potential of a photo-electrode before carrying out any photo-electrochemical experiments. These properties help to elucidate the band structure of a semiconductor which ultimately determines its ability to drive efficient water splitting. Photo-anodes (n-type conductivity) drive the oxygen evolution reaction (OER) at the electrode | electrolyte interface, while photo-cathodes (p-type conductivity)

drive the hydrogen evolution reaction (HER). The conductivity type is determined from the direction of the shift in the open circuit potential upon illumination. Illuminating the electrode surface will shift the Fermi level of the bulk (measured potential) towards more anodic potentials for a p-type material and towards more cathodic potentials for a n-type material.

The illuminated OCP can be used to estimate the flat-band potential. In electrochemical terms, the potential difference measured between two terminals of an electrical device when disconnected from any circuit (no external load/no current flows) is known as open circuit potential (OCP). In the case of an electrochemical cell this concept corresponds to the Nernst potential and it was defined in Chapter 2 as the electrical voltage measured under equilibrium conditions. It is important to consider that the measurements of OCP depend on some parameters such as the operating temperature, pressure and activities of the species involved in the reactions occurring at each electrode, among others.

B.2. Linear Sweep Voltametry (LSV)

In linear sweep voltammetry (LSV) a fixed potential range is used. The voltage is scanned from a lower limit to an upper limit as shown in Figure B.1(a).

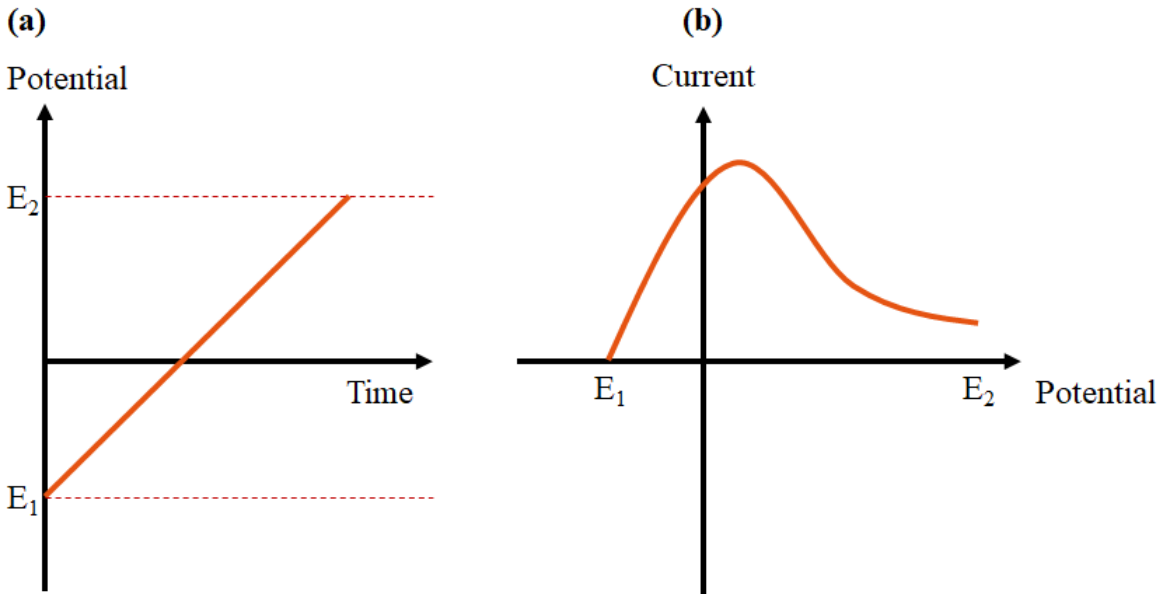

Figure B.1: (a) Linear potential sweep, (b) Resulting linear sweep voltammetry

In this technique, the characteristics of the linear sweep voltammogram recorded depend on some factors such as:

- The rate of the electron transfer reaction(s).
- The chemical reactivity of the electroactive species.
- The voltage scan rate.

The current response is plotted as a function of voltage rather than time, unlike potential step measurements as illustrated in Figure B.1(b).

Linear sweep voltammetry is successfully used in various commercial and/or industrial applications due to advantages such as its rapid response. In the case of this PhD project, this technique has been useful in the determination of the adequate potential for the electrodeposition of films on FTO-coated glass and in the study of the photo-activity of the synthesized photo-electrodes under different operating conditions and for the photo-electrochemical characterization of the electrodes synthesized by spin-coating and electrodeposition.

B.3. Chronoamperometry

Chronoamperometry is an electrochemical technique in which the potential of the working electrode is stepped and the resulting current from faradaic processes occurring at the electrodes is monitored as a function of time. The charging current generated decay exponentially with time while the species in the electrochemical cell reacts and the gradient of the concentration profiles decays. This result provides a notion of the depletion/saturation processes occurring at each electrode surface and their effect in the performance of the electrochemical cell.

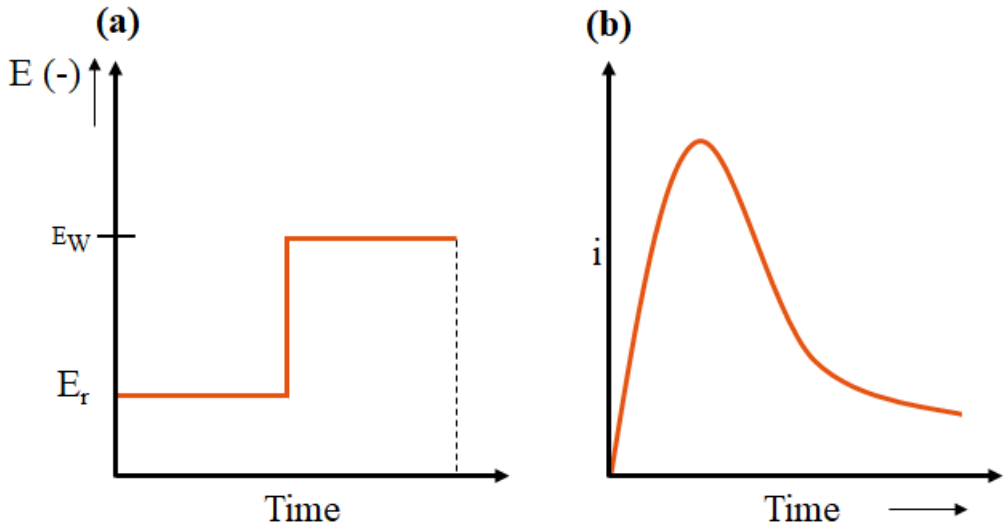

Figure B.2: (a) Potential step applied during a chroamperometry, (b) resulting chronoamperometry

Figure B.2(a) shows the potential function applied during a chronoamperometry experiment. A characteristic response to this potential pulse is illustrated in (b), where the measured current is plotted as a function of time.

This electrochemical technique has been of vital importance in this research in the manufacture of photo-anodes and to study their long-term stability when used in a photo-electrochemical cell.

Appendix C

Techniques for Microstructure and Composition Characterization

The composition of the undoped and nickel/tungsten-doped molybdenum oxide films was characterized by XPS, EDX and XRD analysis, while the microstructural characterization was carried out by AFM and SEM. The XRD analyzes were also used to characterize the crystallinity of the deposits of tungsten-doped molybdenum oxide films.

C.1. Scanning electron microscopy (SEM)

This type of microscope is an electronic device which allows analysing the surface structure of a sample by scanning it with a high-energy beam of electrons in a raster scan pattern. In the scanning process, the electrons interact with the atoms that make up the sample producing signals that contain important information related to the surface topography and other properties of the sample, such as its electrical conductivity [115].

In a conventional SEM the types of signals produced involve secondary electrons, back-scattered electrons (BSE), characteristic X-rays, light (cathode-luminescence), specimen current and transmitted electrons [115].

In the scanning process, the energy exchange between the electron beam and the sample results in the reflection of high-energy electrons by elastic scattering, emission of secondary electrons by inelastic scattering and the emission of electromagnetic radiation, each of which can be detected by specialized detectors to create digital images [173].

In this research work, the scanning electron microscope was used to provide information about the microstructure of the undoped or nickel/tungsten-doped molybdenum oxide photo-anodes films.

C.2. Energy-Dispersive X-ray Spectroscopy (EDS or EDX)

This technique is based on the examination and analysis of a set of peaks obtained when the sample is excited using a high-energy beam of charged particles, such as electrons or protons, or an x-rays beam. The characterization capabilities of the EDS are due in large part to the fundamental principle that each element has a unique atomic structure allowing unique set of peaks on its X-ray spectrum [115].

Any EDS device has four primary components: (1) the excitation source (electron beam or X-ray beam), (2) the X-ray detector, (3) the pulse processor, and (4) the analyser. Electron beam excitation is used in scanning electron microscopes (SEM), which means that usually SEM and EDS techniques can be applied using the same equipment, as in the case of the first stage of this research project.

For this thesis, EDS measurements provided a preliminary elemental analysis of the compounds formed on the surface of FTO-coated glass used as a substrate for the undoped or nickel-doped molybdenum oxide photo-anodes obtained by electrodeposition.

C.3. X-ray Diffraction (XRD)

X-ray diffraction (XRD) is an analytical technique to determine the atomic and molecular structure of a polycrystalline sample using the diffracted pattern produced when an X-ray beam strikes the electrons (scatterers) contained in the atoms of the crystals. In this X-ray method, a regular array of scatterers produces an array of spherical waves which could cancel one another in most directions (destructive interference) or constructively interfere in a few specific directions generating a diffracted beam characterized by Bragg's law [116]:

$$2\mathrm{d}sin\theta = n\lambda \tag{C.1}$$

In the above equation, d, is the spacing between diffracting planes of the crystal, θ is the incident angle of the X-ray beam, n is any integer, and λ is the wavelength of the beam.

It is important to mention that Bragg's law is a simple expression relating the x-ray wavelength and interatomic spacing to the angle of the diffracted beam. If for some reason the Bragg's law is not satisfied, then the interference will be non-constructive in nature so as to yield a very low-intensity diffracted beam. X-rays are used in order to produce the diffraction pattern because their wavelength λ is typically the same order of magnitude (1 – 100 angstroms) as the spacing d between planes in the crystal, which is necessary to produce significant diffraction.

In this research work, XRD analysis was used to identify the composition of the deposits formed on the surface of FTO-ABS used as a substrate for the undoped or tungsten-doped molybdenum oxide photo-anodes obtained by spin-coating.

C.4. X-ray Photoelectron Spectroscopy (XPS)

X-ray Photoelectron Spectroscopy (XPS) also known as Electron Spectroscopy for Chemical Analysis (ESCA) is a widely used surface analysis technique due to the broad range of materials that can be analyzed with it and provides important quantitative and chemical state information from the surface of the material being studied [117].

XPS is usually accomplished by exciting a samples surface with mono-energetic Al kα X-rays generating photoelectrons to be emitted from the sample surface. In this technique, an electron energy analyzer is used to measure the energy of the emitted photoelectrons. From the binding energy and intensity of a photoelectron peak, the elemental identity, chemical state, and quantity of a detected element can be determined.

The average depth of analysis for an XPS measurement is around 5 nm and the information XPS provides about surface layers or thin film structures is crucial for many industrial and research applications where surface or thin film composition plays a critical role in performance such as: nanomaterials, photovoltaics, catalysis, corrosion, adhesion, electronic devices and packaging, magnetic media, display technology, surface treatments, and thin film coatings used for numerous applications, among others [117].

In this investigation, this technique was used for the analysis of the undoped or nickel-doped molybdenum photo-anodes in order to determine the existence of molybdenum on the surface of the deposits formed and determine the relative abundance of the oxidation states of the Mo.

C.5. Atomic Force Microscopy (AFM)

The atomic force microscope (AFM) is one type of scanning probe microscopes (SPM). SPMs are designed to measure local properties with a probe in a sample including: height, friction and magnetism. To acquire an image, the SPM raster-scans the probe over a small area of the sample, measuring the local property in parallel [118].

AFMs work by measuring force between a probe and the sample. Usually, the probe is a sharp tip, which is a 3-6 μm tall pyramid with 15-40 nm end radius. Although the lateral resolution of AFM is low ($\sim$ 30 nm) due to the convolution, the vertical resolution can be up to 0.1 nm [118].

The AFM technique was used in this thesis to obtain information on the morphology of the surface and the thickness of the films of the undoped or nickel-doped molybdenum photo-anodes deposited on FTO-coated glass.

Appendix D

Technique for the Optical Characterization

In order to have a complete optical characterization, analyzes by UV-Visible Spectroscopy for the photo-anodes were performed.

D.1. Ultraviolet–Visible Spectroscopy

UV-V spectroscopy measures the absorption of light of a sample (solid transparent or liquid) in the ultraviolet and visible light wavelengths ranges. Usually, samples are dispensed into cuvettes in the case of liquid or in the case of solids they are fixed in a position that favors the measurement. In both cases the samples are placed in the path between a UV-V light and a detector. According to Beer-Lambert's law, with a constant light path length and known absorption coefficient (dependent upon wavelength), the concentration (in a liquid) or the thickness (of a solid) can be determined from the light absorbed by the sample at that wavelength.

UV-visible spectrophotometry was used in this research to determine the absorbance and band-gap of the undoped and nickel/tungsten-doped molybdenum oxide films produced.

Appendix E

Tauc Plot - Determining Optical Band-Gap

A Tauc plot is a method used to determine the optical band-gap, or Tauc-gap, in semiconductors materials [119]. This parameter is often used to characterize optical properties of materials such as metal oxides.

To build this type of diagrams, the square root of the product of the absorption coefficient and photon energy - $(aE)^{0,5}$ - is plotted versus photon energy. Usually, the curve should have a section of straight line. If extended to the x-axis, the x-intercept of this line gives the optical band-gap as illustrated in Figure E.1.

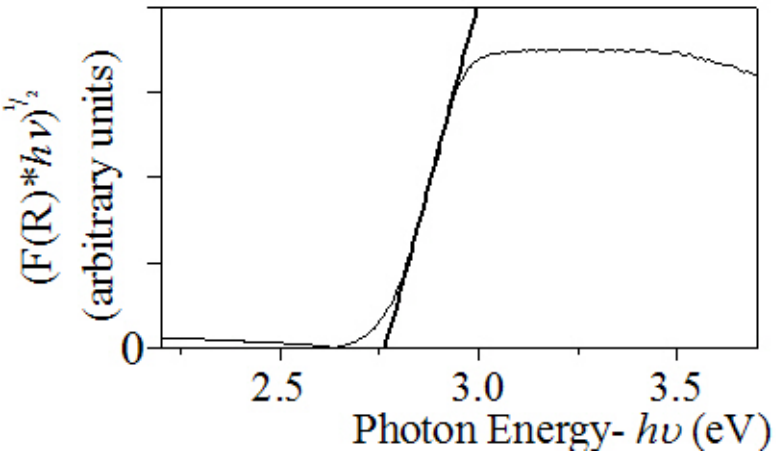

Figure E.1: An example of a Tauc plot [119].

Appendix F

Additional EDS Results

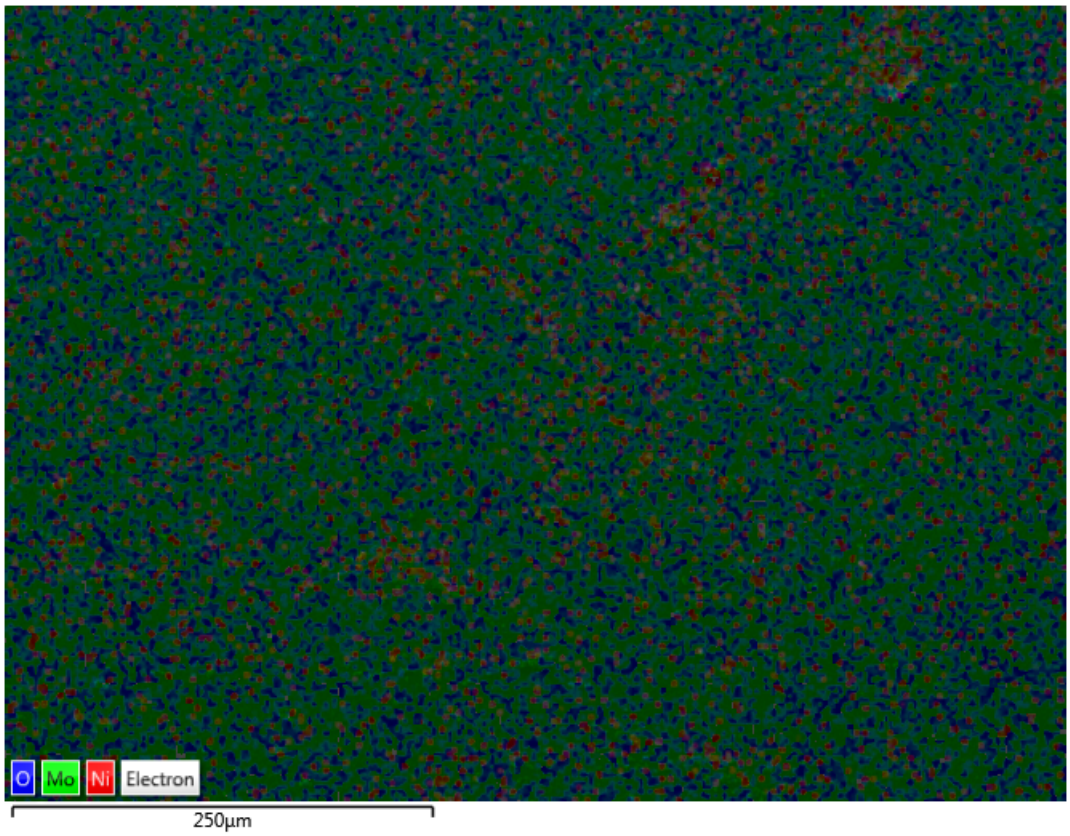

Figure F.1: EDS layered image of nickel-doped molybdenum oxide photo-anode.

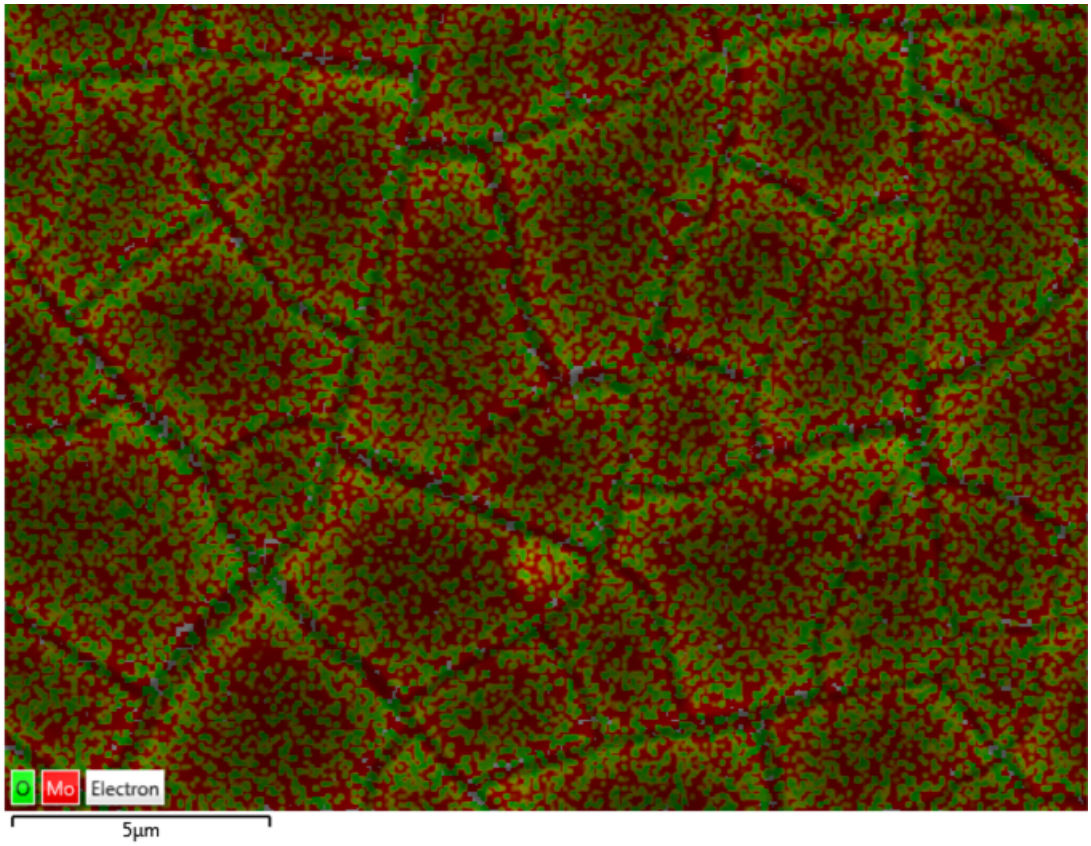

Figure F.2: EDS layered image of undoped molybdenum oxide photo-anode.

Appendix G

Additional XPS Results

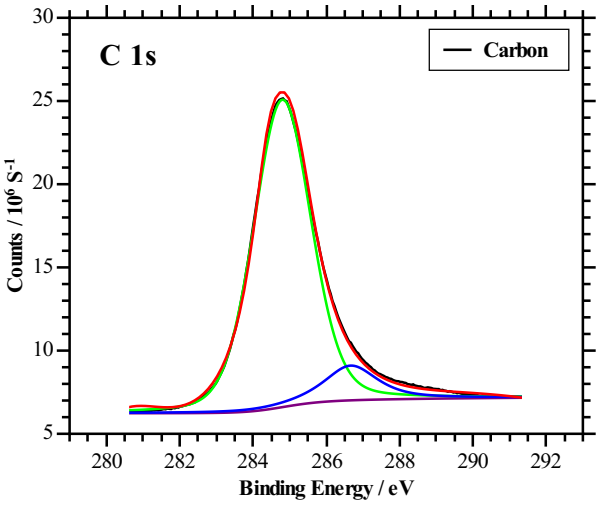

Figure G.1: XPS spectrum of C 1s of photo-anode S_2.

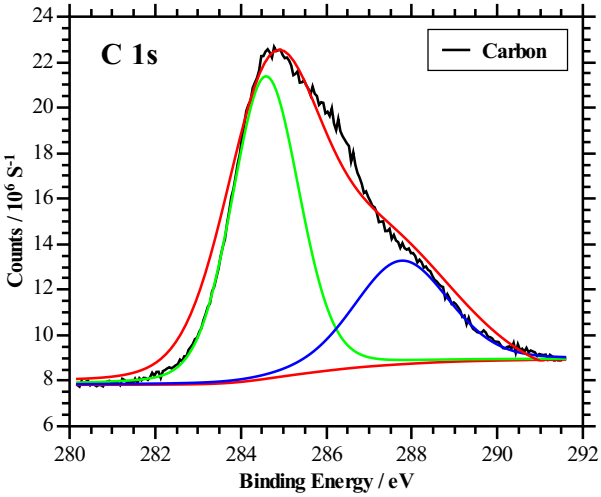

Figure G.2: XPS spectrum of C 1s of photo-anode S_1.

Table G.1: XPS spectrum of Mo 3d in different molybdenum oxides. Obtained from [120] [121].

	$Mo3d_{3/2}$ (eV)			$Mo3d_{5/2}$ (eV)		
Muestra	**Mo (+4)**	**Mo (+5)**	**Mo(+6)**	**Mo (+4)**	**Mo (+5)**	**Mo(+6)**
MoO_3			235.6			232.5
MoO_3 reduced	233		235.4	229.9		232,3
MoO_2	233.1		235.4	230		232.3
MoO_2 reduced	233.2	234.3	235.7	230.1	231.2	232.6
MoO_2 reduced	233.1	234	235.6	230	230,9	232.5

Appendix H

Additional AFM Results

The thicknesses determined by AFM for the deposited film in the electrode S_2 were measured without considering the conglomerates present on the film. Below there is an example of calculation using the Gwyddion.

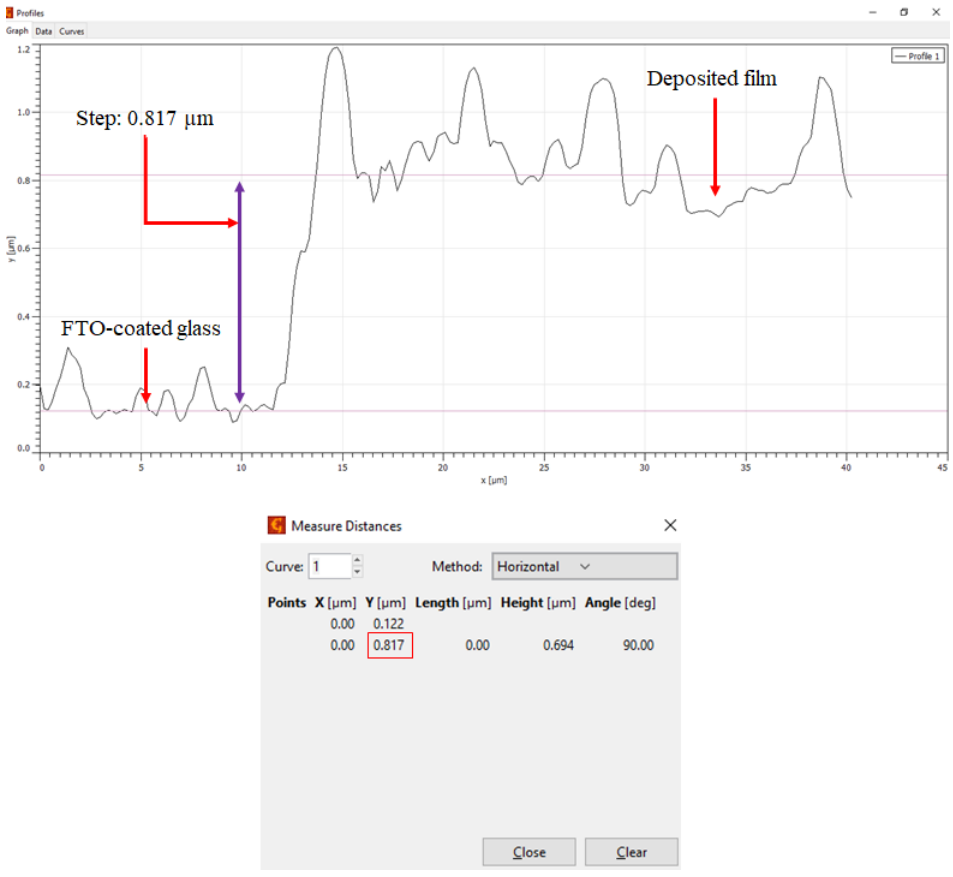

Figure H.1: Step on the deposited film in the electrode S_2.

The measurements were repeated in different areas of the sample in order to obtain a representative thickness.

Appendix I

Photo-electrochemical cell

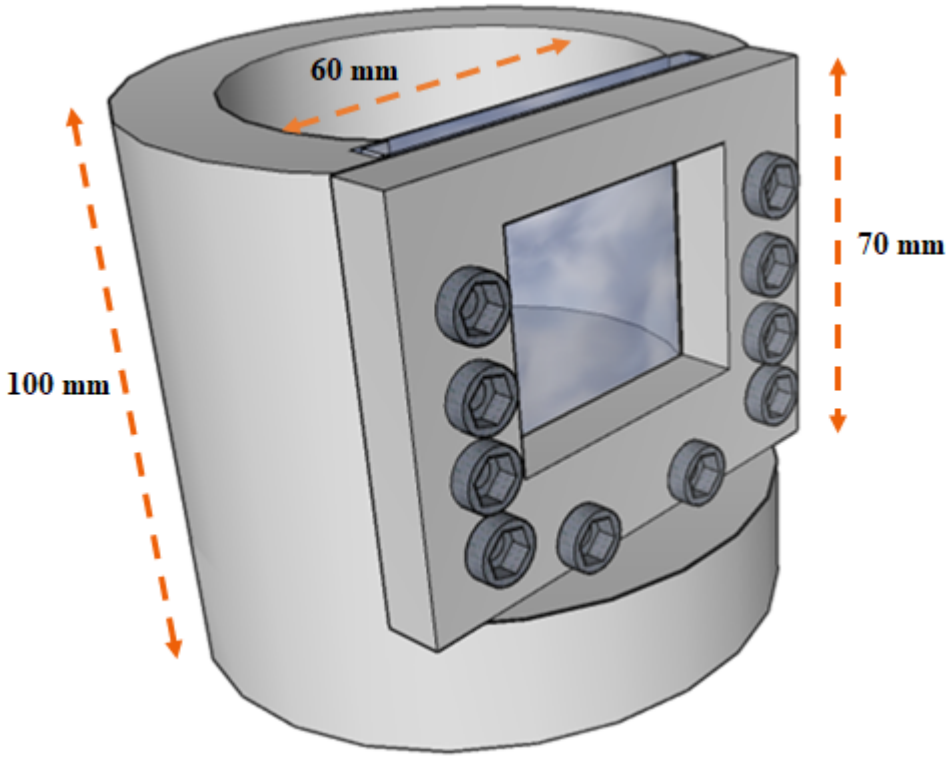

Figure I.1: Front-view number 1 of the photo-electrochemical cell.

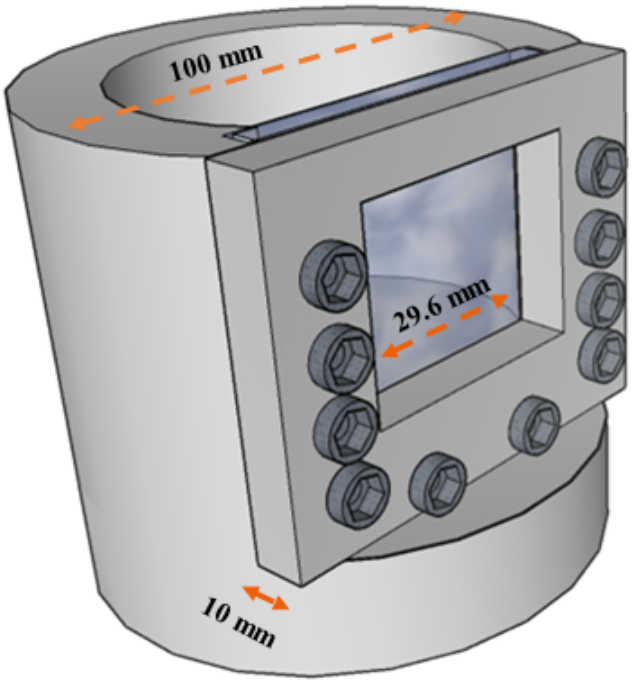

Figure I.2: Front-view number 2 of the photo-electrochemical cell.

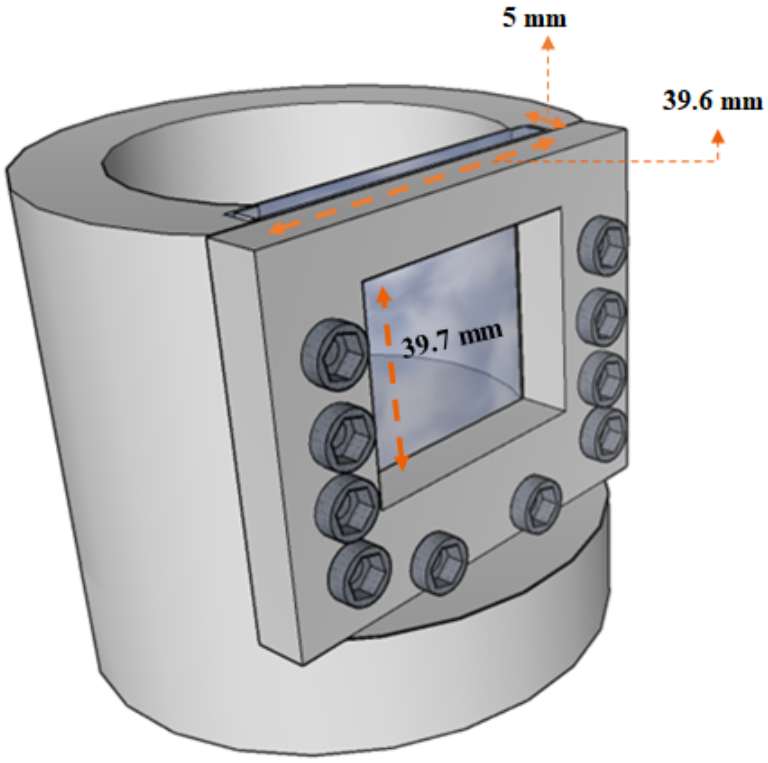

Figure I.3: Front-view number 3 of the photo-electrochemical cell.

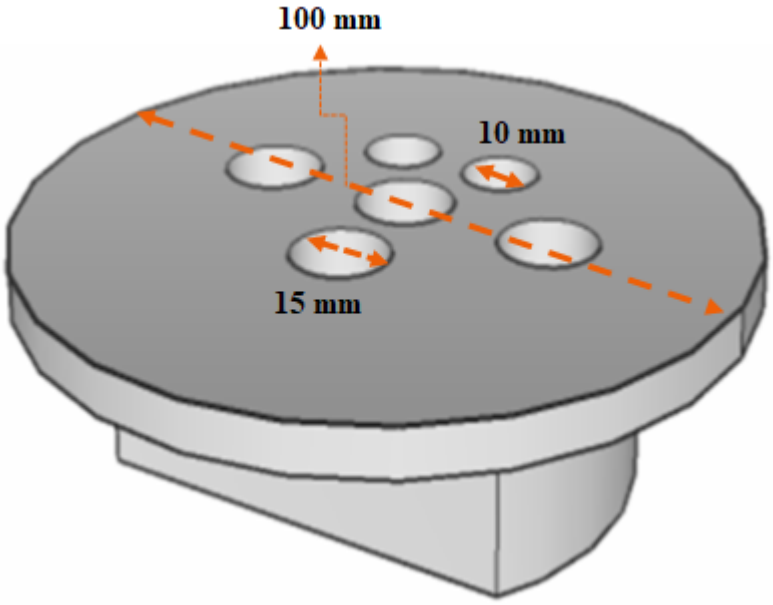

Figure I.4: View number 1 of the lid of the photo-electrochemical cell.

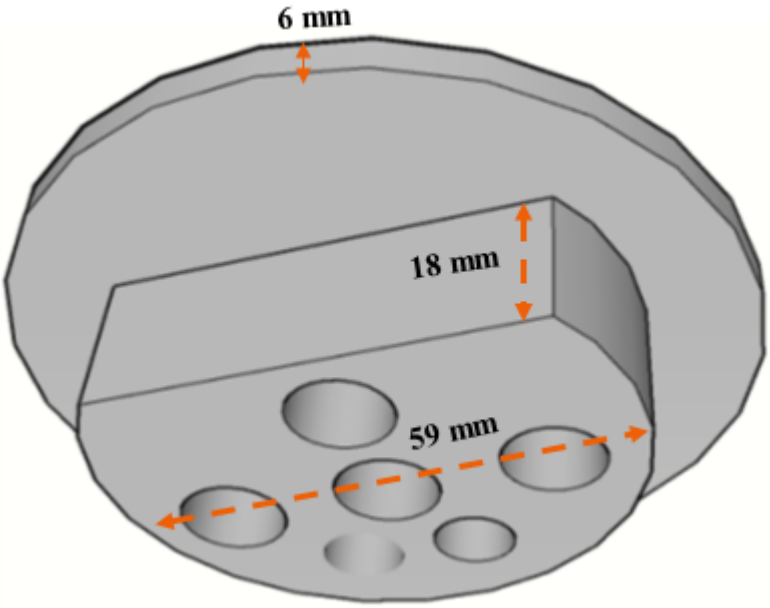

Figure I.5: View number 2 of the lid of the photoelectrochemical cell.

Figure I.6: Photography number 1 of the photo-electrochemical cell.

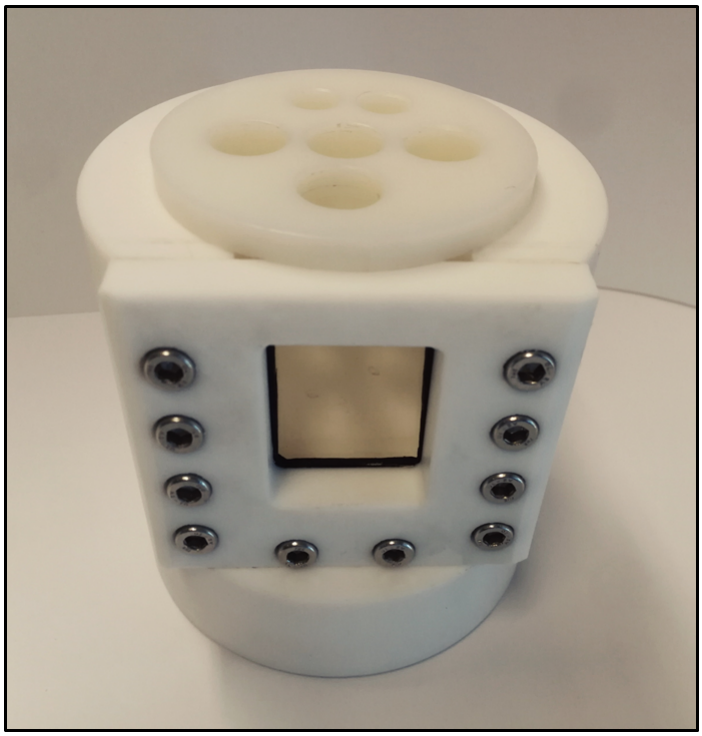

Figure I.7: Photography number 2 of the photo-electrochemical cell.

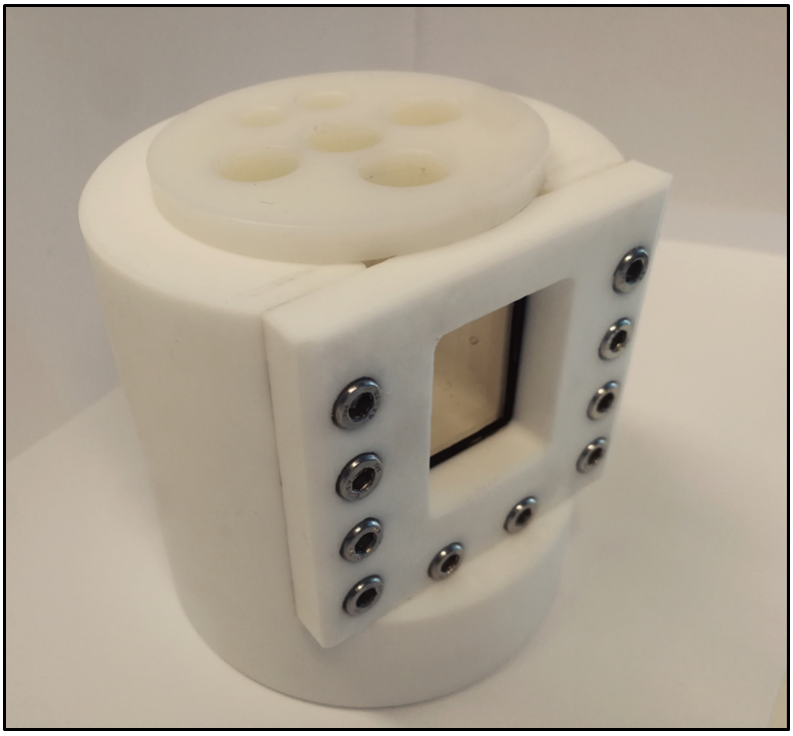

Figure I.8: Photography number 3 of the photo-electrochemical cell.

Appendix J

Academic articles

Next, the academic articles and posters published and presented during this doctoral thesis have been attached.

1. M. García-García, M. Colet-Lagrille*, Electrochemical fabrication of MoO_2/MoO_3-based photo-anodes for water splitting, ECS Transactions, 77(9) 77-83, 2017

2. J. Morales-Santelices, M. Colet-Lagrille*, M. Garcia-Garcia, Speciation model of the Mo(VI)-Ni(II)-Citrate-S(VI)-N(III) aqueous system for the study of the electrodeposition of molybdenum and nickel oxides films", Journal of The Electrochemical Society, 165(9) 344-353, 2018.

3. Póster: Photo-electrochemical activity of molybdenum-nickel-based photo-anodes for the oxygen evolution reaction, 69^{th} Annual Meeting of the International Society of Electrochemistry, Italia, septiembre 2018.

Electrochemical Fabrication of MoO_2/MoO_3-based Photo-Anodes for Water Splitting

M. García-García and M. Colet-Lagrille

Departament of Chemical Engineering and Biotechnology, Universidad de Chile, Beauchef 851, Santiago, Chile

Photo-electrochemical cells are a promising technology for the environmentally-benign production of hydrogen using solar energy. In this kind of cells, a photo-active material is coated or deposited on a substrate (e.g. fluorine-doped tin dioxide(FTO)-coated glass) which acts as current collector and support. In this research project, a molybdenum oxide layer is electrochemically deposited on the surface of a FTO-coated glass working electrode immersed in a solution containing 0.075 M molybdate (MoO_4^{2-}), 0.075 M nickel sulfate ($NiSO_4 \cdot 6H_2O$), 0.5 M tri-sodium citrate ($Na_3C_6H_5O_7 \cdot 2H_2O$) and 0.7 M ammonium hydroxide (NH_4OH), by applying a potential of -1.377 V vs Ag/AgCl (3 M KCl) during 3 hours. The characterization of the photo-anodes produced suggests that they present semiconducting and catalytic properties which make them attractive for their application in a photo-electrochemical cell for water splitting.

Introduction

An 80% of the total thermal and electrical energy produced worldwide comes from the combustion of fossil fuels, implying that it is not generated cleanly and sustainably (1). In addition, fossil fuels are non-renewable, which motivates the study and development of systems for energy generation based on renewable sources (e.g. sunlight or wind) that, also, are environmentally friendly.

In this scenario, an attractive alternative to fossil fuels is hydrogen (2,3), which combustion (oxidation) in an electrochemical cell (fuel cell) produces electricity and water as the reaction product. On the other hand, considering that water is a convenient and abundant source of hydrogen, a significant amount of research has been carried out on the development of systems that use renewable energy sources (particularly, solar energy) for hydrogen production via water splitting (4):

$$H_2O(l) \rightarrow H_2(g) + \tfrac{1}{2}\, O_2(g), \quad \Delta G°(298K) = 237 \text{ kJ mol}^{-1} \qquad [1]$$

This Gibbs free energy of reaction is equivalent to a potential difference $\Delta E° = 1.23$ V, which corresponds to the minimum potential that has to be applied between the electrodes (anode and cathode) of an electrochemical cell to promote the water splitting reaction [1].

Photo-electrochemical cells offer a promising method for hydrogen production directly driven by solar energy (4). Indeed, the anode and/or cathode of these cells are made using semiconductor materials capable of absorbing the energy of the photons in

Journal of The Electrochemical Society, **165** (9) D344-D353 (2018)
0013-4651/2018/165(9)/D344/10/$37.00 © The Electrochemical Society

Speciation Model of the Mo(VI)-Ni(II)-Citrate-S(VI)-N(III) Aqueous System for the Study of the Electrodeposition of Molybdenum and Nickel Oxides Films

J. Morales-Santelices, M. Colet-Lagrille, [z] and M. García-García

Department of Chemical Engineering, Biotechnology and Materials, Faculty of Physical and Mathematical Sciences, Universidad de Chile, Santiago, Región Metropolitana, Chile

A speciation model is proposed for the determination of the concentration of different species formed in an aqueous solution containing Mo(VI), Ni(II), citrate, ammonia and sulfate at 298 K, 10^5 Pa and variable pH and Mo(VI)/Ni(II) activity ratios. This solution is to be used as electrolyte in the electrodeposition process of thin films of Mo and Ni oxides, which appear to be a promising material for the fabrication of photo-anodes for water splitting in photo-electrochemical cells. The speciation model comprises 53 species and their stability constants, which are related through molar and charge balances to estimate the composition of the solution given a pH value and formal concentrations. As a result, predominance and distribution diagrams are produced, based on which electrolyte conditions (pH and central species concentrations) are recommended to maximize the availability of desired species for the electrodeposition process. Eh-pH diagrams for molybdenum and nickel species at the recommended activities (10^{-2} for Mo and Ni species, and 10^{-1} for citrate, ammonia and sulfate species) are also produced, to determine the adequate potential range to be applied for the electrodeposition of Mo and Ni oxides films.
 [DOI: 10.1149/2.0191809jes]

Manuscript submitted March 9, 2018; revised manuscript received May 4, 2018. Published June 1, 2018.

Molybdenum oxides have recently emerged as a promising alternative in the search of new semiconductor materials to fabricate photo-electrodes for driving the water splitting reaction (WSR).[1,2] It has been reported that some compounds of the MoO_x family present: (i) n-type semiconduction;[3] (ii) relative band edge positions in aqueous electrolytes[4] and bandgap energy values[3,5] ($E_g > 1.23$ eV) suitable for harvesting enough energy to drive the oxygen evolution reaction (OER) in a water splitting photo-electrochemical cell.[4–6] In addition, molybdenum presents three stable oxidation states (+4 to +6), which is a desirable property for a catalytic surface in electron transfer mediated processes.[7]

Electrodeposition provides a simple, cheap, scalable and manufacturable fabrication method of semiconducting materials.[8] In this context, it is widely accepted that factors such as the electrolyte properties (concentrations of precursors and other compounds dissolved, solvent, pH), the type of substrate, and the electrodeposition parameters (electrode potential, current density, time), influence the morphological and photo-electrochemical properties of the generated semiconducting deposits (films).[8,9] The understanding of the thermodynamic stability of the aqueous electrolyte involved is crucial for the engineering of these parameters, and thus reaching higher solar-to-hydrogen conversion efficiencies (STH) in photo-electrochemical cells containing these photo-electrodes.[10]

In parallel with the studies on the photo-electrochemical applications of molybdenum oxides, the use of nickel as a catalyst has stood out during the last years, with several applications.[11] It is known that the presence of nickel in electrodes provides catalytic activity for both the OER and the hydrogen evolution reaction (HER) in aqueous solution,[12] which in addition with the properties stated above for molybdenum oxides makes attractive the idea of studying photo-electrodes based on mixed molybdenum-nickel oxides.

The co-deposition of nickel(II) with molybdenum(VI) in aqueous media at cathodic potentials has been previously reported.[13,14] Citrate has been added to aqueous electrolytes used in both nickel and molybdenum electrodeposition in several works,[15–18] because of its complexing ability[19,20] which allows to increase the solubility of metals. Besides, citrate is a weak polyprotic acid and therefore acts as a buffer.[21] It has also been stated that citrate interferes favorably in the mechanism of the co-deposition of nickel and molybdenum.[15] Similarly to the addition of citrate, ammonia is added to these electrolytes following the same logic: the formation of nickel complexes[22] and an increase of the solution buffering capacity in more alkaline conditions with respect to what citrate can do by itself.

The objective of this work is to develop a speciation model with thermodynamic data of the Mo(VI), Ni(II), citrate, sulfate and ammonia aqueous system. This model aims to determine the equilibrium concentrations of different species in solution to produce predominance and distribution diagrams. In addition, Eh-pH diagrams are produced for molybdenum and nickel species based on the speciation model results. All these diagrams are useful for choosing the most favorable electrolyte composition and the potential to be applied for the electrodeposition of molybdenum and nickel oxides films.

It should be noted that the thermodynamic results presented in this work are also useful for the study of the electrodeposition of molybdenum-nickel metal alloys, which are of interest in areas as diverse as corrosion protection and catalysis.[13–16]

Model Description

Speciation model.—The speciation model consists of a set of molar and charge balances, which comprises a system of non-linear equations whose inputs are the pH and the moles of each compound added to the electrolyte per kilogram of pure water. Using a set of equilibrium constants at 298 K, 10^5 Pa and in the limit of zero ionic strength[a], a computational routine was developed to solve this system of equations and determine the composition of the electrolyte at the thermodynamic equilibrium as schematized in Figure 1.

The 53 species included in the speciation model are enumerated in Table I and classified in Figure 2[b]. Each of them is associated with: a number, a reversible reaction in aqueous medium and an equilibrium constant. The stoichiometric coefficients and pK values[23–27] are associated with a generic hydrolysis reaction which involves a species

[a]The constants that were reported in media with ionic strength different from zero were extrapolated using the following equation presented in the OCDE Guidelines for the Extrapolation to Zero Ionic Strength:[29]

$$pK_J(I_m = 0) = pK_J(I_m) - \left(A\frac{\sqrt{I_m}}{1+\sqrt{I_m}} - 0.3\sqrt{I_m}\right)\sum_j \nu_j z_j^2$$

where υ_j are the stoichiometric coefficients associated to the reaction linked to species J, and z_j the unitary charge of each of the aqueous species involved in this equilibrium. pK values obtained this way are marked with an asterisk in Table I.

[b]The notation for molybdenum-citrate complexes is taken from the work of Cruywagen, Rohwer and Wessels.[24] [p,q,r] stands for the product of the reaction: $p\ MoO_{4(aq)}^{2-} + q\ Hcit_{(aq)}^{3-} + r\ H_{(aq)}^{+} \leftrightarrow [p, q, r]_{(aq)}^{[2p+3q-r]-}$

[z]E-mail: mcolet@ing.uchile.cl

Photo-Electrochemical Activity of Molybdenum-Nickel-based Photo-Anodes for the Oxygen Evolution Reaction

M. Garcia-Garcia, J. Morales-Santelices, M. Colet-Lagrille
Departament of Chemical Engineering, Biotechnology and Materials,
Faculty of Physical and Mathematical Sciences, Universidad de Chile
matias.garciag@ug.uchile.cl

Introduction

Photo-electrochemical cells (PECs) are a promising technology that can use solar energy to promote the water splitting reaction to produce hydrogen and oxygen gases [1]. In PECs a photo-active material is coated or deposited on a substrate (e.g. fluorine-doped tin dioxide (FTO)-coated glass), which acts as current collector and support. Figure 1 shows a schematic of the operation of a PEC for water hydrolysis.

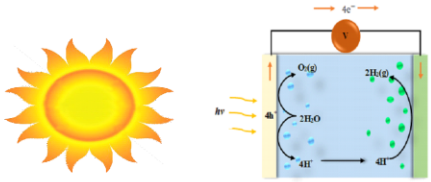

Figure 1: Operation of PEC for hydrolysis of water. The anode is the photosensitive electrode in this case. Adapted from [2].

Results

Linear sweep voltammetries obtained using the photo-anodes in Figure 2, for the study of the oxygen evolution reaction (OER), are shown in Figure 3. The measurements were carried out in dark, white light and under UV illumination, the latter using lamps at two different wavelengths in the ultraviolet region ($?_{1max}$ = 364 nm and $?_{2max}$ = 385 nm).

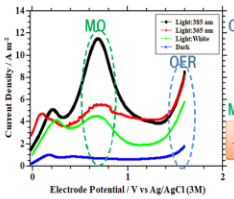

Oxygen Evolution Reaction (OER) [3]:

$$\frac{1}{2}O_2 + 2H^+_{(aq)} + 2e^- \leftarrow H_2O_{(l)}$$

MoO_2 Oxidation (MO):

$$MoO_{3(s)} + 2H^+_{(aq)} + 2e^- \leftarrow MoO_{2(s)} + H_2O_{(l)}$$

Figure 3: Linear sweep voltammograms (25 mV s^{-1}) of the system 0.1 M Na_2SO_4 | MoO_2 / MoO_3 | FTO in the dark and under different types of illumination. Electrolyte at pH 3.5.

Experimental

MoO_x-Ni Electrodeposition

In this research, molybdenum-nickel-based photo-anodes (Figure 2) are fabricated by electrochemical deposition of molybdenum oxides and nickel on the surface of FTO-coated glass (cathodic potential of -1.377 V vs Ag/AgCl (3 M KCl) applied for 3 hours).

Working electrode: FTO-coated glass (1.5 cm^2)

Counter electrode: Platinum foil (1.25 cm^2)

Reference electrode: Ag/AgCl (3 M KCl)

Electrolyte: Molibdate (from MoO_3) (0.075M): $NiSO_4 \cdot 6H_2$ (0.075M): $Na_3C_6H_5O_7 \cdot 2H_2O$ (0.5M): NH_4OH (0.7M). Electrolyte at pH equal to 9.0.

Cell Setup

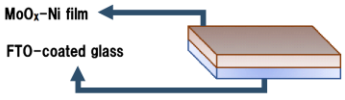

Figure 2: MoO_x-Ni on FTO-coated glass

Conclusions

- The oxidation of $MoO_{2\,(s)}$ to $MoO_{3\,(s)}$ is suggested by the oxidation peaks observed in all the voltammograms (peaks around 0.7 V vs Ag/AgCl (3 M KCl)), being more evident under UV illumination conditions ($?_1$max = 364 nm and $?_2$max = 385 nm).
- The oxygen evolution reaction is favored under UV illumination, ($?_1$max = 364 nm and $?_2$max = 385 nm) reaching in both cases current densities close to 9 A m^{-2} at 1.6 V vs Ag/AgCl (3 M KCl).
- When the linear sweep voltammetries are carried out under white light, the OER presents a better performance than in the dark; although it does not reach a higher current density than those obtained with UV illumination.

[1] N. Dukstiene and D. Sinkeviciute, *J. Solid State Electrochem.*, **17**, 1175-1184 (2013). https://link.springer.com/article/10.1007/s10008-012-1985-z
[2] J. Kubisztal and A. Budniok, *Int. J. Hydrogen Energy*, **33**, 4488-4494 (2008).
[3] R. van de Krol and M. Grätzel, *Photoelectrochemical Hydrogen Production*, 1st ed., p. 13-19, Springer, New York (2012). http://www.springer.com/la/book/9781461413790

fcfm Ingeniería Química, Biotecnología y Materiales
FACULTAD DE CIENCIAS FÍSICAS Y MATEMÁTICAS
UNIVERSIDAD DE CHILE
GIE rupo Ingeniería Electroquímica